The Pennsylvania State University

The Graduate School

Department of Mechanical and Nuclear Engineering

ELECTROCHEMICAL MODELING, ESTIMATION AND CONTROL OF LITHIUM ION BATTERIES

A Thesis in

Mechanical Engineering

by

Kandler A. Smith

Submitted in Partial Fulfillment
of the Requirements
for the Degree of

Doctor of Philosophy

December 2006

The thesis of Kandler A. Smith was reviewed and approved* by the following:

Chao-Yang Wang
Professor of Mechanical Engineering
Co-Thesis Adviser
Co-Chair of Committee

Christopher D. Rahn
Professor of Mechanical Engineering
Co-Thesis Adviser
Co-Chair of Committee

Qian Wang
Assistant Professor of Mechanical Engineering

Joseph P. Cusumano
Professor of Engineering Science and Mechanics

Karen A. Thole
Professor of Mechanical Engineering
Head of the Department of Mechanical and Nuclear Engineering

*Signatures are on file in the Graduate School.

ABSTRACT

Batteries directly contribute to the advancement of technologies ranging from portable electronics to fuel-efficient vehicles. In high power applications such as hybrid electric vehicles (HEVs), monitoring algorithms use current and voltage measurements to estimate battery state of charge (SOC) and available power. Despite increased cost, these systems commonly employ conservative, oversized batteries due to poor prediction of current/voltage dynamics and imprecise real-time estimation. This dissertation introduces a general, electrochemical model-based approach for safe and efficient integration of Li-ion batteries into transient, pulse power-type systems.

A transient solid-state diffusion model is incorporated into a previously developed 1D electrochemical model. The nonlinear model, solving 4 coupled partial differential equations by a computational fluid dynamics (CFD) technique, is validated against low rate constant current, pulse power, and transient driving cycle data sets from a 6 Ah Li-ion HEV battery. Solid-state Li transport (diffusion) significantly limits high rate performance, and end of discharge at the 2.7 V minimum limit is caused by depleted/saturated active material surface concentrations in the negative/positive electrodes for pulses lasting longer than around 10 seconds. The 3.9 V maximum limit, meant to protect the negative electrode from side reactions such as lithium plating, is overly conservative for pulse charging.

Increased power capability may be realized by using a real-time electrochemical model to estimate internal states and control the battery within appropriate limits. Development of a fast, stable, and accurate model is difficult however, given the infinite-dimensional, distributed nonlinear processes governing battery dynamics. Here, an impedance model is derived from the electrochemical kinetic, species and charge transport equations and, using a model order reduction technique developed herein, the high order transfer functions/matrices are numerically reduced to an observable/controllable state variable model in modal form. Open circuit potential and electrode surface concentration nonlinearities are explicitly approximated in the model output equation on a local and electrode-averaged basis, respectively. Validated against the 313th order CFD model, a 12th order state variable model with 0-10 Hz bandwidth predicts terminal voltage to within 25 mV

(<1%) for pulse and constant current profiles at rates up to 50C. The modeling methodology is valid for all types of porous electrode Li-ion batteries not operating under severe electrolyte transport limitations.

A linear Kalman filter is designed for real-time estimation of internal potentials, concentration gradients, and SOC. A reference current governor predicts operating margin with respect to electrode side reactions and surface depletion/saturation conditions responsible for damage and sudden loss of power. Estimates are compared with the nonlinear CFD model. The linear filter gives to within ~2% performance in the 30-70% SOC range except in the case of severe current pulses that drive electrode surface concentrations near saturation and depletion, although the estimates recover as concentration gradients relax. With 4 to 7 states, the filter has low order comparable to equivalent circuit methods presently employed for battery management but, unlike those empirical methods, enables pulse charging/discharging beyond conservative voltage limits. For the 6 Ah HEV battery, the method increases power density by 22% and streamlines the systems integration process for families of battery/vehicle designs.

TABLE OF CONTENTS

LIST OF FIGURES

LIST OF TABLES

NOMENCLATURE

a_s	active surface area per electrode unit volume, cm^2/cm^3
A	electrode plate area, cm^2
c	concentration of Li in a phase, mol/cm^3
D	diffusion coefficient of Li, cm^2/s
E_{act}	activation energy, J/mol
f	frequency, Hz
F	Faraday's constant, 96,487 C/mol
h	convective heat transfer coefficient, $W/m^2\,K$
I	applied current, A
i_o	exchange current density of electrode reaction, A/cm
j	$\sqrt{-1}$
j^{Li}	reaction current resulting in production or consumption of Li, A/cm^3
L	cell width, cm
ℓ	penetration depth of solid state diffusion, cm
q_c	contact resistance (ohmic) heat generation rate, W
q_j	joule (ohmic) heat generation rate of solid and electrolyte phases, W
q_r	electrochemical reaction heat generation rate, W
Q	capacity, A s
r	radial coordinate within active material particle, cm
R	universal gas constant, 8.3143 J/mol K
R_f	film resistance on an electrode surface, $\Omega\ cm^2$
R_s	radius of active material particles, cm
Res	residue function
s	Laplace transform variable
T	absolute temperature, K
t	time, s
t_+^{o}	transference number of Li^+ with respect to solvent velocity
U	open circuit, or equilibrium potential of an electrode reaction, V
x	negative electrode solid phase stoichiometry and cell width spatial coordinate, cm
y	positive electrode solid phase stoichiometry and state variable model output

Greek symbol

α_a, α_c	anodic and cathodic transfer coefficients for an electrode reaction
ε	volume fraction or porosity of a phase
λ	eigenvalue, rad/s
η	overpotential of an electrode reaction, V
κ	Li^+ conductivity of electrolyte, S/cm
κ_D	Li^+ diffusional conductivity of electrolyte, A/cm
θ	electrode-averaged stoichiometry
σ	e^- conductivity of electrode solid matrix, S/cm

ϕ	phase potential, V
Ψ	generic physiochemical property
ω	frequency, rad/s

Matrix/Vector

$\mathbf{A},\mathbf{B},\mathbf{C},\mathbf{D}$	state variable model matrices
$\mathbf{L}$	Kalman filter (state estimator) gain matrix
$\mathbf{p},\mathbf{q}$	left eigenvector, right eigenvector
$\mathbf{r}$	residue vector
$\mathbf{u}$	state variable model input vector
$\mathbf{x}$	state vector
$\mathbf{y}$	state variable model output vector
$\mathbf{z}$	steady-state response vector

Subscript

e	electrolyte phase
max	maximum value
ref	with respect to a reference state
s	solid phase
s,avg	electrode-averaged solid phase
s,e	solid/electrolyte interface
sep	separator region
-	negative electrode region
+	positive electrode region
0%	Zero state of charge reference state
100%	100% state of charge reference state

Superscript

eff	effective
Li	lithium species

"But during every day of travel I watched with endless fascination the varieties in the way land could shape its contours and what bearing water and weather had on it and what sorts of plants and animals could love it or at least tolerate it enough to grow from it."

Charles Frazier
Thirteen Moons

Chapter 1 – INTRODUCTION

Batteries directly contribute to the advancement of technologies ranging from portable electronics to fuel-efficient vehicles. When introduced in hybrid electric vehicles (HEVs) for example, the lithium ion (Li-ion) battery chemistry is expected to reduce battery pack weight and volume by a factor of two compared to the nickel metal-hydride chemistry presently used.

Model-based battery monitoring algorithms, of particular importance in high power applications, use current and voltage measurements to estimate state of charge (SOC), available power, and state of health (SOH) with interacting systems basing control action upon these estimates [1]. Despite increased cost, hybrid power system designs must often employ conservative, oversized batteries due to imprecise estimation. The objective of the present work is to develop fundamental models of the Li-ion battery and employ those models in real-time algorithms for accurate battery state estimation and management.

The electrochemical modeling of batteries is fairly well established [2,3] however these high order models (with hundreds of states) are typically only employed offline as they run slower than real-time and can sometimes be unstable. In real-time battery monitoring applications, equivalent circuit models are generally favored for their low order (just 2-5 states) and relative ease of identification [1,4]. These empirical models, however, are unable to predict proximity to side reactions and saturation/depletion conditions responsible for damage and sudden loss of power, respectively, and instead must control the battery within conservative current and voltage limits.

Development of an accurate online electrochemical model is difficult given the nonlinear, infinite-dimensional, distributed mass-transport processes governing battery dynamics [5,6]. A significant challenge for the present work is the one of model order reduction, that is, how we may extract from the governing physical equations a meaningful low order battery model with the stability and execution speed required for real-time application.

In this chapter, we introduce the operating principles of the Li-ion battery and review relevant literature in the areas of fundamental Li-ion battery modeling, model order reduction, and battery estimation/control. The chapter closes with an overview of this dissertation.

1.1 Operating Principles

Figure 1.1 shows a schematic of the Li-ion cell, or battery consisting of three domains: the negative composite electrode, separator, and positive composite electrode. During discharge, Li ions diffuse to the surface of Li_xC_6 active material particles (solid phase) in the negative electrode where they undergo electrochemical reaction

$$Li_xC_6 \underset{\text{charge}}{\overset{\text{discharge}}{\rightleftarrows}} Li_0C_6 + x\mathrm{Li}^+ + x\mathrm{e}^- \qquad (1.1)$$

and transfer into a liquid or gelled electrolyte solution (electrolyte phase). The positively charged ions travel through the electrolyte solution via diffusion and ionic conduction to the positive electrode, where they react

$$Li_0MO_2 + y\mathrm{Li}^+ + y\mathrm{e}^- \underset{\text{charge}}{\overset{\text{discharge}}{\rightleftarrows}} Li_yMO_2 \qquad (1.2)$$

and diffuse towards the inner regions of metal oxide active material particles (solid phase). The porous separator serves as an electronic insulator, forcing electrons to follow an opposite path through an external circuit or load. Both composite electrodes contain binder and filler (not shown in Fig. 1.1) to enhance electron transport across the solid matrix. End of discharge/charge, accompanied by sudden voltage decay/rise, occurs when solid phase Li concentrations at either electrode surface become saturated or depleted, or electrolyte phase Li concentration becomes depleted in either electrode.

Following industry convention, we use “C-rate” terminology to describe current rate. For a typical HEV battery with 6Ah capacity, a 1C (6 Amp) discharge rate is sustainable for roughly 1 hour from the fully-charged (100% SOC) initial condition. In practice, ohmic and transport limitations reduce available capacity to less than the nominal nameplate capacity, particularly at high C-rates. For the 6 Ah HEV battery considered in this work, a 50C (300 Amp) rate is available for just 12 seconds from 100% SOC, having discharged only 1 Ah capacity before negative electrode solid surface concentrations become depleted. Given time for concentration gradients to relax, further discharge is possible at the 50C rate.

1.2 Electrochemical Modeling

Hybrid electric vehicles use a battery as a high rate transient power source cycled about a relatively fixed state of charge (SOC). In the literature, however, most fundamentally-based battery models focus on predicting performance at various constant current discharge rates beginning from the fully charged state [7,8,9]. Cell phone, laptop, and electric vehicle batteries are typically discharged over some hours and it is common in the literature to term discharge rates of only 4C (four times the manufacturer's nominal one hour Ah rating, lasting on the order of 15 minutes) as "high-rate". In contrast, Hitachi states that their 5.5 Ah HEV cell can sustain 40C discharge from 50% SOC for approximately 5 seconds. Phenomenological models capable of capturing ultra-high-rate transient behavior are needed to understand and establish the operating limitations of HEV cells.

Doyle, et al. [2,3] were the first to model the lithium ion cell using porous electrode and concentrated solution theories. Their 1D model captures relevant transport limitations and is general enough to adopt a wide range of active materials and electrolyte solutions with variable properties [7,8,9,10,11]. In [7], Doyle et al. validated the model against constant current data (with rates up to 4C) from similar cells of three different electrode thicknesses. Solid and electrolyte phase mass transport properties were adjusted to fit measured data, and in particular, the solid diffusion coefficient for Li_xC_6 ($D_{s-} = 3.9\text{x}10^{-10}$ cm^2/s) was chosen to capture rate-dependent end of discharge. Interfacial resistance was used as an adjustable parameter to improve the model's fit across the three cell designs. More recently, the 1D isothermal model was validated against a 525 mAh Sony cell phone battery [8]. The authors used a large Bruggeman exponent correcting for tortuosity in the negative electrode ($p = 3.3$) leading to the conclusion that the battery was electrolyte phase limited. Though the model successfully predicted end of discharge for rates up to 3C, the voltage response during the first minutes of discharge did not match and was found to be sensitive to values chosen for interfacial resistances.

While the majority of the modeling literature is devoted to voltage prediction during quasi-steady state constant current discharge and charge, we note several discussions of transient phenomena relevant to HEV cells. Neglecting effects of concentration dependent properties (that generally change modestly with time), the three transient processes occurring in a battery are double-layer capacitance, electrolyte phase diffusion, and solid phase diffusion. Due to the facile kinetics of lithium ion cells, Ong et. al. [12] demonstrated that double-layer effects occur on the millisecond time scale and can thus be neglected for current pulses with frequency less than ~100 Hz.

Unlike double-layer capacitance, electrolyte and solid phase diffusion both influence low frequency voltage response and the relative importance of various diffusion coefficient values can be judged either in the frequency domain [13,14] or through analysis of characteristic time scales [3,11]. Fuller et. al. [11] studied the practical consequence of these transient phenomena by modeling the effect of relaxation periods interspersed between discharge and charge cycles of various lithium ion cells. Voltage relaxation and the effect of repeated cycling were influenced very little by electrolyte concentration gradients and were primarily attributed to equalization of local state of charge across each electrode. Non-uniform active material concentrations would relax via a redistribution process driven by the corresponding non-uniform open-circuit potentials across each electrode.

Thermal behavior of Li-ion batteries is of interest due to their potential for thermal runaway and explosion under high temperature operation. Researchers have approached the problem through both experiment and modeling [15,16,17,18,19,20,21]. Gu and Wang [9] modeled secondary current distributions arising due to temperature gradients within a large electric vehicle battery cooled only from the top. Their 2D electrochemical model considered ohmic and reaction heat generation effects. Srinivasan and Wang [22] subsequently included the entropic heat effect. Nelson et al. [21] used a simpler, lumped-parameter model to explore the ability of HEV cell designs of various geometry to meet PNGV power and thermal requirements. Integrated within a vehicle simulator, the model predicted worst-case system cooling requirements during aggressive driving.

1.3 Model Order Reduction

The fundamental models described above use four coupled partial differential equations (PDEs) to describe species and charge conservation in the solid and electrolyte phases. (Energy conservation is also considered for the non-isothermal models). Standard estimation and control methods [23,24], however, require a dynamic model expressed as a low order set of ordinary differential equations (ODEs), referred to as a state variable model. For a system with input $u(t)$ and output $y(t)$ the general state variable model has linear form

$$\begin{aligned} \dot{\mathbf{x}} &= \mathbf{A}\,\mathbf{x} + \mathbf{B}\,u \\ y &= \mathbf{C}\,\mathbf{x} + \mathbf{D}\,u \end{aligned} \tag{1.3}$$

and nonlinear form

$$\begin{aligned} \dot{\mathbf{x}} &= f(\mathbf{x},u) \\ y &= h(\mathbf{x},u) \end{aligned} \tag{1.4}$$

where $\mathbf{x}(t)$ is the vector of model states. Equivalent circuit models are readily expressed in state variable form. For a circuit built from resistor and capacitor elements, the states $\mathbf{x}(t)$ represent individual capacitor voltages.

Diffusive mass transport processes, with an infinite number of negative real eigenvalues [25], cause batteries to respond across a range of time scales. Karden et al. report battery dynamics as slow as 35 μHz [26], while at very high rates a HEV battery may become solid state diffusion-limited in seconds [27]. Equivalent circuit models with just 2 to 3 states cannot be expected to accurately predict current/voltage behavior across such disparate time scales. By neglecting fast dynamics however, these empirical models may accurately predict low rate discharge behavior [28], or, by neglecting slow dynamics, high rate perturbations within a small SOC range [29]. In the literature, empirical model parameters are commonly fit to a representative data set with little discussion of model bandwidth and region of validity (SOC range, admissible current inputs, etc.).

Representation of an infinite-dimensional diffusion, or parabolic PDE system in matrix ODE form requires some sort of truncation and/or lumping procedure. The response of parabolic PDE systems is generally dominated by a finite number of slow modes and, for control purposes, the eigenspectrum of the spatial differential operator can be partitioned into finite-dimensional (possibly unstable) slow and infinite-dimensional stable fast subspaces [30]. Using this concept, Christophides [25] develops a general approach for robust control of quasi-linear parabolic PDE systems. Galerkin's method approximates the PDE system as a system of ordinary differential equations (ODEs), with the ODE system truncated via singular perturbations. Though their models are not used for control, Bhikkaji and Söderström also reduce the order of 1-D [31] and 2-D [32] diffusion systems via singular perturbation, or what we more generally term modal truncation.

A drawback of Galerkin, collocation, and similar methods is that admissible functions must be identified prior to application of the method, limiting them to systems defined on regular domains. It is often unclear *a priori* which function or method will most efficiently represent a particular problem [33]. While spatial discretization methods such as the finite difference and finite element method are widely applicable to both regular and irregular domains, they generally result in a high order model [25,34]. Karhuenen-Loève decomposition [35], combined with the method of snapshots [36], provides an alternative numerical approach, identifying "empirical" eigenfunctions using time simulation results from a high order finite difference or finite element model. With the dominant eigenfunctions employed as basis functions in a Galerkin procedure, the low degree of freedom model accurately represents the system. Park et al. successfully apply this method in the modeling [34], identification [37], and control [38] of multidimensional linear and nonlinear thermal fluid systems on regular and irregular domains.

The present work takes a similar approach to that of Park, although we numerically identify low order models in the frequency domain rather than time domain. A modal grouping procedure is also developed, providing intuition as to the relationship between high order, possibly infinite-dimensional diffusion systems and the low order approximate models.

1.4 Estimation and Control

State of charge estimation is the classical topic occupying most of the battery estimation literature and good reviews are given by Piller et al. [6] and Pop et al. [39]. Common methods include: (i) Bookkeeping, in which measured voltage is compared to predetermined thresholds, (ii) Coulomb-counting or Amp-hour integration, in which measured current is integrated to carry an initial SOC estimate (generally based upon rest voltage measured at system start-up) forward in time, and (iii) Model-based methods, in which measured current and voltage are compared to a dynamic reference model to determine SOC.

Model-based methods are best suited in dynamic applications, particularly for the HEV application where accurate estimation of available power is far more important than available energy (SOC). Examples include the generalized recursive least squares algorithm of Verbrugge et al. [1] and the extended Kalman filter algorithm of Plett [4]. Both algorithms use an assumed empirical battery model (with 4-5 states) to predict state of charge (SOC) and maximum pulse power available within some fixed, predetermined voltage limits. In pulsed-power applications, fixed current/voltage limits can be overly conservative, particularly for short duration, high-rate current pulses that give rise to large ohmic voltage perturbations [40]. Manufacturers sometimes rate high power batteries with multiple current/voltage limits that depend on the duration of the pulse event [41], although such control limits are difficult to realize in practice.

For the Li-ion battery, physical limits of charge and discharge are saturation/depletion of Li concentration at the electrode surfaces, $c_{s,e}$, and depletion of Li concentration in the electrolyte solution, c_e. To avoid sudden loss of power, Li concentrations must be maintained within constraints

$$0 < \frac{c_{s,e}(x,t)}{c_{s,\max}} < 1 \quad \text{and} \quad c_e(x,t) > 0 .$$

To avoid damaging side reactions, the solid/electrolyte phase potential difference, $\phi_{s-e} = \phi_s - \phi_e$, must be maintained within constraints

$$U_{\substack{side\ rxn, \\ de-insertion}} < \phi_{s-e}(x,t) < U_{\substack{side\ rxn, \\ insertion}}$$

where $U_{side\ rxn}$ is the equilibrium potential of a side reaction occurring when Li ions are either inserted into or de-inserted from active material particles. The reference governor [42], is an effective method to control a system within constraints and has been used, for example, to prevent fuel cell oxygen starvation by dynamically limiting fuel cell load current [43]. In the case of a battery, where only current and voltage can be measured in real time, internal electrochemical states must be estimated based on a fundamental model rather than an empirical model.

As noted earlier, derivation of a dynamic electrochemical model suitable for battery state estimation is difficult given the infinite dimensionality of the underlying partial differential equation (PDE) system. By spatially discretizing the PDEs, fundamental model-based estimation algorithms have been developed for the lead-acid battery [44] and the nickel metal-hydride battery [45], though with high order (30-100 states) compared to equivalent circuit model-based algorithms (2-5 states). Tenno et al. [44] sequentially solve diagonal ODE systems representing lead acid battery distributed concentrations/potentials and use a PID controller to tune model states to match current/voltage measurements during slow discharge. For nickel metal-hydride battery SOC estimation, Barbarisi et al. [45] neglect electrolyte phase and negative electrode solid state transport, assume uniform reaction current, and discretize the positive electrode solid state diffusion PDE (albeit in the incorrect spatial direction) to a 32nd order system of ODEs. Model order reduction techniques offer the potential to provide low order fundamental model-based estimation algorithms without the restrictive assumptions of previous work.

1.5 Overview of the Present Work

In this dissertation, Chapter 2 summarizes the electrochemical [2,3] and thermal [46] model governing equations. For their solution, a previously developed computational fluid dynamics (CFD) model [9] is extended to include transient solid state diffusion, also described in Chapter 2. In Chapter 3, the CFD model is validated with constant current, pulse current, and driving cycle test data provided by DOE/Argonne National Labs from a 6 Ah Li-ion battery designed and built under the FreedomCAR program [47]. Solid state diffusion effects relevant to pulse operation of HEV batteries are discussed. Chapter 4 applies the CFD model to predict battery pack power rate capability and physical limits of operation with respect to DOE Partnership for Next Generation Vehicle (PNGV) goals [48]. The CFD model is integrated into a vehicle simulator to predict battery heat generation rates expected in a midsize HEV passenger car for a range of driving cycles and operating temperatures.

Departing from the CFD model, Chapter 5 develops a frequency domain model order reduction technique for 1D diffusion systems. Transcendental transfer functions (obtained from analytical solution) and numerical transfer matrices (obtained from finite element discretization) are reduced by grouping, or lumping together modes with similar eigenvalues.

The grouped models are compared to optimal models in which the frequency response error between the full and reduced model is minimized in a least-squares sense.

Chapter 6 derives an impedance (frequency domain) model for the complete battery from the governing equations (Chapter 2) under the assumptions of quasi-linear behavior and local reaction current decoupled from electrolyte concentration. The impedance model transfer functions/matrices are reduced to low order state variable models, dominant nonlinearities are explicitly approximated, and the resulting reduced order battery model is validated against CFD model time domain results.

In Chapter 7, a linear Kalman filter based on the reduced order battery model is designed to estimate internal potentials, concentration gradients, and SOC from external current and voltage measurements. A reference current governor predicts operating margin with respect to electrode side reactions and surface depletion/saturation conditions responsible for damage and sudden loss of power. The estimation and reference current control methods are demonstrated with the CFD model and higher order state variable models simulating the plant.

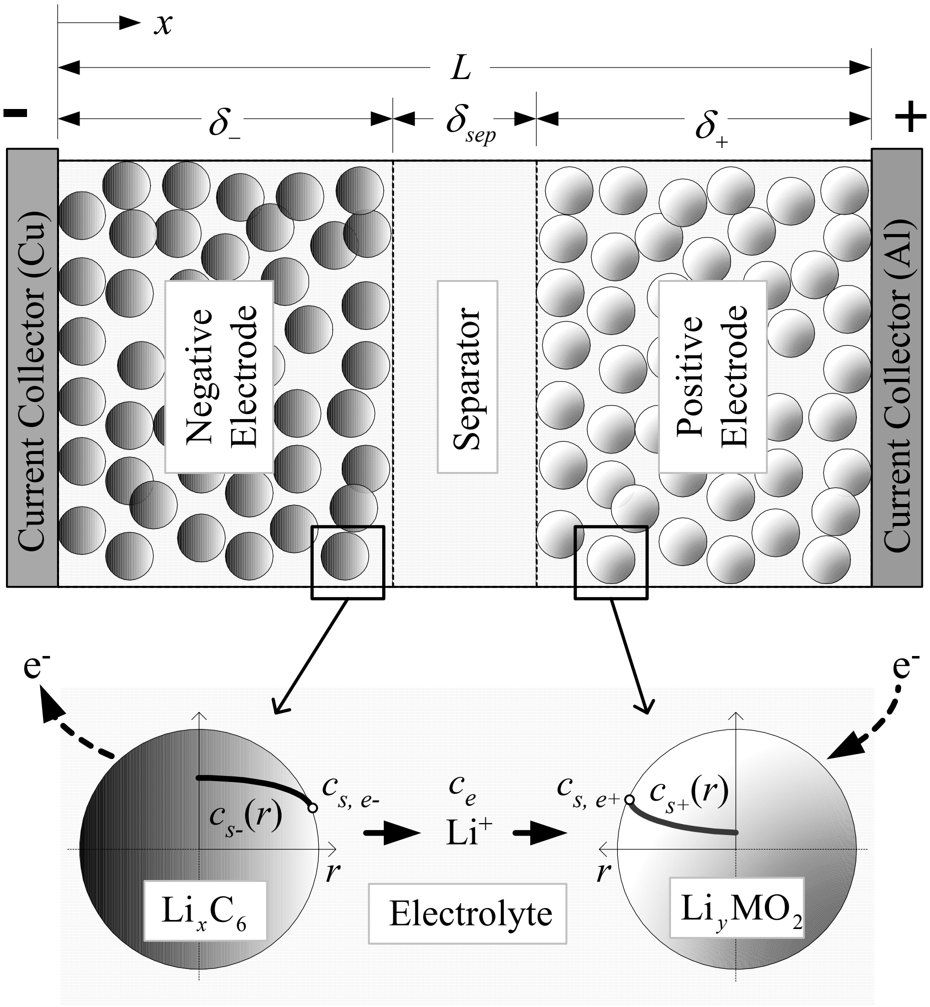

Figure 1.1. Schematic of the Li-ion cell model.

Chapter 2 – MATHEMATICAL MODEL

For the Li-ion battery, the one-dimensional model of Doyle, Fuller, and Newman [2,3] captures relevant solid state and electrolyte diffusion dynamics and accurately predicts current/voltage response. Temperature dependency is considered by coupling the 1-D electrochemical model with a lumped thermal model [46]. Model equations summarized in this chapter serve as the basis for the entire dissertation (though thermal effects are explored only in Chapter 4).

2.1 1-D Electrochemical Model

Composite electrodes are modeled using porous electrode theory, meaning that the solid and electrolyte phases are treated as superimposed continua without regard to microstructure. Conservation of Li in a single spherical active material particle is described by Ficks law of diffusion,

$$\frac{\partial c_s}{\partial t} = \frac{D_s}{r^2}\frac{\partial}{\partial r}\left(r^2 \frac{\partial c_s}{\partial r}\right), \tag{2.1}$$

with boundary conditions

$$\left.\frac{\partial c_s}{\partial r}\right|_{r=0} = 0 \tag{2.2}$$

$$D_s \left.\frac{\partial c_s}{\partial r}\right|_{r=R_s} = \frac{-j^{Li}}{a_s F}. \tag{2.3}$$

In Eqs. (2.1-3), c represents Li concentration and the subscript s denotes the solid phase. D_s is the solid phase diffusion coefficient, j^{Li} the volumetric rate of electrochemical reaction at the particle surface (with $j^{Li} > 0$ indicating ion discharge), a_s the specific interfacial surface area, and F is Faraday's constant (96487 C/mol). For spherical active material particles of radius R_s occupying electrode volume fraction ε_s, the interfacial surface area is $a_s = 3\varepsilon_s/R_s$. Equations (2.1-3) are applied on a continuum basis across each electrode giving solid phase concentration a 2D spatial dependency, i.e. $c_s(x,r,t)$ where x is the particle position, r is the radial position within a particle, and t is time. The electrochemical model depends only upon concentration at the particle surface, $c_{s,e}(x,t) = c_s(x,R_s,t)$, where the subscript s,e denotes the solid/electrolyte interface.

Conservation of Li in the electrolyte phase yields

$$\frac{\partial(\varepsilon_e c_e)}{\partial t} = \frac{\partial}{\partial x}\left(D_e^{eff}\frac{\partial}{\partial x}c_e\right) + \frac{1-t_+^o}{F}j^{Li} \tag{2.4}$$

with zero flux boundary conditions at the current collectors,

$$\left.\frac{\partial c_e}{\partial x}\right|_{x=0} = \left.\frac{\partial c_e}{\partial x}\right|_{x=L} = 0 \tag{2.5}$$

where $c_e(x,t)$ is electrolyte phase Li concentration, ε_e is electrolyte phase volume fraction, and t_+^o is the transference number of Li^+ with respect to the velocity of solvent. The effective diffusion coefficient is calculated from a reference coefficient using the Bruggeman relation $D_e^{eff} = D_e \varepsilon_e{}^p$ that accounts for the tortuous path that Li^+ ions follow through the porous media. Equation (2.4) assumes constant t_+^o.

Charge conservation in the solid phase of each electrode is described by Ohm's law

$$\frac{\partial}{\partial x}\left(\sigma^{eff}\frac{\partial}{\partial x}\phi_s\right) - j^{Li} = 0 \tag{2.6}$$

with boundary conditions at the current collectors proportional to applied current,

$$-\sigma_-^{eff}\left.\frac{\partial \phi_s}{\partial x}\right|_{x=0} = \sigma_+^{eff}\left.\frac{\partial \phi_s}{\partial x}\right|_{x=L} = \frac{I}{A}, \tag{2.7}$$

and zero electronic current at the separator,

$$\left.\frac{\partial \phi_s}{\partial x}\right|_{x=L_-} = \left.\frac{\partial \phi_s}{\partial x}\right|_{x=\delta_- + \delta_{sep}} = 0\,. \tag{2.8}$$

In Eqs. (2.6-8), $\phi_s(x,t)$ and σ^{eff} are the potential and effective conductivity of the solid matrix, respectively, with σ^{eff} evaluated from active material reference conductivity σ as $\sigma^{eff} = \sigma\,\varepsilon_s$. A is electrode plate area and $I(t)$ is the applied current following the sign convention that a positive current discharges the battery.

Electrolyte phase charge conservation yields

$$\frac{\partial}{\partial x}\left(\kappa^{eff}\frac{\partial}{\partial x}\phi_e\right)+\frac{\partial}{\partial x}\left(\kappa_D^{eff}\frac{\partial}{\partial x}\ln c_e\right)+j^{Li}=0 \tag{2.9}$$

with boundary conditions

$$\left.\frac{\partial \phi_e}{\partial x}\right|_{x=0}=\left.\frac{\partial \phi_e}{\partial x}\right|_{x=L}=0\,. \tag{2.10}$$

In Eqs. (2.9-10), $\phi_e(x,t)$ is the electrolyte phase potential and κ^{eff} the effective ionic conductivity, calculated from the Bruggeman relation $\kappa^{eff}=\kappa\,\varepsilon_e{}^{p}$. Derived from concentrated solution theory, effective diffusional conductivity is

$$\kappa_D^{eff}=\frac{2RT\kappa^{eff}}{F}(t_+^0-1)\left(1+\frac{d\ln f_\pm}{d\ln c_e}\right) \tag{2.11}$$

where R is the universal gas constant (8.3143 J/mol K), T is temperature, and $f_\pm$ is the activity coefficient, assumed in the present work to be constant.

The four governing PDEs (2.1), (2.4), (2.6), and (2.9) describing field variables, $c_{s,e}$, c_e, ϕ_s, and ϕ_e, are coupled by the Butler-Volmer electrochemical kinetic expression

$$j^{Li}=a_s i_o\left\{\exp\left[\frac{\alpha_a F}{RT}\eta\right]-\exp\left[-\frac{\alpha_c F}{RT}\eta\right]\right\}. \tag{2.12}$$

In Eq. (2.12), j^{Li} is driven by overpotential, η, defined as the difference between solid and electrolyte phase potentials minus the thermodynamic equilibrium potential, U, of the solid phase

$$\eta=\phi_s-\phi_e-U\,. \tag{2.13}$$

Equilibrium potential, $U(c_{s,e})$, is a function of the solid phase concentration at the particle surface. In Eq. (2.12), exchange current density, i_0, is related to both solid surface and electrolyte concentrations according to

$$i_0=k(c_e)^{\alpha_a}(c_{s,\max}-c_{s,e})^{\alpha_a}(c_{s,e})^{\alpha_c} \tag{2.14}$$

where k is a kinetic rate constant and α_a and α_c are the anodic and cathodic transfer coefficients, respectively.

With boundary conditions applied galvanostatically (2.7), cell current, $I(t)$, is model input. Voltage across the cell terminals is calculated as

$$V(t) = \phi_s(L,t) - \phi_s(0,t) - \tfrac{R_f}{A} I(t) \tag{2.15}$$

where R_f is an empirical contact resistance.

2.2 Lumped Thermal Model

Physiochemical property values are made temperature dependent, coupling the 1-D electrochemical model to the lumped thermal model. An Arrhenius equation defines the temperature sensitivity of a general physiochemical property, Ψ , as

$$\Psi = \Psi_{ref} \exp\left[\frac{E_{act}^{\Psi}}{R} \left(\frac{1}{T_{ref}} - \frac{1}{T} \right) \right] \tag{2.16}$$

where Ψ_{ref} is the property value defined at reference temperature T_{ref} = 25˚C. Activation energy, E_{act}^{Ψ}, controls the temperature sensitivity of each individual property, Ψ .

Conservation of energy for a Li-ion cell with lumped thermal capacity balances heat accumulation, convective dissipation, and generation terms as

$$\frac{d(\rho c_p T)}{dt} = hA_s(T - T_\infty) + (q_r + q_j + q_c) \tag{2.17}$$

describing the evolution of cell temperature, T, with time. In Eq. (2.17), h is the heat transfer coefficient for forced convection from each cell, A_s is the cell surface area exposed to the convective cooling medium (typically air), and T_∞ is the free stream temperature of the cooling medium.

Total heat generated is taken as the sum of reaction and joule (ohmic) heats. Local reaction heat is equal to reaction current, j^{Li}, times overpotential, η. The total reaction heat, q_r, is obtained by integrating across the 1-D cell domain

$$q_r = A \int_0^L j^{Li} (\phi_s - \phi_e - U)\, dx\,. \tag{2.18}$$

Note that there is no reaction, and thus no reaction heat generated in the separator region.

Local ohmic heats arise from the current in each phase carried with finite conductivity. This i^2R (or i^2/σ)-type heating is expressed in terms of potential gradients by utilizing the conservation of charge relationship for each phase. Total ohmic heat, q_j, across the 1-D cell domain is

$$q_j = A\int_0^L \sigma^{eff}\left(\frac{\partial\phi_s}{\partial x}\right)^2 + \kappa^{eff}\left(\frac{\partial\phi_e}{\partial x}\right)^2 + \kappa_D^{eff}\left(\frac{\partial \ln c_e}{\partial x}\right)\left(\frac{\partial\phi_e}{\partial x}\right) dx\,. \tag{2.19}$$

The first term inside the integral of Eq. (2.19) expresses ohmic heat of the solid phase; the second and third terms express that of the electrolyte phase. Note that while the first and second terms are always positive, the third term is generally negative, since Li^+ ions carried via diffusion in the electrolyte solution reduce the ionic current (migration) in the electrolyte phase.

Additional ohmic heat arises due to contact resistance, R_f, between current collectors and electrodes. Total heat generated in the cell due to contact resistance, q_c, is

$$q_c = I^2\frac{R_f}{A}\,. \tag{2.20}$$

Since contact resistance, R_f, represents an empirical parameter in an otherwise fundamentally-based model we list q_c separately in Eq. (2.17) from the previously mentioned ohmic heats, q_j.

Reversible heating is neglected in the present work. Srinivasan and Wang [22] incorporated empirical data from Li_xC_6 and Li_yMnO_4 electrodes into a 2-D Li ion cell model and showed the reversible heating effect, important at low discharge rates, to be dominated by irreversible (reaction and ohmic) heating at high discharge rates relevant to automotive applications. For the typical HEV application where the battery is alternately pulse-discharged and charged about a fixed SOC, reversible heats will alternately heat and cool the cell and, over time, the net reversible heat will be near zero.

2.3 CFD Model Numerical Implementation

The nonlinear governing PDEs and constitutive relationships are numerically solved within a computational fluid dynamics (CFD) framework. (This dissertation builds upon the CFD model previously developed by Gu and Wang [9] by including transient solid state diffusion effects.) The 1-D macroscopic domain is discretized into approximately 50 control volumes. Described in Appendix A, a finite element solution to the transient solid state diffusion problem, Eqs. (2.1-3), is separately applied within each control volume of the negative and positive electrodes. For input current $I(t)$, the five governing equations are solved simultaneously for field variables $c_e(x,t)$, $c_{s,e}(x,t)$, $\phi_e(x,t)$, and $\phi_s(x,t)$, and lumped cell temperature $T(t)$.

Chapter 3 – SOLID STATE DIFFUSION LIMITATIONS ON PULSE OPERATION[*]

The CFD model described in Chapter 2 is validated against constant current and hybrid pulse power characterization (HPPC) experimental data from a 6 Ah cell designed for hybrid electric vehicle (HEV) application. Reaction current distribution and redistribution processes occurring during discharge and current interrupt, respectively, are driven by gradients in equilibrium potential that arise due to solid diffusion dynamics. The model is extrapolated to predict voltage response at discharge rates up to 40C (240 A) where end of discharge is caused by negative electrode active material surface concentrations near depletion. Simple expressions are derived from an analytical solution to describe solid state diffusion limited current for short duration, high rate pulses. The suitability of various solid state diffusion solution methods is addressed.

3.1 Electrochemical Model Parameterization

Low-rate constant current discharge/charge, hybrid pulse power characterization (HPPC), and transient driving cycle data [47] were provided by the DOE FreedomCAR program for a 276V nominal HEV battery pack consisting of 72 serially-connected cells. For the purpose of HEV systems integration modeling, we were tasked to build a mathematical model of a single cell of that pack and present all data on a single cell basis by dividing measured pack voltage by 72. Due to the proprietary nature of the prototype FreedomCAR battery we were unable to disassemble cells to measure geometry, composition, etc. and therefore adopt values from the literature and adjust them as necessary to fit the data.

By expressing capacity of the negative and positive electrodes as

$$\begin{aligned} Q_- &= \varepsilon_{s-}(\delta_- A)(c_{s,\max -})(\Delta x)F \\ Q_+ &= \varepsilon_{s+}(\delta_+ A)(c_{s,\max +})(\Delta y)F, \end{aligned} \tag{3.1}$$

low-rate capacity data provides a rough gauge of electrode volume and stoichiometry cycling range, assuming electrode composition and electrode mass ratio from [2]. This mass ratio is later shown to result in a well-balanced cell at both high and low rates. Discharge capacity at

---

[*] This chapter adapted from: K. Smith, C.-Y. Wang, "Solid-state diffusion limitations on pulse operation of a lithium ion cell for hybrid electric vehicles," *J. Power Sources*, 161 (2006) 628-639.

the 1C (6 Amp) rate was measured to be 7.2 Ah and we define stoichiometry reference points for 0% and 100% SOC (listed in Table 3.1) on a 7.2 Ah basis.

The negative electrode active material almost certainly consists of graphite (Li_xC_6) given its widespread use in reversible lithium ion cells. Shown in Fig. 3.1, we use the empirical correlation for Li_xC_6 open circuit potential, U_-, from [8]. The positive electrode active material could consist of $Li_yMn_2O_4$, Li_yCoO_2, Li_yNiO_2, or some combination of metal oxides. Listed in Table 3.1, we fit our own correlation for U_+ by subtracting U_- from the cell's measured open circuit voltage.

Figure 3.2 compares the model using parameters listed in Table 3.1 to 1C (6 Amp) constant current discharge and charge data. This low rate data set is relatively easy to fit as it deviates little from open circuit voltage.

In contrast, the voltage perturbation of the transient HPPC data set is more difficult to fit. The HPPC test procedure, defined in [47], consists of a 30 A discharge for 18 seconds, open-circuit relaxation for 32 seconds, 22.5 A charge for 10 seconds, followed by open-circuit relaxation as shown in the top window of Fig. 3.3. The onset of constant current discharge and charge portions of the HPPC profile are accompanied by brief (0.1 second) high-rate pulses to estimate high frequency resistance. Unable to decouple values of SEI layer resistance from contact film resistance (or cell-to-cell interconnect resistance for that matter), we fit ohmic perturbation using a contact film resistance of $R_f = 20\ \Omega\ cm^2$.

Neglecting double layer capacitance (whose transient effects occur on a millisecond time-scale [8]) the only transient phenomena accounted for in the mathematical model [2,3] are electrolyte diffusion and solid diffusion. A parametric study showed that while it was possible to match the observed voltage drop at the end of the HPPC 30 A discharge by lowering D_e several orders of magnitude from a baseline value of $2.6x10^{-6}\ cm^2\ s^{-1}$ [8], the voltage drop at short times was too severe. Significant decrease in D_e also caused predicted voltage to diverge from the measured voltage over time due to severe electrolyte concentration gradients. While recent $LiPF_6$-based electrolyte property measurements [49] show diffusion coefficient, D_e, and activity coefficient, $f_\pm$, both exhibiting moderate concentration dependency, it is beyond the scope of this work to consider anything beyond the first approximation of constant D_e and unity $f_{\pm}$.

In investigating solid state diffusion transient effects, we note that measured voltage response only allows observation of characteristic time $t = R_s^2/D_s$ and will not provide R_s and D_s independently. SEM images, such as that shown by Dees et al. [50] (their Fig. 1) of a $LiNi_{0.8}Co_{0.15}Al_{0.05}O_2$ composite electrode, often show bulk or "secondary" active material particles (with radii ~5 µm) having finer "primary" particles (with radii ~0.5 µm) attached to the surface. Dees achieved good description of $LiNi_{0.8}Co_{0.15}Al_{0.05}O_2$ impedance data in the 0.01 to 1 Hz frequency range using a characteristic diffusion length of 1.0 µm. As active material composition and structure are unknown for the present cell, we adopt this value as the particle radius in both electrodes.

Though Li_xC_6 is often reported to have more sluggish diffusion than common positive electrode active materials, a parametric study on D_{s-} using the transient solid diffusion model found no value capable of describing both the ~0.047 V drop in cell voltage from 2 to 20 seconds of the HPPC test as well as the slow voltage relaxation upon open-circuit at 20 seconds. Assuming for the moment that the ~0.047 V drop is caused solely by solid diffusion limitations in the negative electrode, we estimate that surface concentration $c_{s,e-}$ would need to fall from its initial value by $4.3\text{x}10^{-4}$ mol cm^{-3} (a substantial amount) to cause the observed 0.047 V change in U_-. Wang et. al. [46] give an empirical formula for the evolution of a concentration gradient within a spherical particle subjected to constant surface flux as

$$c_{s,e}(t) - c_{s,avg}(t) = j^{Li}\frac{-R_s}{5a_sFD_s}\left[1-\exp\left(-\tfrac{20}{3}\sqrt{D_st}/R_s\right)\right]. \tag{3.2}$$

At steady state (where the exponential term goes to zero) and with the assumption of uniform reaction current, $j_-^{Li} = I/A\delta_-$, we manipulate Eq. (3.2) to obtain a rough estimate of the negative electrode diffusion coefficient,

$$D_{s-} = \frac{R_s}{5Fa_s\Delta c_{s-}}\frac{I}{A\delta_-} \tag{3.3}$$

of $1.6\text{x}10^{-12}$ cm^2 s^{-1}. A corresponding characteristic time whereby the operand of the exponential term in Eq. (3.2) equals unity is 140 seconds. Our conclusion is that, while a negative electrode solid diffusion coefficient of $D_{s-} = 1.6\text{x}10^{-12}$ cm^2 s^{-1} might cause the cell voltage to drop ~0.047 V, that voltage drop would take much longer to develop than what we observe in the data. Repeating calculations for concentration gradient magnitude and characteristic time under a variety of conditions revealed that the observed transient behavior might be described by solid state diffusion in the negative electrode if the slope $\partial U_- / \partial c_{s-}$ were roughly 8 times steeper. This is indeed the case in the positive electrode, where at 50% SOC the open circuit potential function has almost 7x greater slope with respect to concentration than the negative electrode. Chosen via parametric study, final values of D_{s-} ($2.0\text{x}10^{-12}$ cm^2 s^{-1}) and D_{s+} ($3.7\text{x}10^{-12}$ cm^2 s^{-1}) represent HPPC voltage dynamics in Fig. 3.3 quite well, although we note they are dependent upon our choice of particle radius. Were we to chose particle radii of 5 μm rather than 1 μm, our diffusion coefficient would be 25x higher to maintain characteristic time $t = R_s^2/D_s$ and match the voltage dynamics of the HPPC test.

Figure 3.4 quantifies voltage polarization resulting from diffusive transport by individually raising each diffusion coefficient by 5 or more orders of magnitude such that it no longer affects cell voltage response. Despite comparable values of D_{s-} and D_{s+}, the positive electrode polarizes transient voltage response more significantly due to its stronger open-circuit potential coupling.

Figure 3.5 compares model voltage prediction to data taken on the FreedomCAR battery whereby an ABC-150 battery tester was used to mimic a power profile recorded from a Toyota Prius HEV on a federal urban (FUDS) driving cycle. Only the first 150 seconds are shown, though results are representative of the entire test.

3.2 Electrode Dynamics

Despite aforementioned uncertainties in cell design and choice of model parameters, the model is still useful in elucidating pulse discharge and charge dynamics resulting from solid state transport limitations. As a basis for the subsequent discussion we use simulation results from the first 30 seconds of the 58.3% SOC HPPC case (whose voltage response is denoted with circles in Fig. 3.3).

Approximately one second into the test, a 30 A discharge current is applied resulting in the step change in local reaction current, j^{Li}, shown in Fig. 3.6. At the onset of the step change, solid phase surface concentrations are uniform and the initial distribution of reaction across each electrode is governed by relative magnitudes of exchange current density, electrolyte phase conductivity, and solid phase conductivity. The solid phase is a much better conductor than the electrolyte phase and the reaction is distributed such that Li^+ ions favor a path of least resistance, traveling the shortest distance possible in the electrolyte phase. Negative electrode reaction is less evenly distributed than positive electrode reaction predominantly due to the greater solid phase conductivity of the negative electrode ($\sigma_- = 1.0$ S/cm vs. $\sigma_+ = 0.1$ S/cm).

As a consequence of the initial peak in reaction current at the separator interface, Li surface concentration changes most rapidly at that location in each electrode, as shown in Fig. 3.7. The effect is more pronounced in the negative electrode where the larger initial peak in current density quickly causes a gradient in active material surface concentration, $\partial c_{s,e} / \partial x$, to build across that electrode. Local equilibrium potential, U_-, falls most rapidly at the negative electrode/separator interface, penalizing further reaction at that location and driving the redistribution of reaction shown in Fig. 3.6. As discharge continues, progressively less reaction occurs at the separator interface and more reaction occurs at the current collector interface.

Positive electrode reaction current exhibits similar redistribution, though less significant than in the negative electrode. The positive electrode open-circuit potential function is almost 7 times more sensitive to changes in concentration than the negative electrode function at 58.3% SOC. Small changes in positive electrode active material surface concentration significantly penalize reaction, and for this reason, redistribution of reaction due to solid diffusion limitations occurs much quicker in that electrode.

Redistribution of Li also occurs upon cell relaxation at the end of the 18 second-long 30 A discharge. Figure 3.6 shows a second step change in transfer current density around 19 seconds, appearing qualitatively as the mirror image of the step change at 1 second when the galvanostatic load was first applied. At locations near the separator, a recharging process begins while at locations near the current collector, discharge continues even after the load is removed. The process is driven by the gradient in local equilibrium potential, $\partial U / \partial x$ (directly related to the solid phase surface concentration gradient, $\partial c_{s,e} / \partial x$) and continues until surface concentrations, $c_{s,e}$, are once again evenly distributed. During this redistribution process the net balance of reaction across each electrode is zero.

Relaxation reaction redistribution is less significant in the positive electrode, where only a minimal solid phase surface concentration gradient, $\partial c_{s,e+} / \partial x$, arose during the 30 A discharge. The process lasts on the order of 10 seconds, compared to several minutes for the negative electrode. In both electrodes, solid phase bulk concentrations rise and fall at roughly the same rate as surface concentrations throughout the redistribution process, indicating that the time scale of reaction redistribution is much faster than solid phase diffusion. Localized concentration gradients within individual solid particles (from bulk to surface), $\partial c_s / \partial r$, relax so slowly that the 63 second long pulse power test amounts to little more than a transient discharge and charge on the surface of the active material particles with inner bulk regions unaffected.

3.3 Rate Capability

Figure 3.8 presents model-predicted constant current discharge capability from 50% SOC. Shown in the bottom window of Fig. 3.8, a 40C rate current (240 A) can be sustained for just over 6 seconds before voltage decays to the 2.7 V minimum. The top window of Fig. 3.8 shows active material surface concentration in the negative (left axis) and positive (right axis) electrodes at the end of discharge across the range of discharge rates. Electrode-averaged rather than local values of surface concentration are presented to simplify the discussion. The electrodes are fairly well balanced, indicated by end of discharge surface concentrations near depletion and saturation in the negative and positive electrodes, respectively. End of discharge voltage is predominantly negative electrode-limited as stoichiometries of $x = c_{s,e} / c_{s,max-} < 0.05$ causes a rapid rise in U_-. Surface active material utilization decreases slightly with increasing C-rate due to increased ohmic voltage drop. In the present model, electrolyte Li^+ transport is sufficiently fast that electrolyte depletion does not play a limiting role at any discharge rate from 50% SOC. In the worst case of 30C, the minimum value of local electrolyte concentration, occurring at the positive electrode/current collector interface, is around 50% of average concentration, $c_{e,0}$. For rates less than 30C, the reduced current level results in lesser electrolyte concentration gradients, while for rates greater than 30C, the shorter duration of discharge time results in a smaller concentration gradient at end of discharge. If we induce sluggish diffusion by reducing D_e (a similar effect may be induced in cell design by reducing porosity), electrolyte concentration in the positive electrode comes closer to depletion with the worst case minimum value of c_e occuring at lesser current rates. Lowering D_e by one order of magnitude for example, results in a battery limited in the 10C to 20C range by electrolyte phase transport, with higher and lower current rates still controlled by solid state transport.

3.4 Solid State Diffusion-Limited Current

Under solid phase transport limitations, simple relationships may be derived to predict maximum current available for a given pulse time. Substituting dimensionless variables

$$\bar{r} = \frac{r}{R_s}, \quad \tau = \frac{D_s t}{R_s^{\,2}}, \quad \bar{c}_s(\bar{r},\tau) = \frac{c_s(\bar{r},\tau) - c_{s,0}}{c_{s,\max}}, \quad \bar{j}^{Li} = \frac{j^{Li} R_s}{D_s a_s F c_{s,\max}} \tag{3.4}$$

into Eq (2.1) yields the dimensionless governing equation

$$\frac{\partial \bar{c}_s}{\partial \tau} = \frac{1}{\bar{r}^2} \frac{\partial}{\partial \bar{r}} \left(\bar{r}^2 \frac{\partial \bar{c}_s}{\partial \bar{r}} \right) \tag{3.5}$$

with initial condition $\bar{c}_s(\bar{r}, \tau = 0) = 0 \;\; \forall \;\; \bar{r}$ and boundary conditions

$$\left. \frac{\partial \bar{c}_s}{\partial \bar{r}} \right|_{\bar{r}=0} = 0, \qquad \left. \frac{\partial \bar{c}_s}{\partial \bar{r}} \right|_{\bar{r}=1} = \bar{j}^{Li}. \tag{3.6}$$

The solution given by Carslaw and Jaeger [51] is

$$\bar{c}_s(\bar{r},\tau) = -\bar{j}^{Li} \left[3\tau + \tfrac{1}{10}(5\bar{r}^2 - 3) - \frac{2}{\bar{r}} \sum_{n=1}^{\infty} \frac{\sin(\lambda_n \bar{r}) \exp(-\lambda_n^{\,2} \tau)}{\lambda_n^{\,2} \sin(\lambda_n)} \right], \tag{3.7}$$

where the eigenvalues are roots of $\lambda_n = \tan(\lambda_n)$. Figure 3.9 shows distribution of Li concentration along the radius of an active material particle during galvanostatic discharge or charge for dimensionless times ranging from $\tau = 10^{-6}$ to 10^{-1} which, for reference, correspond to current pulses lasting 0.05 to 500 seconds using negative electrode parameters from Table 3.1.

Surface concentration and depth of penetration into the active material, both of practical interest for HEV pulse-type operation, can be obtained from Eq. (3.7). Surface concentration, shown for the present model to cause end of discharge as the negative electrode nears depletion, is calculated by evaluating Eq. (3.7) at $\bar{r} = 1$. Penetration depth, ℓ, providing a measure of active material accessible for short duration pulse events, is calculated by finding the point along the radius where the concentration profile is more or less equal to the initial condition. A 99% penetration depth, $\ell = R_s - r$, is defined using the location *r* resulting in a root of the formula

$$\frac{\bar{c}_s(\bar{r},\tau)}{\bar{c}_s(1,\tau)} = 1 - a \tag{3.8}$$

with $a = 0.99$. Expressed as a fraction of total radius, dimensionless penetration depth, $\bar{\ell} = \ell / R_s$, is a function of dimensionless time only.

Empirical expressions for dimensionless surface concentration, $\bar{c}_{s,e}$, and dimensionless penetration depth, $\bar{\ell}$, are fit to the results of Eq. (3.7) and presented in Table 3.2. Functions of the form $f(\tau) = C\sqrt{\tau}$ provide good resolution at short times of $\tau < 10^{-3}$, corresponding in our model to pulses lasting fewer than ~5 seconds. Resolution may be extended one to two orders of magnitude in τ using functions of the form $f(\tau) = C\sqrt{\tau} + D\tau$.

Equation (3.19) in Table 3.2 may be used in lieu of the present electrochemical model to predict negative electrode surface concentrations for pulses shorter than 400 seconds, or, conversely, to predict limiting currents at rates greater than ~9C caused by depleted active material surface concentration at end of discharge. By combining Eqs. (3.4) and (3.19) under the assumption of uniform current density, $j_-^{Li} = I / A\delta_-$, we obtain an empirical relationship for surface concentration as a function of current and time

$$\frac{c_{s,e}(t)}{c_{s,\max -}} = \frac{c_{s,0}}{c_{s,\max -}} - I \frac{R_{s-}}{\delta_- A D_{s-} a_{s-} F c_{s,\max -}} \left[1.122 \frac{\sqrt{D_{s-} t}}{R_{s-}} + 1.25 \frac{D_{s-} t}{R_{s-}^{\;2}} \right] \tag{3.9}$$

valid for $t < 0.08 D_s / R_s^2$. Alternatively, given initial stoichiometry, x_0, and surface stoichiometry at end of discharge, $x_{s,e\,final}$, the maximum current available for a pulse discharge lasting t seconds will be

$$I_{\max} = \left(x_0 - x_{s,e\,final}\right)\left(\frac{\delta_- A a_{s-} F c_{s,\max-}}{\frac{1.122}{\sqrt{D_{s-}}}\sqrt{t} + \frac{1.25}{R_{s-}}t}\right). \tag{3.10}$$

While the theoretical maximum current will be obtained under the condition $x_{s,e\,final} = 0$, i.e. complete surface depletion, Fig. 3.8 showed the present model to exhibit an end of discharge surface stoichiometry around 0.03, with some rate dependency. Under uniform initial conditions, the initial stoichiometry, x_0, is simply a function of SOC. For a recently charged or discharged battery with nonuniform initial concentration, a better prediction of maximum pulse current may be obtained by replacing x_0 in Eq. (3.10) with a stoichiometry averaged across the penetration depth or "pulse-accessible" region [52].

3.5 Solid State Diffusion Approximations for Electrochemical Modeling

Discussed in Chapter 2 and detailed in Appendix A, the present CFD model utilizes a 5th order finite element approximation for solid state diffusion, Eq. (2.1), and incorporates that submodel into the 1-D electrochemical model as a finite difference equation, that is, local values of $c_{s,e}$ are calculated using values of $c_{s,e}$ and j^{Li} from the previous 5 time steps

$$c_{s,e}^{[k]} = f\left([c_{s,e}^{[k-1]}, \dots c_{s,e}^{[k-5]}], [j^{Li[k]}, \dots j^{Li[k-5]}] \right). \tag{3.11}$$

Here we compare the finite element submodel to the analytical solution employed by Doyle et. al. [2] and the polynomial profile model of Wang et. al. [53]. Comparisons are made in the frequency domain in order to remove the influence of a particular type of input (pulse current, current step, constant current, etc.) by taking the Laplace transform of each time domain model, expressing the input/output relationship as a transfer function in the Laplace variable s, and substituting $s = j\omega$ to calculate the complex impedance at frequency ω. A capitalized variable denotes that variable's Laplace transform, that is, $C_{s,e}(s) = L\{c_{s,e}(t)\}$, and an overbar denotes a dimensionless variable. Define

$$\overline{C}_{s,e}(s) = \frac{C_{s,e}(s) - c_{s,0}}{c_{s,\max}}, \quad \overline{J}^{Li}(s) = J^{Li}(s)\frac{R_s}{a_s F D_s c_{s,\max}}, \quad \overline{\omega} = \omega\frac{R_s^{\,2}}{D_s}. \tag{3.12}$$

In the Laplace domain, a compact analytical solution to Eq. (2.1) is readily available. The exact transfer function expressing dimensionless surface concentration vs. dimensionless reaction current given by Jacobsen and West [54] is

$$\frac{\overline{C}_{s,e}(s)}{\overline{J}^{Li}(s)} = \frac{\tanh(\psi)}{\tanh(\psi) - \psi} \tag{3.13}$$

where $\psi = R_s \sqrt{s/D_s}$.

Doyle et. al. [2] provide two analytical series solutions in the time domain, one for short times and one for long times. In Appendix B, we manipulate Doyle's formulae to arrive at the short time transfer function

$$\frac{\overline{C}_{s,e}(s)}{\overline{J}^{Li}(s)} = \left[1 - \psi + 2\psi \sum_{n=1}^{\infty} \exp(-2n\psi)\right]^{-1} \tag{3.14}$$

and the long time transfer function

$$\frac{\overline{C}_{s,e}(s)}{\overline{J}^{Li}(s)} = \left[-2\sum_{n=1}^{\infty} \frac{\psi^2}{\psi^2 + (n\pi R_s)^2 / D_s}\right]^{-1} . \tag{3.15}$$

The frequency response (magnitude and phase angle) of truncated versions of the short and long time transfer functions are compared to the exact transfer function (3.13) in Fig 3.10, showing the short time solution to provide good agreement at high frequencies and the long time solution at low frequencies. Note that the short time transfer function does not change much beyond the first term of the series. A good strategy to piece together Doyle's two solutions is to use one term of the short time solution for $\tau = D_s t / R_s^2 \leq 0.1$ (corresponding to $\overline{\omega} \geq 6\text{x}10^1$ in Fig. 3.10) and around 100 terms of the long time solution for $\tau > 0.1$.

Reaction current appears in Eq. (2.1) as a time dependent boundary condition which Doyle accommodates using a Duhamel superposition integral. Numerical solution of this convolution-type integral requires that a time history of all previous step changes in surface concentration be held in memory and called upon at each time step to reevaluate the integral. So while the analytical solution is inarguably the most accurate approach, it can be expensive in terms of memory and computational requirements, particularly in situations requiring a small time step but long simulation time (driving cycle simulations, for instance) or in situations requiring a large grid mesh (2-D or 3-D simulations incorporating realistic cell geometry, for instance).

Approximate solutions to Eq. (2.1) are appropriate so long as they capture solid state diffusion dynamics sufficiently fast for a particular investigation. Wang et. al. [53] assume the concentration profile within the spherical particle is described by a parabolic profile $c_s(r,t) = A(t) + B(t)r^2$, and thus formulate a solid state diffusion submodel which correctly captures bulk dynamics and steady state concentration gradient, but otherwise neglects diffusion dynamics. Derived in Appendix C, the transfer function of the parabolic profile, or steady state diffusion, model is

$$\frac{\overline{C}_{s,e}(s)}{\overline{J}^{Li}(s)} = \frac{3}{\psi^2} + \frac{1}{5}. \tag{3.16}$$

Shown in Fig. 3.11 versus the exact transfer function (3.13), the parabolic profile model is valid for low frequencies, $\overline{\omega} < 10$, or long times, $\tau = D_s\, t / R_s^2 > 0.6$. Substituting values from the present model's negative electrode ($D_{s-} = 2.0\text{x}10^{-12}$ cm^2 s^{-1}, $R_{s-} = 1.0\text{x}10^{-4}$ cm), the parabolic profile model would correctly predict surface concentration only at times longer than 3000 seconds. For electrochemical cells with sluggish solid state diffusion, the parabolic profile model will correctly capture low rate end of discharge behavior, but is generally inappropriate in the modeling of high rate (>2C) or pulse type applications [55].

We find spatial discretization of Eq. (2.1) yields low order solid state diffusion models with more accurate short time prediction compared to polynomial profile models [56]. Recasting the 5th order finite element model from Appendix A in nondimensional form,

$$\frac{\overline{C}_{s,e}(s)}{\overline{J}^{Li}(s)} = a_s F \frac{D_s}{R_s}\left[\frac{b_1 s^5 + b_2 s^4 + b_3 s^3 + b_4 s^2 + b_5 s + b_6}{a_1 s^5 + a_2 s^4 + a_3 s^3 + a_4 s^2 + a_5 s + a_6}\right], \tag{3.17}$$

Fig. 3.11 shows the present model to provide good approximation of the exact transfer function for $\overline{\omega} < 10^5$, and thus be valid for dimensionless times $\tau > 6\text{x}10^{-5}$ (or $t > 0.3$ s for the present model's negative electrode). Regardless of what solution technique is employed for solid state diffusion in an electrochemical cell model, if the objective is to match high rate (~40C) pulse behavior and predict transport limitations on a short (~5 second) time scale, that technique must be valid at very short times.

3.6 Conclusions

A 5th order finite element model for transient solid state diffusion is incorporated into a previously developed 1-D electrochemical model and used to describe low rate constant current, hybrid pulse power characterization, and transient driving cycle data sets from a 6 Ah Li-ion HEV battery. HEV battery models in particular must accurately resolve active material surface concentration at very short dimensionless times. Requirements for the present model are $\tau = D_s\, t / R_s^2 \approx 10^{-3}$ to predict 40C rate capability and $\tau \approx 2\text{x}10^{-5}$ to match current/voltage dynamics at 10 Hz.

Dependent on cell design and operating condition, end of pulse discharge may be caused by negative electrode solid phase Li depletion, positive electrode solid phase Li saturation, or electrolyte phase Li depletion. Simple expressions developed here for solid state diffusion-limited current, applicable in either electrode, may aid in the interpretation of high rate experimental data. While the present work helps to extend existing literature into the dynamic operating regime of HEV batteries, future work remains to fully characterize an HEV battery in the laboratory and develop a fundamental model capable of matching current/voltage data at very high rates.

Parameter	Negative Electrode	Separator	Positive Electrode
Design Specifications (Geometry & Volume Fractions)			
Thickness, δ [cm]	$50\text{x}10^{-4}$	$25.4\text{x}10^{-4}$	$36.4\text{x}10^{-4}$
Particle radius, R_s [cm]	$1\text{x}10^{-4}$		$1\text{x}10^{-4}$
Active material volume fraction, ε_s	0.580		0.500
Polymer phase volume. fraction, ε_p	0.048	0.5	0.110
Conductive filler volume. fraction, ε_f	0.040		0.06
Porosity (electrolyte phase volume fraction), ε_e	0.332	0.5	0.330
Solid & Electrolyte Phase Li Concentrations			
Maximum solid phase concentration $c_{s,max}$ [mol cm^{-3}]	$16.1\text{x}10^{-3}$		$23.9\text{x}10^{-3}$
Stoichiometry at 0% SOC, $x_{0\%}$, $y_{0\%}$	0.126		0.936
Stoichiometry at 100% SOC, $x_{100\%}$, $y_{100\%}$	0.676		0.442
Average electrolyte concentration, c_e [mol cm^{-3}]	$1.2\text{x}10^{-3}$	$1.2\text{x}10^{-3}$	$1.2\text{x}10^{-3}$
Kinetic & Transport Properties			
Exchange current density, i_o [A cm^{-2}]	$3.6\text{x}10^{-3}$		$2.6\text{x}10^{-3}$
Charge-transfer coefficients, α_a, α_c	0.5, 0.5		0.5, 0.5
SEI layer film resistance, R_{SEI} [Ω cm^2]	0		0
Solid phase Li diffusion coefficient, D_s [cm^2 s^{-1}]	$2.0\text{x}10^{-12}$		$3.7\text{x}10^{-12}$
Solid phase conductivity, σ [S cm^{-1}]	1.0		0.1
Electrolyte phase Li$^+$ diffusion coefficient, D_e [cm^2 s^{-1}]	$2.6\text{x}10^{-6}$	$2.6\text{x}10^{-6}$	$2.6\text{x}10^{-6}$
Bruggeman porosity exponent, p	1.5	1.5	1.5
Electrolyte phase ionic conductivity, κ [S cm^{-1}]	$\kappa = 15.8 c_e \exp(0.85(1000 c_e)^{1.4})$		
Electrolyte activity coefficient, $f_\pm$	1.0	1.0	1.0
Li$^+$ transference number, t_+^o	0.363	0.363	0.363

Parameter	Value
Negative electrode equilibrium potential, U_- [V]	$U_-(x) = 8.00229 + 5.0647x - 12.578x^{1/2} - 8.6322 \times 10^{-4} x^{-1} + 2.1765 \times 10^{-5} x^{3/2} - 0.46016 \exp[15.0(0.06 - x)] - 0.55364 \exp[-2.4326(x - 0.92)]$
Positive electrode equilibrium potential, U_+ [V]	$U_+(y) = 85.681y^6 - 357.70y^5 + 613.89y^4 - 555.65y^3 + 281.06y^2 - 76.648y - 0.30987 \exp(5.657 y^{115.0}) + 13.1983$
Electrode plate area, A [cm^2]	10452
Current collector contact resistance, R_f [Ω cm^2]	20

Table 3.1. Electrochemical model parameters for 6 Ah Li-Ion HEV cell.

Dimensionless surface concentration		1% error bounds
$\bar{c}_{s,e} \big/ \bar{j}^{Li} = -1.139\sqrt{\tau}$	(3.18)	$0 < \tau < 1\text{x}10^{-4}$
$\bar{c}_{s,e} \big/ \bar{j}^{Li} = -1.122\sqrt{\tau} - 1.25\tau$	(3.19)	$0 < \tau < 8\text{x}10^{-2}$
Dimensionless 99% penetration depth		**1% error bounds**
$\bar{\ell} = 3.24\sqrt{\tau}$	(3.20)	$0 < \tau < 1\text{x}10^{-3}$
$\bar{\ell} = 3.23\sqrt{\tau} + 1.89\tau$	(3.21)	$0 < \tau < 2\text{x}10^{-2}$

Table 3.2. Empirical formulae fit to solid state diffusion PDE exact solution, Eq. (3.7).

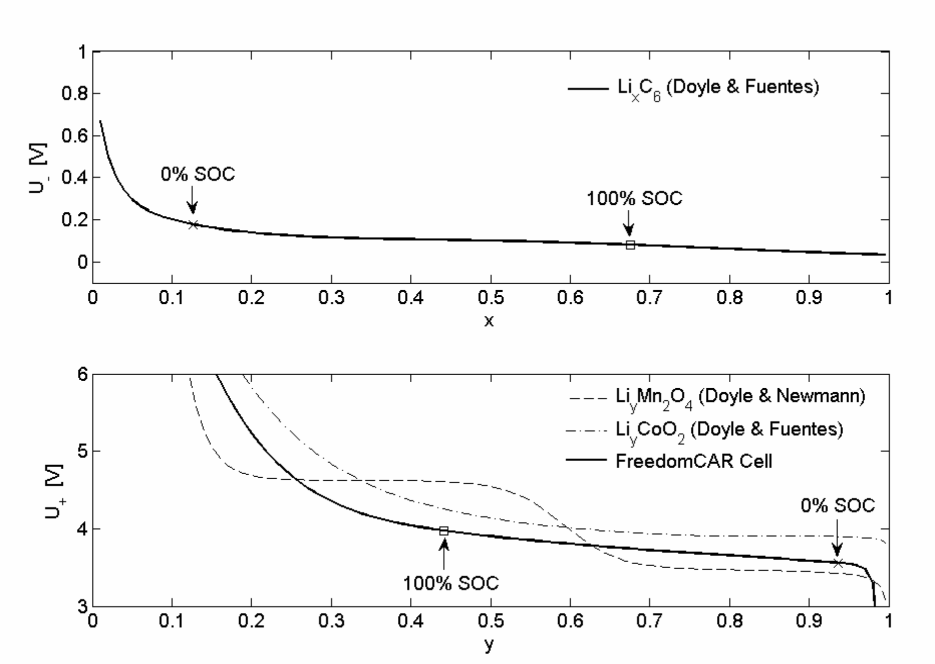

Figure 3.1. Empirical open-circuit, or equilibrium potential relationships for negative and positive electrodes.

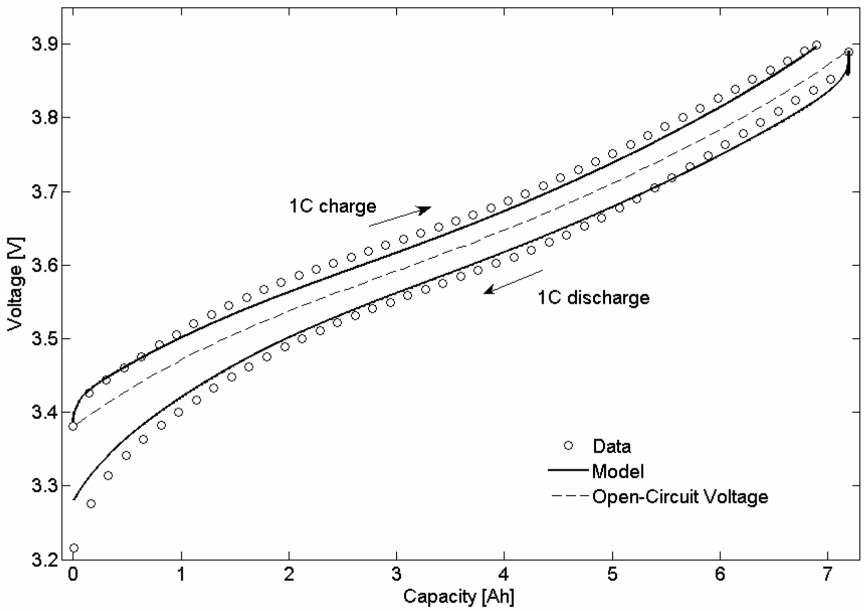

Figure 3.2. CFD model validation versus constant current charge/discharge data at 1C (6 Amp) rate.

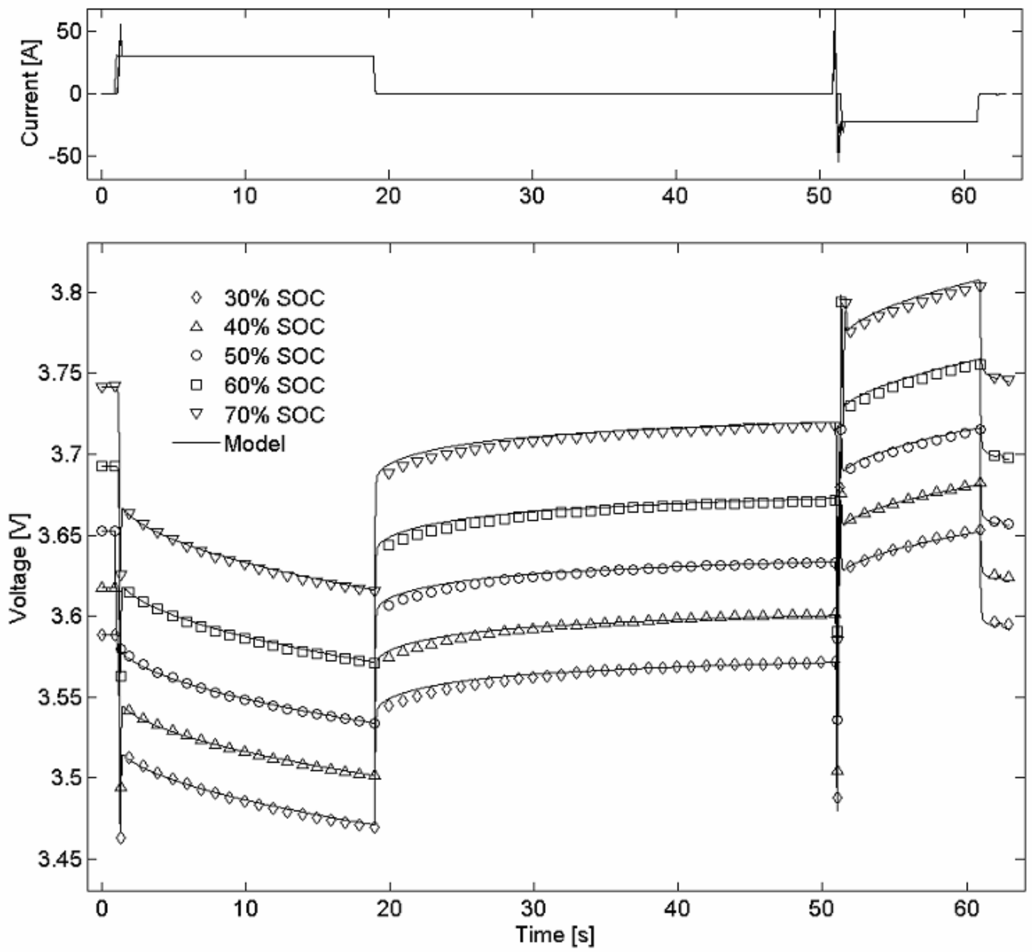

Figure 3.3. CFD model validation versus HPPC test data. SOC labeled on 6Ah-basis per FreedomCAR test procedures. SOC initial conditions used in 7.2 Ah-basis CFD model are 41.7%, 50.0%, 58.3%, 66.6%, and 75.0%.

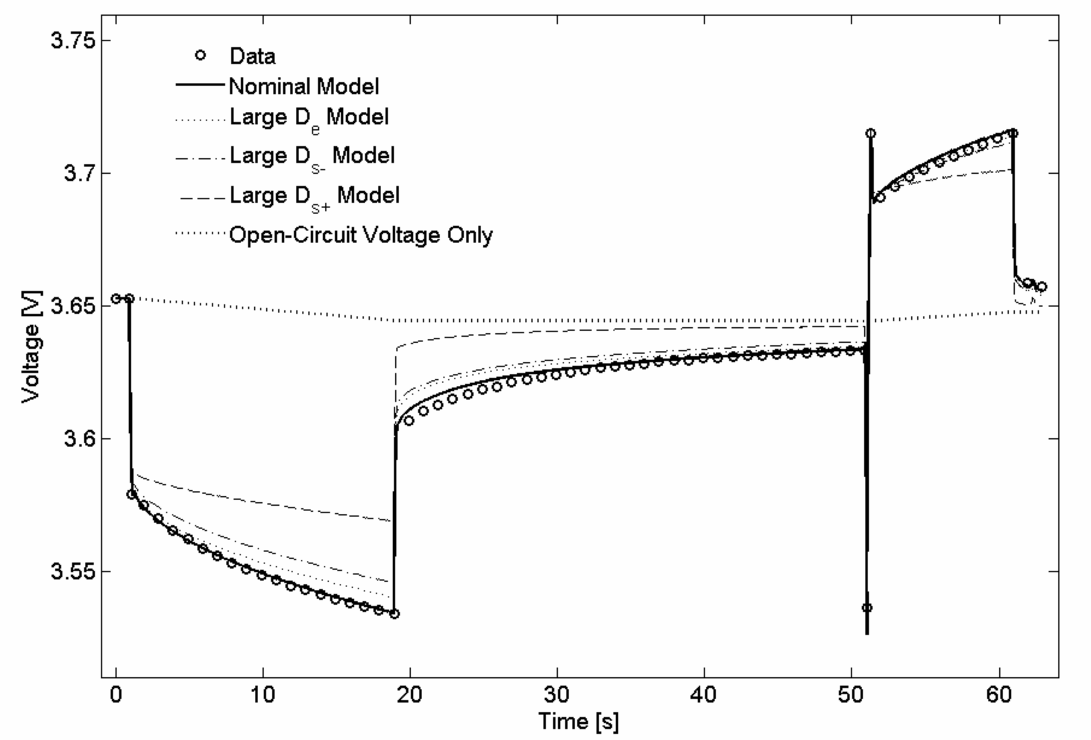

Figure 3.4. Nominal CFD model compared to models where limitations of electrolyte phase, negative electrode solid phase, and positive electrode solid phase diffusion have been individually (not sequentially) removed.

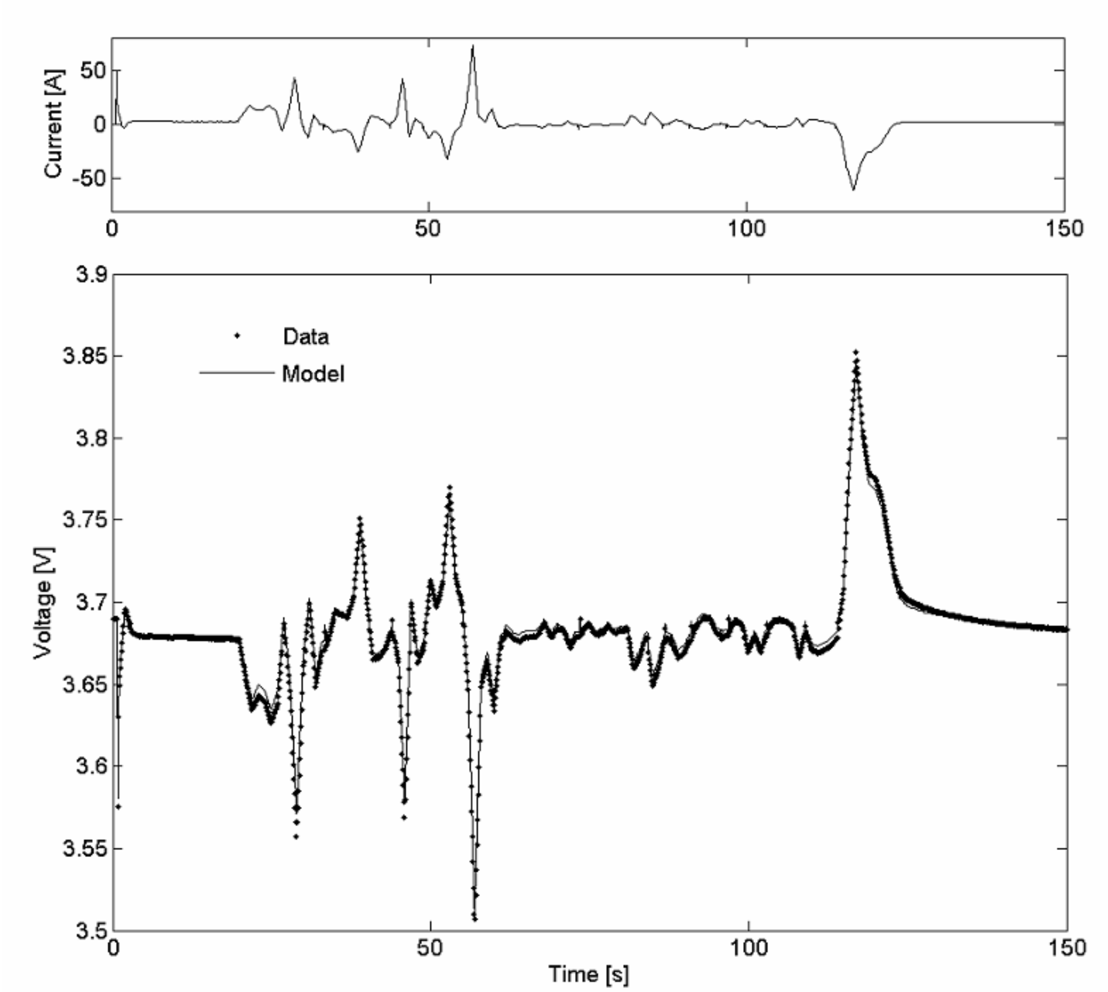

Figure 3.5. CFD model validation versus transient FUDS cycle HEV data. Power profile of data mimics that recorded from a Toyota Prius (passenger car) HEV run on a chassis dynamometer.

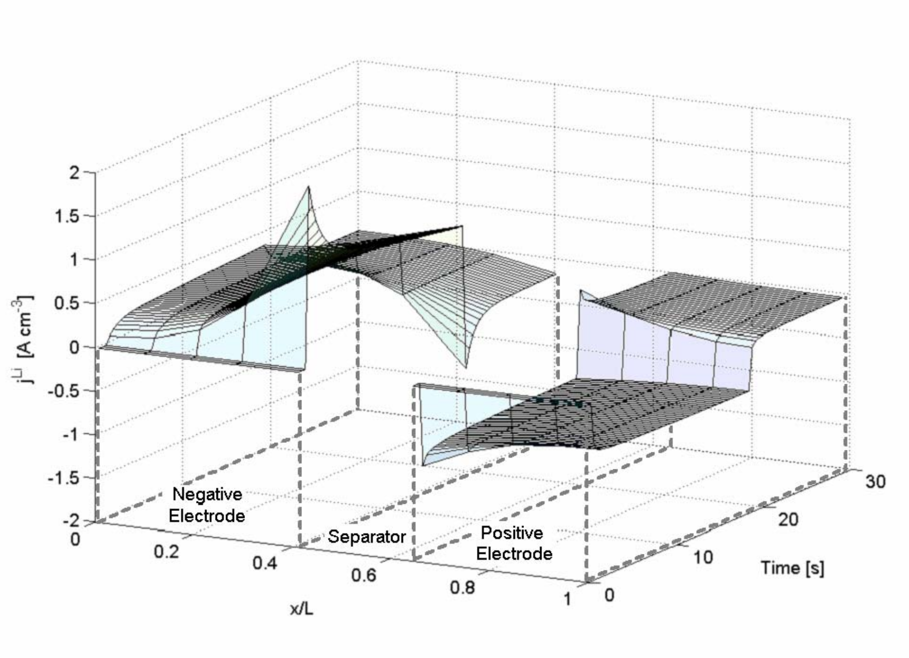

Figure 3.6. Distribution of reaction current across cell for first 30 seconds of HPPC test at 58.3% SOC.

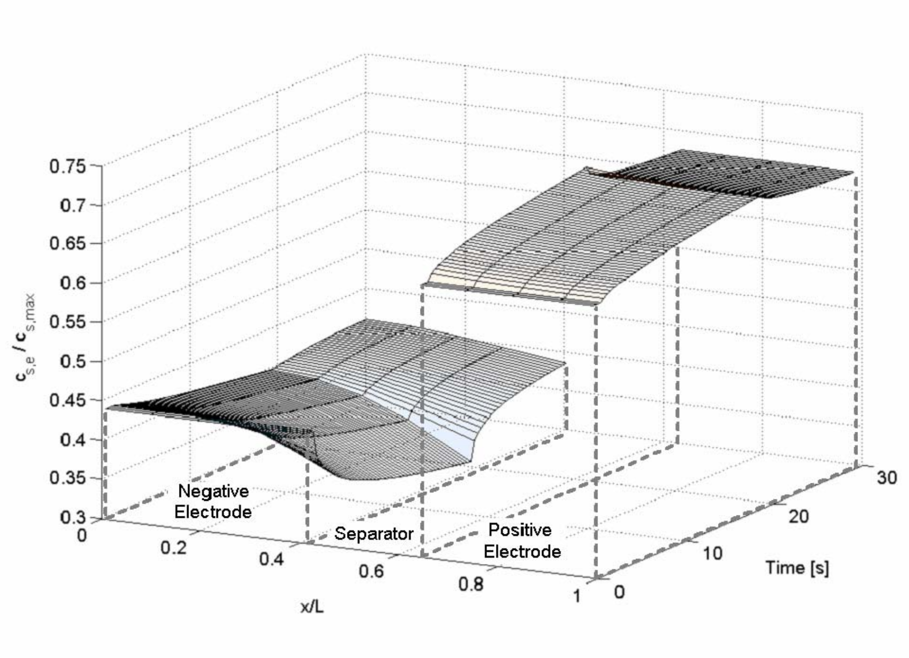

Figure 3.7. Distribution of active material surface concentration across cell for first 30 seconds of HPPC test at 58.3% SOC.

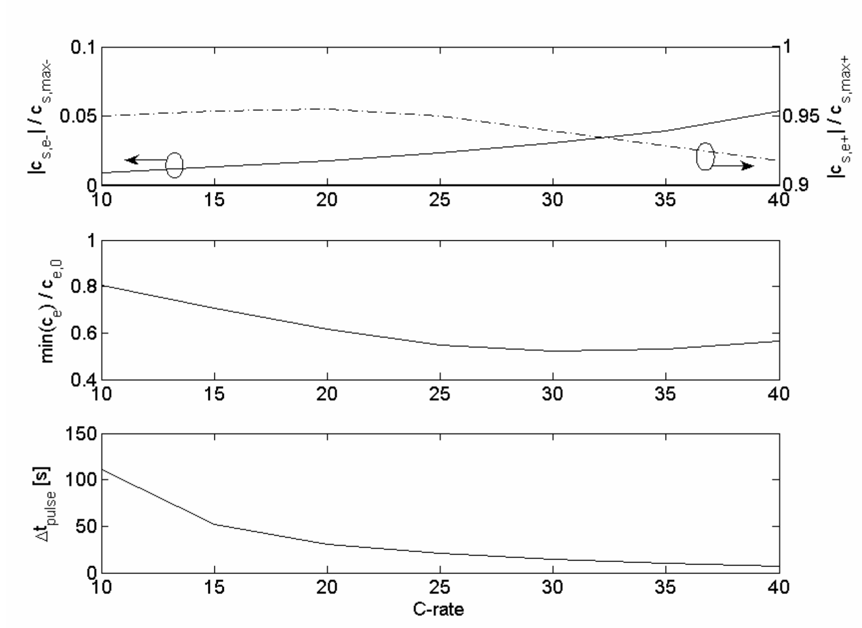

Figure 3.8. Solid phase surface concentration (top), minimum electrolyte concentration (middle), and time (bottom) at end of constant current discharge from 50% SOC for rates from 10C to 40C. Each discharge case ended at 2.7 V minimum limit.

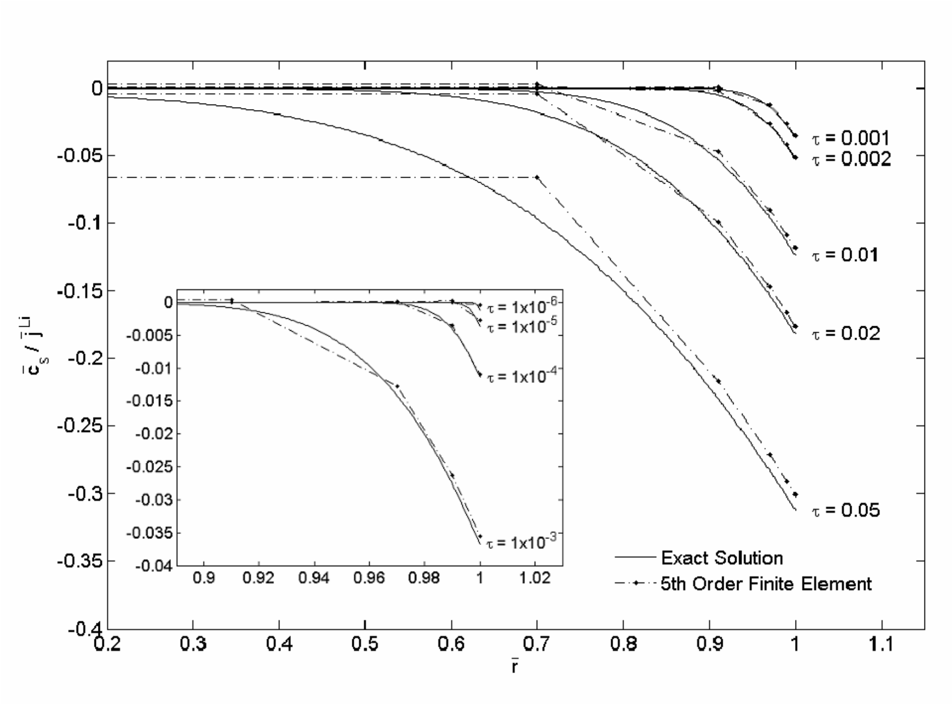

Figure 3.9. Dimensionless concentration distribution within an active material particle at various times during constant reaction current (dis)charge.

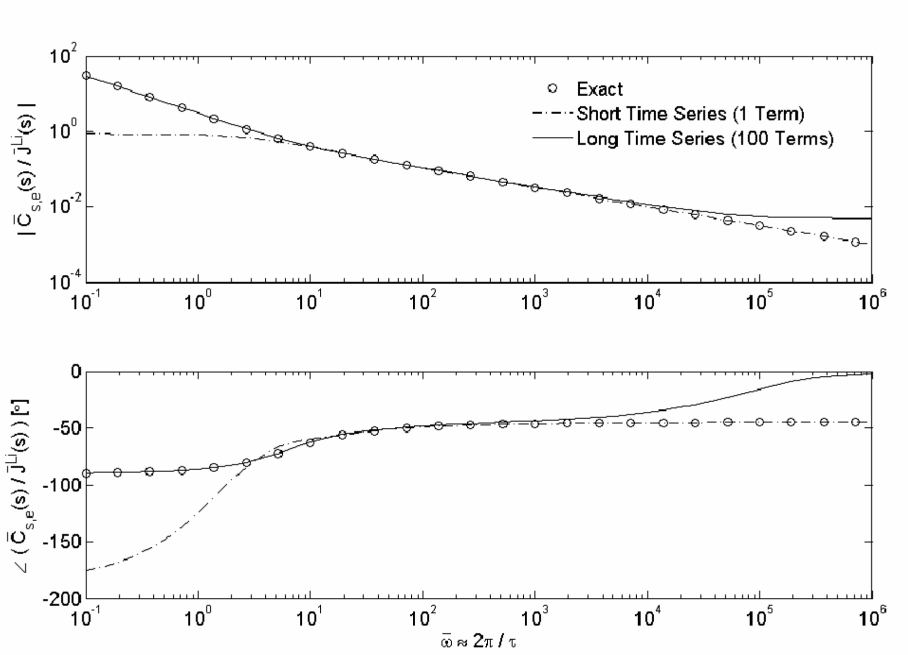

Figure 3.10. Frequency response of short and long time analytical solutions used in Ref. [2] for solid state diffusion in spherical particles, compared to exact frequency response.

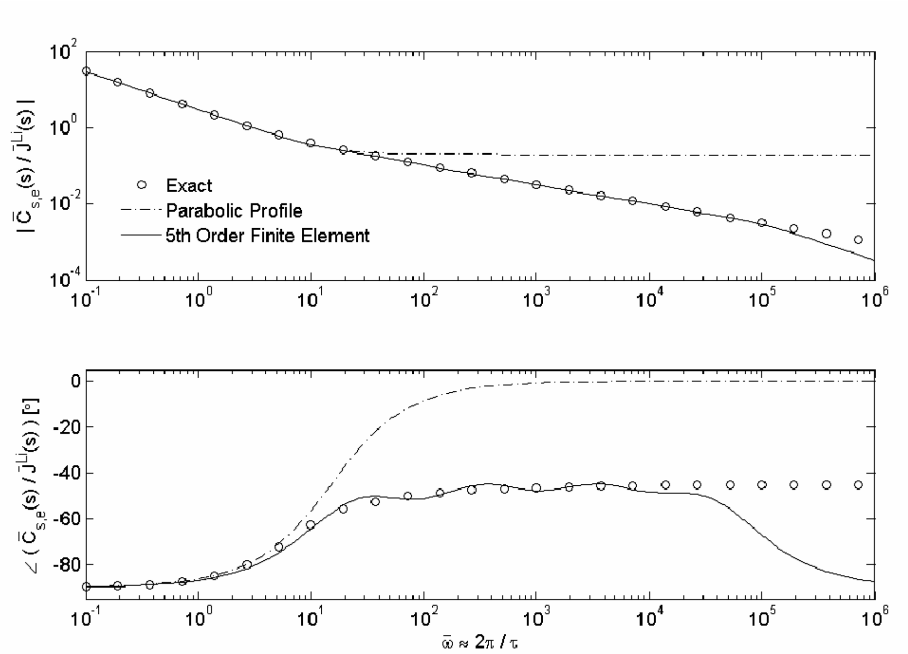

Figure 3.11. Frequency response of parabolic profile solid state diffusion submodel from Ref. [53] and fifth order finite element solid state diffusion submodel (used in this work), compared to exact frequency response.

Chapter 4 – POWER AND THERMAL CHARACTERIZATION[*]

The CFD model described in Chapter 2 and validated in Chapter 3 is used to predict performance of the 6 Ah Li-ion HEV battery relative to DOE Partnership for Next Generation Vehicles (PNGV) energy storage program goals. The 3.9 V maximum limit, meant to protect the negative electrode from the lithium plating side reaction, is found to be overly conservative for high rate (> 15C) pulses initiated from states of charge (SOCs) less than 100%. The CFD battery model is integrated into a DOE hybrid vehicle simulator to predict worst-case heat generation rates expected under in-vehicle operation.

4.1 Pulse Current Limits

HEV batteries transiently source and sink power in short pulses within a narrow SOC operating range, never using their entire available stored energy. PNGV test procedures [48] rate pulse power in terms of maximum current available for a given pulse length from a given SOC initial condition. The pulse length is chosen to be characteristic of typical vehicle acceleration (discharge) and deceleration (charge) events, in this case 18 seconds and 2 seconds respectively. To avoid complication of voltage-current interaction and ensure test repeatability, PNGV test procedures measure pulse power using constant current rather than constant power tests. End of discharge/charge is declared when the cell terminal voltage reaches predefined limits, in this case 2.7 V on discharge and 3.9 V on charge.

The bottom portion of Fig. 4.1 presents the simulated voltage response of 18 second maximum current discharge events initiated from various SOC initial conditions. For each event, successive simulations were run iteratively to find the discharge current rate whereby cell voltage hits the manufacturer's 2.7 V minimum limit at exactly 18 seconds. All simulations are begun from the rest state. A constant discharge current is applied at simulation time *t* = 0 and, due to ohmic limitations, the cell voltage response immediately departs from open circuit potential. Similarly, the top portion of Fig. 4.1 displays the voltage

---

[*] This chapter adapted from: K.A. Smith, C.-Y. Wang, "Power and Thermal Characterization of a lithium-ion battery pack for hybrid-electric vehicles," *J. Power Sources*, 160 (2006) 662-673.

response of 2 second maximum charge current events with a 3.9 V cutoff criteria initiated from various SOC initial conditions.

The cell is only mildly limited by electrolyte phase diffusive transport. Figure 4.1 shows each constant current simulation run again with the electrolyte diffusion coefficient, D_e, raised 5 orders of magnitude to artificially remove electrolyte phase diffusion limitations. Electrolyte diffusion effects are apparent in cell voltage response only at very high levels of current (> 150 A, or 25C rate) sustained for longer than ~5 seconds. These sustained high rate current events give rise to large electrolyte concentration gradients that polarize voltage response.

Figure 4.2 shows distribution of reaction current at various times during the 160 A discharge from 50% SOC, both with and without electrolyte diffusion limitations in the model. The two cases are almost identical, indicating that the coupling between electrochemical reaction and electrolyte concentration (2^{nd} term in Eq. 2.9) is negligible for operating conditions sufficiently far from electrolyte depletion. This observation enables an analytical solution for reaction distribution, employed later in Chapter 6.

Figure 4.3 shows active material (solid phase) bulk and surface concentrations at various times during the 160 A discharge from 50% SOC. End of discharge is caused by depleted/saturated negative/positive electrode surface concentrations. Bulk concentrations change much less than surface concentrations during the discharge. Given time for concentration gradients to relax following the discharge event, further discharge will be possible. In general, the manufacturer's 2.7 V cutoff is a good indicator of depleted/saturated surface concentrations for pulses longer than 10 s. For very short duration, high-rate current pulses, however the minimum voltage limit can be overly conservative given the large ohmic voltage perturbation.

During cell charging, current rate capability is limited due to the proximity of the cell's open circuit voltage (3.6 V at 50% SOC) to the manufacturer's maximum voltage limit (3.9 V). At 100% SOC, the negative and positive electrode stoichiometries ($x_{100\%} = 0.676$ and $y_{100\%} = 0.442$) are far from respective saturation and depletion and further charge is physically possible beyond the 100% SOC reference point.

Raising the upper voltage limit would increase both charge power rate capability and overall capacity [57], though it may introduce side reactions detrimental to the pack's future rate capability. Lithium plating on the surface of negative electrode Li_xC_6 active material particles is the most common side reaction attributed to capacity and power fade [7,58,59]. Arora et. al. [58] showed that designing a cell with sufficient excess negative electrode and limiting the maximum allowable voltage during charge are successful strategies for avoiding the plating reaction. The plating reaction becomes thermodynamically favorable when the difference between solid and electrolyte phase potentials becomes zero or

$$\phi_s - \phi_e = 0 . \tag{4.1}$$

We check this condition at the end of 2 second charge pulses initiated from various SOC initial conditions and, though the phase potential difference does become progressively smaller approaching 100% SOC, it never reaches zero. The smallest value observed is 80.2 mV, occurring at the negative electrode/separator interface at the end of the 2 second charge from 100% SOC. By comparison, the smallest value observed at the end of the 2 second charge from 50% SOC is 90.4 mV. Both of these charge cases terminate at the 3.9 V cutoff, though clearly the 50% SOC case leaves more margin with respect to the lithium plating condition. A substantial portion of the voltage rise from 50% SOC is ohmic due to the large –101 A charging rate and the cell terminal voltage reaches the 3.9 V limit well before risk of lithium plating.

Figure 4.4 shows the evolution of $\phi_s - \phi_e$ distribution across the negative electrode for the 2 second charge cases from 50% and 100% SOC, both ending at the manufacturer specified 3.9 V upper voltage limit. In these and all other charge cases, the minimum value of $\phi_s - \phi_e$ occurs at the separator interface, also noted in [58]. Increasing the charging rate from the 50% SOC initial condition, we find that the cell can sustain a –155 A charge for 2 seconds and still maintain the same degree of conservatism with respect to lithium plating as the 100% SOC case ($\phi_s - \phi_e \geq 80.2 \text{ mV}$).

4.2 PNGV Power Capability

PNGV test procedures estimate power capability using constant current rather than constant power tests. Maximum discharge/charge power is calculated by multiplying maximum current by final voltage at the end of the pulse event (i.e. the minimum/maximum voltage limit). Compared to a constant power test method, the constant current method will slightly underpredict maximum discharge power and overpredict maximum charge power.

The PNGV HPPC experimental test procedure applies a step change in current (~5C) from a known SOC rest condition and uses the measured voltage perturbation to calculate polarization resistances representative of 18 second discharge and 2 second charge. The test is repeated at roughly 10% intervals in SOC. Maximum discharge and charge currents are then estimated using the formulae

$$\begin{aligned} I_{discharge} &= (OCV - V_{\min}) / R_{discharge} \\ I_{charge} &= (V_{\max} - OCV) / R_{charge} \end{aligned} \tag{4.2}$$

where $R_{discharge}$, R_{charge}, and OCV (open circuit voltage) are experimentally-determined functions of SOC while V_{min} and V_{max} are constant values specified by the manufacturer. The present approach differs only in that we use the 1-D electrochemical model to predict maximum current versus SOC rather than linearly extrapolate low rate experimental data. Note that the PNGV linear extrapolation procedure will only be accurate within linear regions of operation where equilibrium potentials and kinetics exhibit linear behavior, properties remain constant, etc. High rate, 30-40C simulation results presented earlier, however, exhibited strong non-linearities as active material surface concentrations approached depletion/saturation at end of discharge. We therefore expect the nonlinear 1-D electrochemical model to produce more accurate results.

4.2.1 Room Temperature

Figure 4.5 presents the maximum 18 second discharge and 2 second charge power rate capability of the 72 cell battery pack at 25 ˚C predicted by the electrochemical model. Much of the same information can be found in Fig. 4.1, though Fig. 4.5 now displays power rate capability (rather than current rate capability) found by multiplying maximum 18 second discharge current by V_{min} = 194.4 V and maximum 2 second charge current by V_{max} = 280.8 V. The maximum power rates are displayed with respect to the 25 kW discharge (left axis) and 30 kW charge (right axis) PNGV power assist goals. Above 77% SOC, the 18 second discharge power is limited by a 217 A maximum current limit established by PNGV requirements. Left and right axes of Fig. 4.5 are plotted on different scales such that the PNGV power assist goals for discharge and charge align horizontally. The battery pack can only meet the two goals simultaneously at SOCs ranging from 36.2% to 46.2% SOC. Within this narrow operating range, the battery pack can source and sink ~190 Wh of energy at a 1C rate, short of the PNGV available energy goal of 300 Wh.

Shown in Fig. 4.5, the SOC operating range may be significantly expanded if, rather than imposing a constant 280.8 V maximum voltage limit, higher rates of charge current are allowed up to a lithium plating side reaction limit of $\phi_s - \phi_e \geq 80.2 \text{ mV}$. Only for the 100% SOC case does the constant current lithium plating-limited charge terminate at a pack voltage of 280.8 V (3.9 V/cell). Charge cases initiated from lower SOCs terminate at modestly elevated voltages, up to a maximum of 296.7 V (4.12 V/cell) for the 2 second charge case from 27% SOC. Below 27% SOC, charge performance is limited by the -217 A PNGV maximum current requirement. To permit equal judgement of the nominal (3.9 V/cell limited) and expanded ($\phi_s - \phi_e \geq 80.2 \text{ mV}$ limited) charge current capability, lithium plating-limited charge powers are calculated using the same end of charge voltage, 280.8 V.

With lithium plating-limited 2 second charge, PNGV power assist goals are now met within a 36.2% to 67.5% SOC range. Available energy at the 1C rate increases from ~190 Wh to ~595 Wh, a 212% improvement. Taking the intersection of the discharge and charge curves on Fig. 4.5 as the maximum discharge and charge power simultaneously realizable from a given SOC, use of the lithium plating limit would increase power rate capability of the battery pack by 22% over the nominal case. The potential for increased performance motivates the model-based estimation and constraint management approach presented in Chapter 7.

4.2.2 Temperature Dependence

We next define operating maps of 18 second discharge and 2 second charge power capability as a function of SOC initial condition and cell temperature. Electrochemical model properties are made temperature dependent through Arrhenius expressions, Eq. (2.16). Activation energies, defined in Table 4.1, are estimated from the data used by Botte et al. [19]. Each case is run under isothermal operating conditions.

Figure 4.6 shows the 18 second discharge power capability of the PNGV battery pack throughout a range of temperatures (–15 to 65˚C) and SOCs (0 to 100%). The contour plot is generated by running the model at 11 different SOCs for each of 5 different temperatures. Figure 4.6 data presented at 25˚C is identical to that from Fig. 4.5. A map of 2 second charge power (280.8 V limited) throughout the temperature/SOC operating range is shown in Fig. 4.7. As operating temperature is reduced, slow kinetics require increased overpotential, η, to drive reaction, sluggish diffusion properties result in increased solid and electrolyte phase concentration gradients, $\partial c_s / \partial r$ and $\partial c_e / \partial x$, and decreased ionic conductivity of the electrolyte leads to larger electrolyte phase potential gradients, $\partial \phi_e / \partial x$. All effects result in a greater voltage polarization from the equilibrium open-circuit voltage for a given current pulse. As we reduce operating temperature below the nominal 25˚C the range of SOC meeting the PNGV discharge and charge goals narrows until, for temperatures of 16˚C and below, the dual goals can no longer be simultaneously met.

4.3 In-Vehicle Heat Generation

We adapt the CFD model to be called as an energy storage subsystem model from the PSAT vehicle simulator (developed by DOE/Argonne National Labs) running in the Matlab/Simulink environment. At each 100th of a second time step, the FORTRAN battery model subroutine calculates pack voltage, SOC, temperature, heat generated, etc. as a function of current applied by the vehicle's electric drivetrain. Figure 4.8 shows vehicle speed profiles for the FUDS, HWFET, and US06 driving cycles used as inputs to the vehicle simulator.

To establish cooling requirements for the PNGV Li-ion battery pack we use the integrated battery model/vehicle simulation tool to predict battery pack heat generation rate under constant temperature operation in a small 5 seat passenger car similar to a Toyota Prius. The PNGV Li-ion battery pack shares similar power and energy ratings with the Ni-

MH pack used by the Prius, but weighs less and occupies less volume. Vehicle and drivetrain-specific parameters of the power-split HEV are summarized in Table 4.2.

Figure 4.9 presents time-averaged heat generation rate and turnaround efficiency of the PNGV Li ion battery pack under isothermal operation at 6 different cell temperatures (ranging from -15˚C to 85˚C) for each of the three different driving cycles. Across the range of simulated temperatures, the HWFET cycle (with relatively few acceleration events and moderate highway speeds) generates the least heat while the FUDS cycle (with numerous short acceleration events at low speeds) generates roughly twice that amount. The US06 cycle (with long acceleration events to high speeds and continued acceleration/deceleration events while at speed) generates four to six times that of the FUDS cycle. The 320W average heat generation rate for the US06 cycle at 25˚C is larger than, but similar in magnitude to the 250W worst-case heat generation rate predicted by Nelson et. al. [21] on their modified HWFET cycle.

Across the -15˚C to 85˚C simulated temperature range, the profile of power cycled to and from the battery pack is virtually identical for a given driving cycle. Heat generation rates in Fig. 4.9 depend on operating temperature, however, due to the increased voltage perturbation caused by sluggish kinetics and transport properties at low temperatures. With the exception of reversible heating (not considered in this work as discussed in Chapter 2), all modes of heat generation dissipate and waste potentially useful energy. Battery round-trip energy efficiencies follow the opposite trend of heat generation rates, with the lowest efficiency (87%) seen on the coldest (-15˚C) US06 cycle. Round-trip efficiency generally surpasses the PNGV goal of 90%.

To explain the driving cycle dependency of heat generation rates, Figs. 4.10 and 4.11 present detailed plots of the FUDS and US06 cycles, respectively, under isothermal operation at 25˚C. Each figure shows power cycled to and from the battery pack, battery pack SOC, and cumulative amount of heat generated by the battery pack (i.e. the time integral of the instantaneous heat generation rate).

The US06 case (Fig. 4.11) cycles the battery pack about a wider range of SOC than the FUDS case (Fig. 4.10). In total, 1827 kJ of energy is discharged over the course of the

1372 second FUDS cycle, and 1822 kJ of energy is charged. By comparison, during the 600 second US06 cycle, 2235 kJ of energy is discharged, and 2263 kJ of energy is charged. Expressing the total amount of charge and discharge energy on a per-second basis to correct for the different durations of the two cycles, the US06 cycle sources and sinks roughly 2.8 times the energy of the FUDS cycle. But from Fig. 4.9, we see that at 25˚C the US06 cycle generates heat at a rate 5.9 times that of the FUDS cycle. Heat generation is much more strongly current (or power) rate-dependent than energy-dependent due to the ohmic heating mechanisms of Eqs. (2.19) and (2.20).

The bottom portions of Figs. 4.10 and 4.11 show individual components of heat generation in the PNGV pack. In both cases, contact resistance contributes the most to heat generation (Eq. (2.20), followed by electrolyte-phase conductivity (2nd and 3rd terms of Eq. (2.19)), heating due to electrochemical reaction (Eqn. (2.18)), and lastly solid-phase conductivity (1st term of Eqn. (2.19)), negligible in all cases. Given the dominance of ohmic heat generation mechanisms, a lumped electrochemical model [21] or perhaps an equivalent circuit model should be sufficient to predict heat generation rates across a range of driving cycles. Such a model would need to be validated under several different temperatures and state-of-charge operating conditions, however.

We briefly consider the problem of cooling such a power-dense energy storage system onboard a HEV. PNGV energy storage system performance goals define a temperature range for equipment operation of –30 to +52˚C. At 52˚C, Fig. 4.9 predicts a 302W heat generation rate on the US06 cycle. With only the outer radial surface of each cylindrical cell exposed to the cooling medium, the total surface area, A_s, of the 72 cell pack is approximately 1.35 m^2. The cooling medium is most likely to be air drawn from the passenger cabin at perhaps 30˚C. Substituting each of these values into Eqn. (2.17) we find a convective heat transfer coefficient, h, of 10.1 W/m^2 K is required to maintain the battery pack at a constant 52˚C and prevent further temperature rise. A simple forced-convection cooling scheme with air as the cooling fluid could adequately meet [60] what we consider to be the worst-case requirement for steady-state operation. A more difficult problem, not explored here, would be to rapidly cool the battery pack from the maximum PNGV equipment survival goal of 66˚C back down to 52˚C at start-up.

4.4 Conclusions

The 1-D electrochemical, lumped thermal CFD model is used to explore limiting regions of pulse power operation for a 6 Ah, 72 cell, 276 V nominal Li ion battery pack designed for the PNGV program. Electrolyte phase Li^+ transport (diffusion and migration) is sufficiently fast to have little impact on high-rate power capability and transient voltage response. In contrast, solid phase Li transport (diffusion) significantly limits high rate performance and end of discharge at the 2.7 V/cell minimum limit is caused by depleted/saturated active material surface concentrations in the negative/positive electrodes for pulses lasting longer than around 10 seconds. During high rate discharge pulses, bulk solid concentrations (related to SOC) change very little and the inner regions of active material particles go unutilized.

The 3.9 V/cell maximum limit, meant to protect the negative electrode from side reactions such as lithium plating, is overly conservative for pulse charging initiated from SOCs less than 100%. By limiting charge via a $\phi_s - \phi_e$ potential margin, rather than a 3.9 V cell terminal voltage limit, charging rates are increased by approximately 50% and overall power density (defined using PNGV 18 second discharge and 2 second charge metrics) is increased by 22%.

Installed in a midsize passenger car, the battery pack is predicted to generate heat at a rate of 320 W on a US06 cycle at 25ºC, with more heat generated at lower temperatures. Heat generation rates on the less aggressive FUDS and HWFET cycles are substantially less. For pulse power operation typical of HEV applications, ohmic heating dominates other heating mechanisms and equivalent circuit models validated over a range of temperatures and SOCs should sufficiently predict heating rates for various driving cycles and control strategies. Maintaining cell temperature at or below the 52ºC PNGV operating limit on the worst-case US06 cycle requires a convective heat transfer coefficient of h = 10.1 $W/m^2 K$, realizable with forced air convection.

Activation Energy	Value [J/mol]
Exchange current densities: $E_{act}^{i_{0-}}, E_{act}^{i_{0+}}$	3 x 10^4, 3 x 10^4
Solid phase diffusion coeff.: $E_{act}^{D_{s-}}$, $E_{act}^{D_{s+}}$	4 x 10^3, 2 x 10^4
Electrolyte phase diffusion coeff.: $E_{act}^{D_e}$	1 x 10^4
Electrolyte phase conductivity: E_{act}^{κ}	2 x 10^4

Table 4.1. Activation energies used in Arrhenius equation (2.16) coupling physiochemical cell parameters to lumped thermal model

Parameter/Component	Value
Vehicle mass, m_{veh}	3040 kg
Frontal area, A_f	1.746 m^2
Coefficient of drag, C_D	0.29
1.5L gasoline engine	52.2 kW, 111 Nm peak
Electric motor 1	20 kW, 75 Nm peak
Electric motor 2	33 kW, 350 Nm peak
Battery pack	276 V nominal, 72 cell, 6 Ah Li-Ion

Table 4.2. Vehicle-specific parameters used for driving cycle simulations of Figs. 4.9-4.11

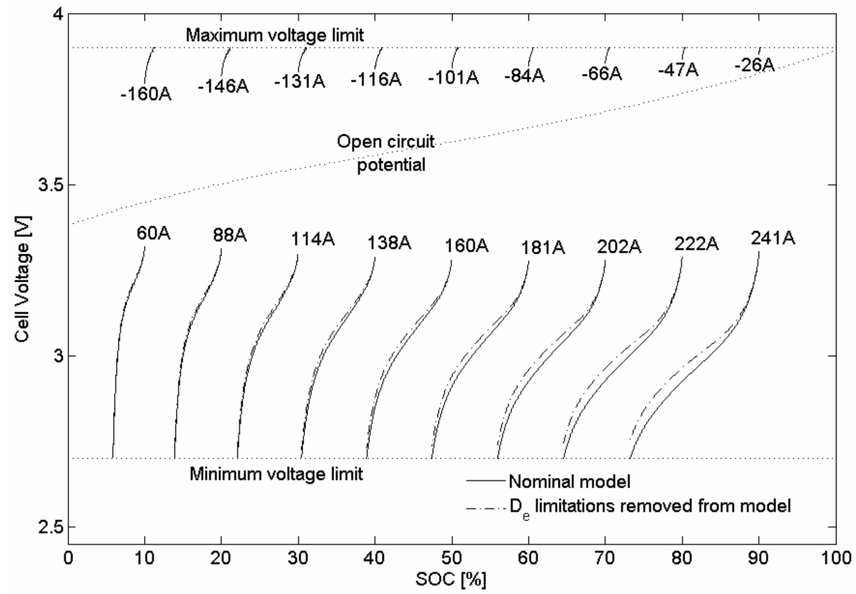

Figure 4.1. Voltage response for maximum 18 second pulse current discharge and 2 second pulse current charge events initiated from various SOC initial conditions. End of 18 second discharge and 2 second charge cases are defined at limits of 2.7 and 3.9 V/cell, respectively.

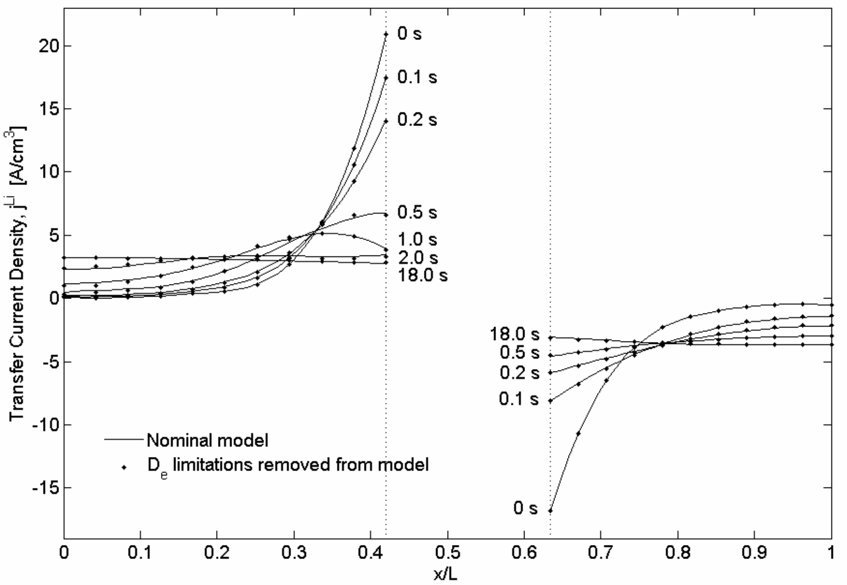

Figure 4.2. Distribution of reaction current at various times during the 160 A discharge from 50% SOC shown in Fig. 4.1.

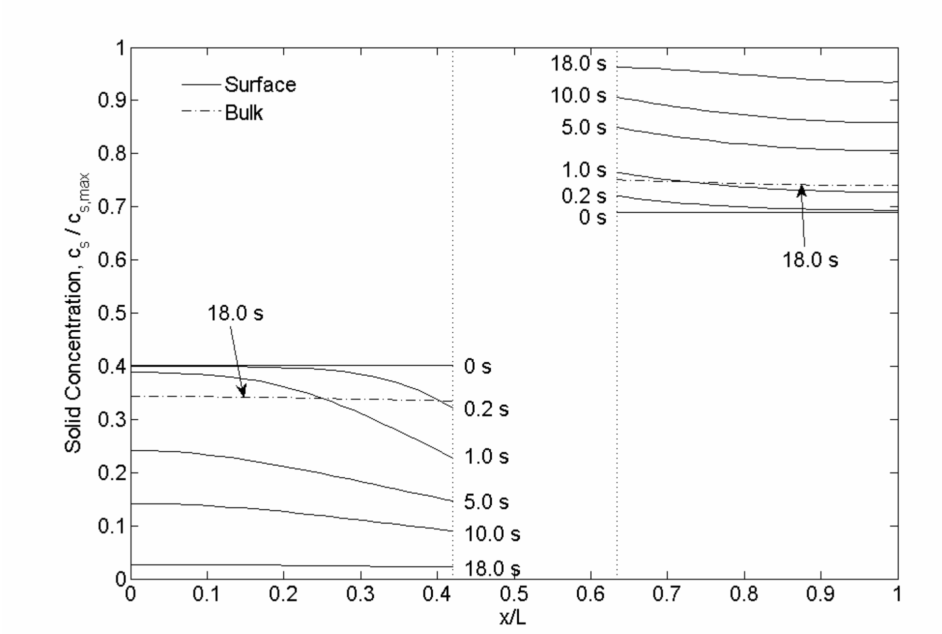

Figure 4.3. Active material (solid phase) bulk and surface Li concentrations at various times during the 160 A discharge from 50% SOC shown in Fig. 4.1.

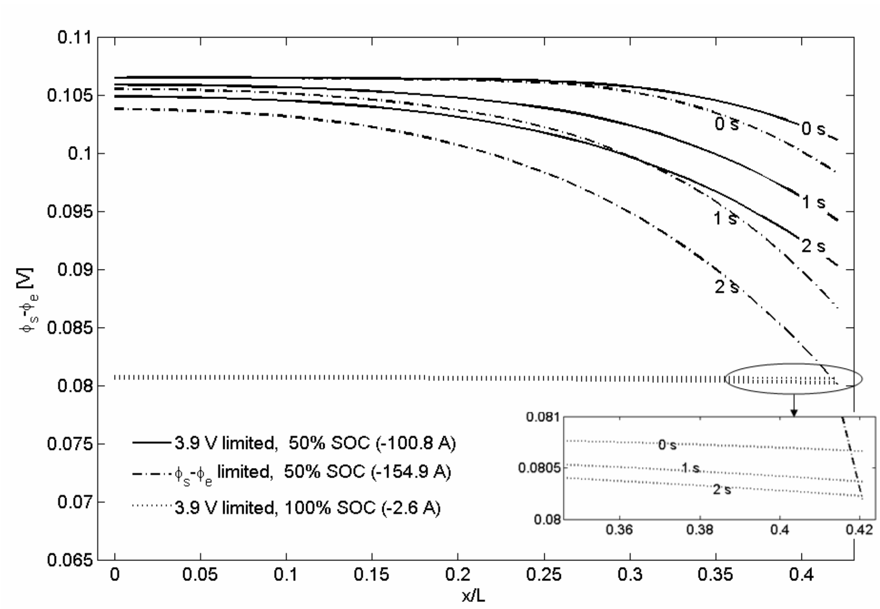

Figure 4.4. Difference between solid and electrolyte phase potentials in the negative electrode at various times during 2 second constant current charge cases initiated from various SOC initial conditions. The $\phi_s - \phi_e$ limited case provides the same margin with respect to damaging side reactions as the 3.9 V limit at 100% SOC.

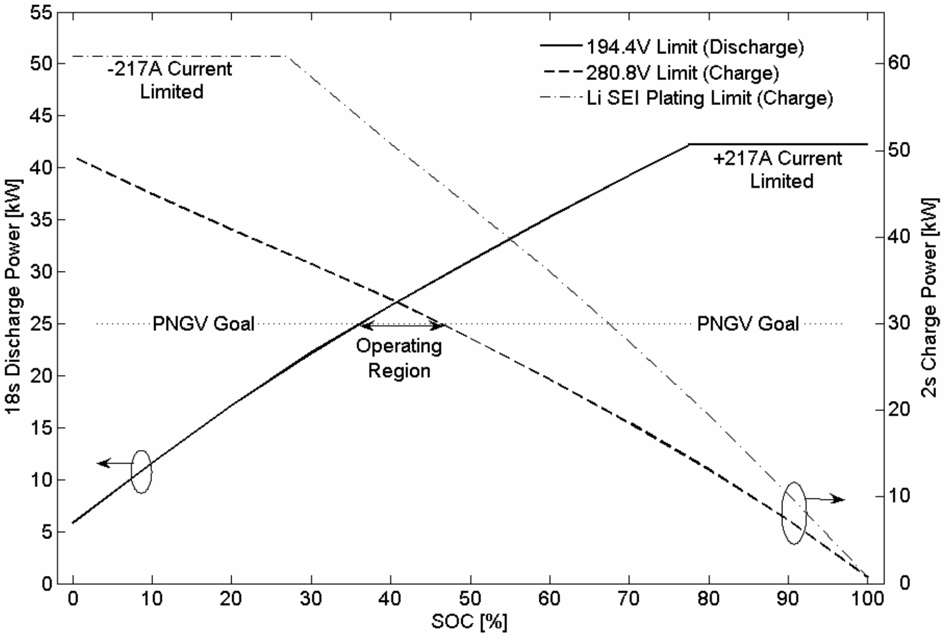

Figure 4.5. Power rate capability of the 72 cell pack at 25ºC compared to PNGV 18 second discharge and 2 second charge goals. Operating region could in theory be expanded by enforcing a Li plating limit rather than a constant 3.9 V/cell limit on charge.

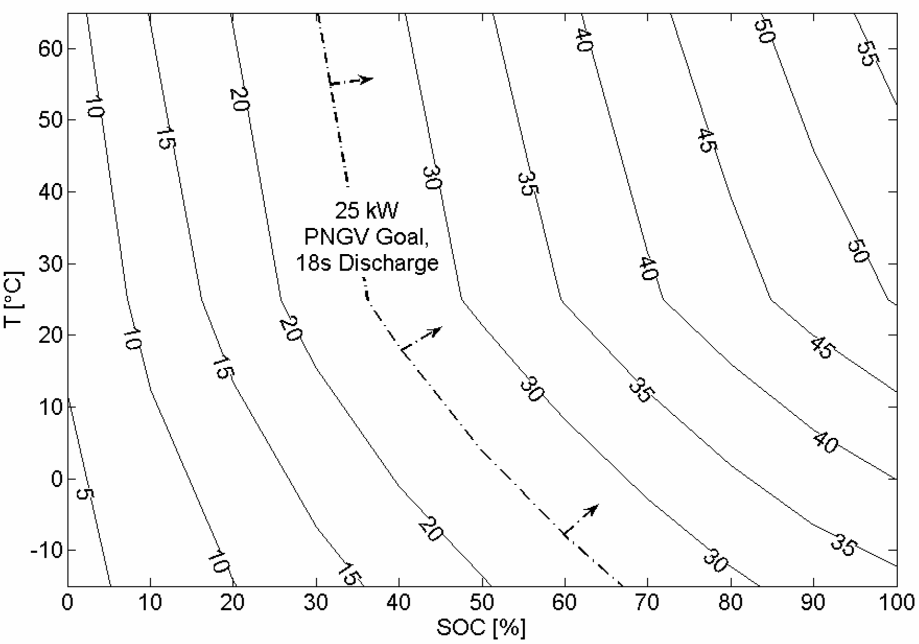

Figure 4.6. Contours of 18 second discharge power [kW] capability throughout SOC/ temperature operating range.

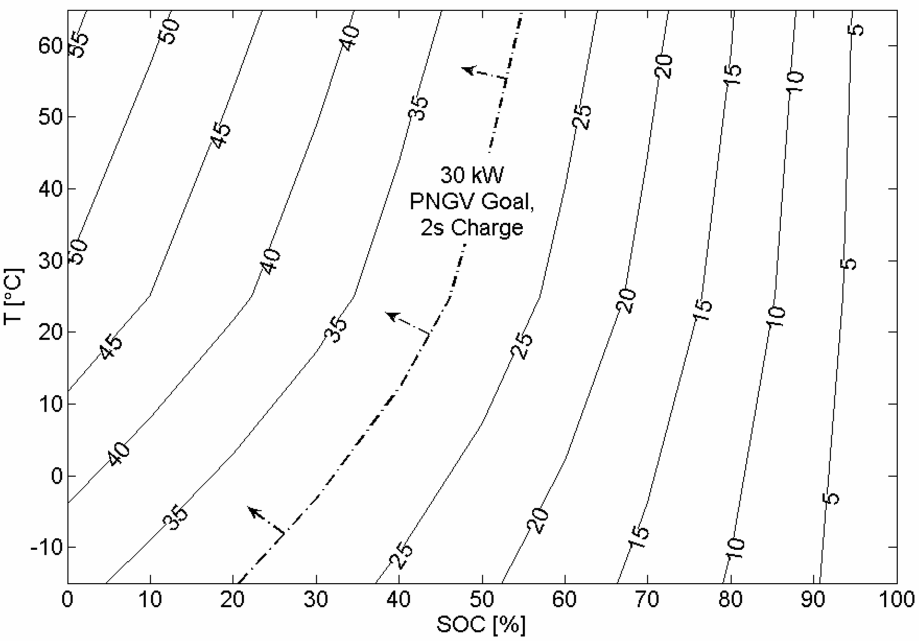

Figure 4.7. Contours of 2 second charge power [kW] capability throughout SOC/ temperature operating range.

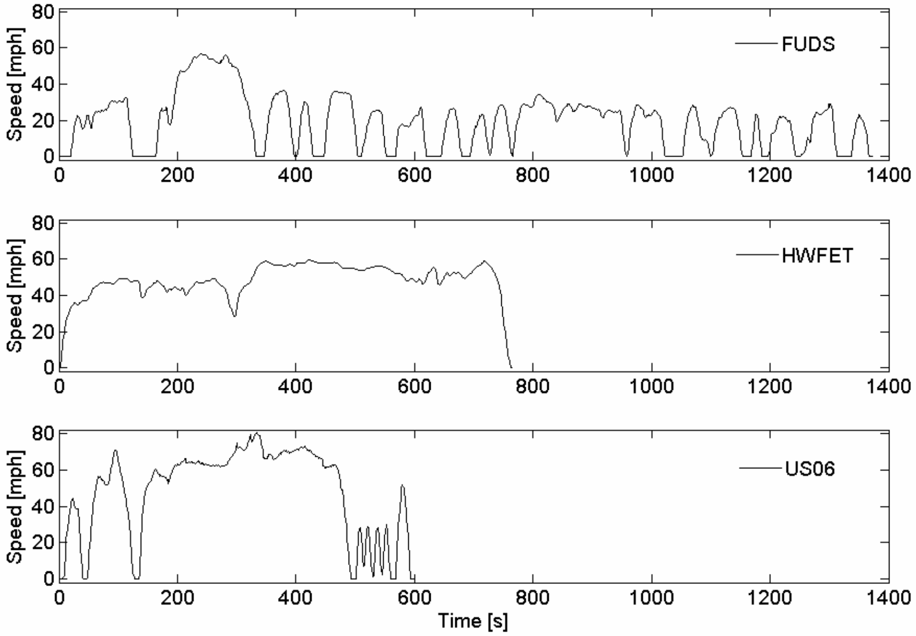

Figure 4.8. Vehicle speed profiles for FUDS, HWFET, and US06 driving cycles.

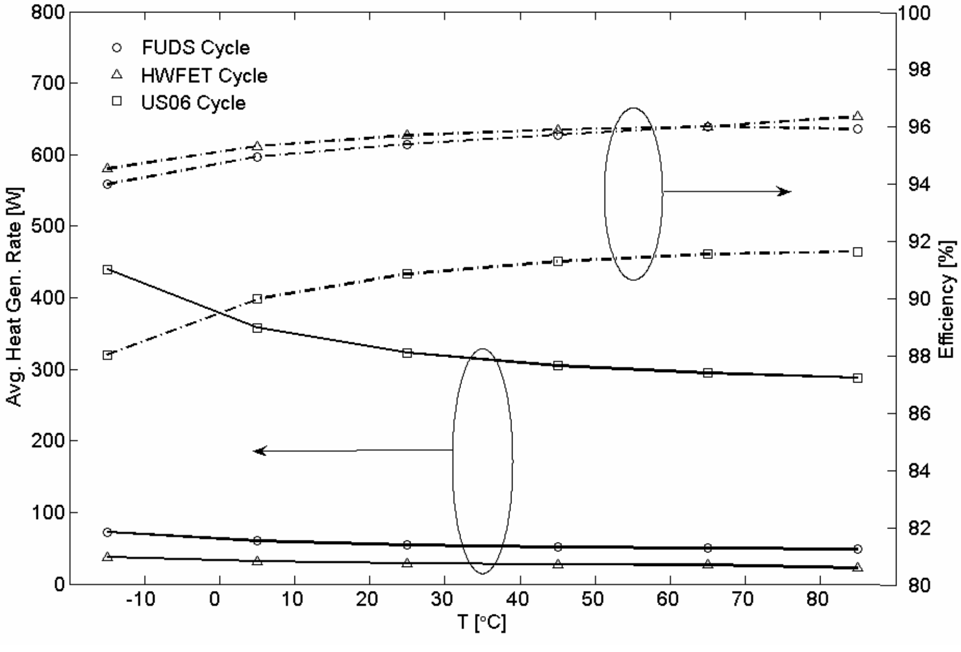

Figure 4.9. Average heat generation rate (solid lines, left axis) and efficiency (dashed lines, right axis) of PNGV battery pack integrated into a small HEV passenger car. Simulations were run at 6 different temperatures for each of 3 different driving cycles.

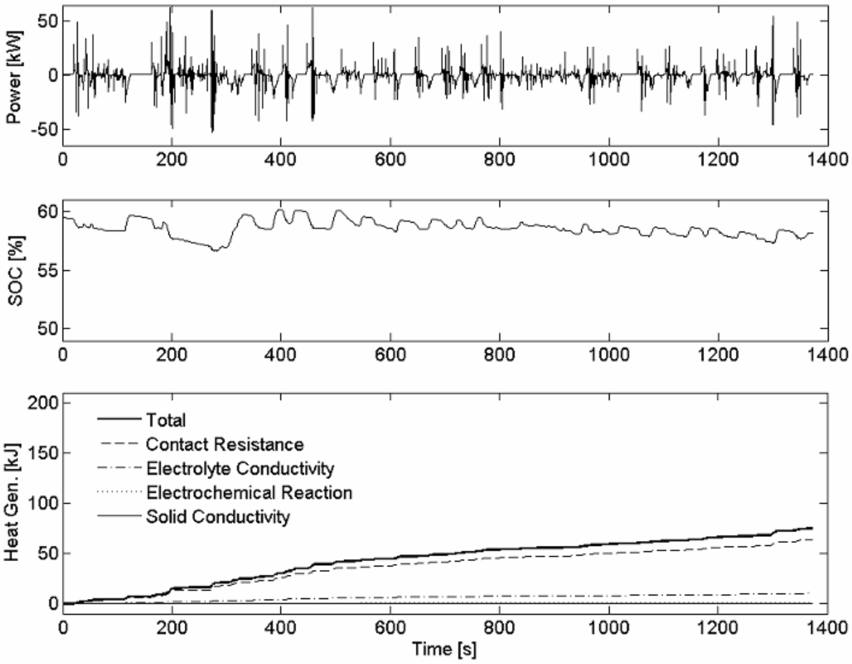

Figure 4.10. FUDS driving cycle results for the 25ºC isothermal battery pack. Individual components of the total heat generated are shown in the bottom-most plot.

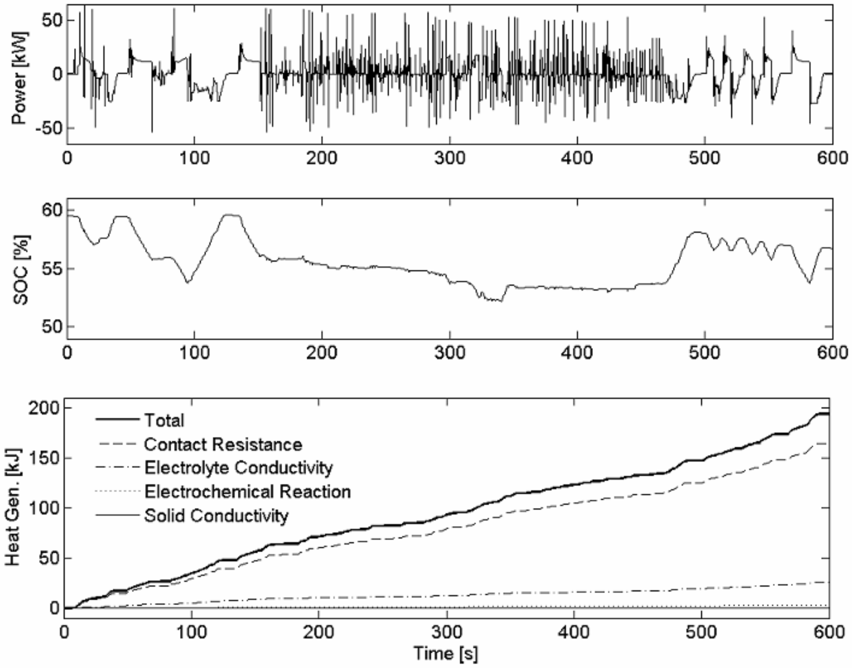

Figure 4.11. US06 driving cycle results for the 25ºC isothermal battery pack. Individual components of the total heat generated are shown in the bottom-most plot.

Chapter 5 – MODEL ORDER REDUCTION OF 1-D DIFFUSION SYSTEMS

As a preliminary step towards development of a low order real-time battery model, this chapter develops a model order reduction methodology for 1-D diffusion systems. Spatially distributed residues are found either analytically (from a transcendental transfer function) or numerically (from a finite element or finite difference model) and residues with similar eigenvalues are grouped together to reduce the model order. Two examples are presented from a simplified lithium ion battery model. Reduced order grouped models are compared to full order models and models of the same order in which optimal eigenvalues and residues are found numerically. The grouped models give near-optimal performance with roughly 1/20th the computation time of the full order models and require 1000-5000x less CPU time for numerical identification compared to the optimization procedure.

5.1 Reduction Framework

We restrict the present chapter to linear systems with single input and 1-D distributed output and seek to generate a reduced order model (ROM) whose output response, $y^*(x,t)$, accurately approximates the full order model (FOM) output response, $y(x,t)$, for any arbitrary input, $u(t)$. Analytical solutions to diffusion problems are commonly found by taking the Laplace transform of the governing PDE, solving it with respect to boundary conditions and inverting the Laplace or s-domain solution to generate a solution in the time domain. Denoting functions in the Laplace domain with capital letters, we have input $U(s)$, FOM output $Y(x,s)$, and ROM output $Y^*(x,s)$. We further restrict the work to systems with a steady state, that is $\lim_{s\to 0} Y(x,s)/U(s)$ is finite. The two examples given later in this chapter are each modified prior to reduction to meet this steady state requirement, ensuring that the ROM satisfies conservation of species across the 1-D domain.

Model order reduction is performed in the Laplace domain (which we loosely refer to as the frequency domain) and model error is quantified in the time domain. Design criteria in the frequency domain are

- correct steady-state, and

- $\| Y^*(x,j\omega) - Y(x,j\omega) \| < \alpha, \ \forall \ \omega \in [0, 2\pi f_c]$.

While the latter condition could be extended to bound the model error across the entire frequency range $\omega \in [0, \infty)$, the frequency response rolls off at high frequency and the ROM need only agree for $f < f_c$, where the bandwidth f_c is chosen to be sufficiently fast to resolve the dynamic response. To quantify error, $\hat{y} = y^* - y$, associated with a given ROM design, we simulate the response to a unit step in u at $t = 0$. For some applications, it may be appropriate to judge the error at one specific location, $x = x_i$ (*e.g.* at a sensor location), for which we define local L^2 and L^∞ norms as

$$L^2 = \left[\int_0^\infty | \hat{y}(x_i,t) |^2 dt \right]^{\frac{1}{2}}, \qquad (5.1)$$

$$L^\infty = \max_{t \in [0,\infty)} | \hat{y}(x_i,t) | .$$

For the more general case where the ROM must accurately describe system response across spatial domain $\Omega = \{x : x \in [0, 1]\}$, we define distributed L_Ω^2 and L_Ω^∞ norms as

$$L_\Omega^2 = \left[\int_0^\infty \int_\Omega | \hat{y}(x,t) |^2 \, dx \, dt \right]^{\frac{1}{2}}, \qquad (5.2)$$

$$L_\Omega^\infty = \max_{\Omega,\, t \in [0,\infty)} | \hat{y}(x,t) | .$$

5.2 Transcendental Transfer Function Approach

For many linear 1-D diffusion systems it is possible to analytically obtain a transcendental transfer function with an infinite number of poles,

$$\frac{Y(x,s)}{U(s)} = \frac{h(x,s)}{g(s)}, \qquad (5.3)$$

where $h(x,s)$ and $g(s)$ are the numerator and denominator, respectively. We desire a rational transfer function of order *n,*

$$\frac{Y^*(x,s)}{U(s)} = \frac{b_n(x)s^n + b_{n-1}(x)s^{n-1} + \ldots + b_1(x)s + b_0(x)}{a_n s^n + a_{n-1}s^{n-1} + \ldots + a_1 s + a_0}. \qquad (5.4)$$

5.2.1 Pole/Residue Series

We decompose Eq. (5.3) into a modal series finding the poles, p_k, with $g(p_k) = 0$, the unit step input steady state impedance

$$Z(x) = \lim_{s \to 0} \frac{h(x,s)}{g(s)}, \tag{5.5}$$

and unit step residues as

$$\mathrm{Res}_k(x) = \lim_{s \to p_k} (s - p_k)\, Y(x,s) = \lim_{s \to p_k} (s - p_k) \frac{h(x,s)}{s \cdot g(s)}. \tag{5.6}$$

Eq. (5.6) is valid for non-repeated p_k. If $h(x,p_k) \neq 0$ (see pp. 234-235 of Ref. [61]), then

$$\mathrm{Res}_k(x) = \left[\frac{h(x,s)}{s \cdot \frac{\partial}{\partial s} g(s)} \right]_{s=p_k}. \tag{5.7}$$

Using the poles, residues, and steady state impedance, the transcendental transfer function can be represented as an infinite series

$$\frac{Y(x,s)}{U(s)} = Z(x) + \sum_{k=1}^{\infty} \frac{\mathrm{Res}_k(x)\, s}{s - p_k}. \tag{5.8}$$

Substituting step input $U(s) = u / s$ into Eq. (5.8) and performing the inverse Laplace transform yields the time domain step response

$$y(x,t) = u \left[Z(x) + \sum_{k=1}^{\infty} \mathrm{Res}_k(x)\, \mathrm{e}^{p_k t} \right]. \tag{5.9}$$

5.2.2 Pole/Residue Truncation

An obvious method to represent a transcendental transfer function as a rational transfer function is to truncate Eq. (5.8) at n terms, yielding an n^{th} order transfer function

$$\frac{Y^*(x,s)}{U(s)} = Z(x) + \sum_{k=1}^{n} \frac{\mathrm{Res}_k(x)\, s}{s - p_k} \tag{5.10}$$

which may be expressed in the polynomial form of Eq. (5.4). For step input $U(s) = u / s$, the n^{th} order time domain model is

$$y^*(x,t) = u \left[Z(x) + \sum_{k=1}^{n} \mathrm{Res}_k(x)\, \mathrm{e}^{p_k t} \right]. \tag{5.11}$$

Order n may be chosen using either of the following criteria:

1. $p_n \approx -2\pi f_c$ $\quad (p_1 > p_2 > \ldots > p_\infty)$, or
2. $\|\mathrm{Res}_n(x)\| < \alpha$ $\quad (\|\mathrm{Res}_1\| > \|\mathrm{Res}_2\| > \ldots > \|\mathrm{Res}_\infty\|)$.

Condition 1 is useful when the simulation step size or a particular frequency range of interest is given. Condition 2 may be used in cases where the magnitude of the system input and required system output resolution (*e.g.* sensor accuracy) are given.

5.2.3 Pole/Residue Truncation + Grouping

Transcendental transfer functions are commonly characterized by numerous closely-spaced poles with similar residues. Accurate low order models can be obtained by dividing the frequency range of interest into d frequency "bins" and lumping poles within each bin. We define grouping indices $k_f \subseteq \{0,1,2,\ldots n\}$, arranged such that $0 = k_0 < k_1 < \ldots < k_d = n$. The grouped residue corresponding to bin $f \in \{1,2,\ldots d\}$ is

$$\overline{\mathrm{Res}}_f(x) = \sum_{k=k_{f-1}+1}^{k_f} \mathrm{Res}_k(x)\,. \tag{5.12}$$

Possible methods for choosing grouped pole location, $\bar{p}_f$, include:

1. Slowest pole

$$\bar{p}_f = \max\left\{p_{k_{f-1}+1},\, p_{k_{f-1}+2},\, \cdots\, p_{k_f}\right\}, \tag{5.13}$$

2. Largest residue

$$\bar{p}_f = \left\{p_k : \quad k = \sup_{k \in \{k_{f-1}+1,\ldots,k_f\}} \|\,\mathrm{Res}_k\,\|\right\}, \text{ or} \tag{5.14}$$

3. Residue-weighted pole

$$\bar{p}_f = \frac{\sum_{k=k_{f-1}+1}^{k_f} p_k\ \mathrm{Res}_k(x_i)}{\overline{\mathrm{Res}}_f(x_i)}\,. \tag{5.15}$$

Only the first two methods maintain poles from the original system. We find the third method, however, works best for the examples presented in Sec. 5.4. Equation (5.15) tends to place the grouped pole close to the mode with dominant response. Unlike Eq. (5.14), however, closely spaced modes with opposite sign residues cancel one another. Residues appearing in Eq. (5.15) are evaluated at a particular location x_i in the 1-D domain. The grouping procedure yields a d^{th} order transfer function

$$\frac{Y^*(x,s)}{U(s)} = Z(x) + \sum_{f=1}^{d} \frac{\overline{\mathrm{Res}}_f(x)\, s}{s - \overline{p}_f} . \tag{5.16}$$

5.2.4 Pole/Residue Optimization

To assess the efficiency of the grouping method, we compare the grouped ROMs to ROMs of the same order in which poles and residues (denoted with double overbars) are found numerically to minimize a cost functional. The optimal ROM transfer function is

$$\frac{Y^*(x_i,s)}{U(s)} = Z(x_i) + \sum_{f=1}^{d} \frac{\overline{\overline{\mathrm{Res}}}_{i,f}\; s}{s - \overline{\overline{p}}_f} . \tag{5.17}$$

Unlike Eq. (5.16), the residues in Eq. (5.17) hold no connection to the analytical solution and must be found at discrete locations x_i across the spatial domain. We numerically solve for $\overline{\overline{\mathrm{Res}}}_{i,f}$ and $\overline{\overline{p}}_f$ that minimize the frequency response cost functional

$$J = \sum_{k=1}^{n_\omega} \sum_{i=1}^{n_x} \left| \operatorname{Re}\left(Y^*(x_i, j\omega_k) - Y(x_i, j\omega_k)\right) \right|^2 + \left| \operatorname{Im}\left(Y^*(x_i, j\omega_k) - Y(x_i, j\omega_k)\right) \right|^2 \tag{5.18}$$

as shown in Appendix D [62,63]. Equation (5.18) includes real and imaginary error-squared terms to retain proper magnitude and phase angle in the discretized transfer function.

5.3 State Space Approach

If it is not convenient to obtain an analytical transfer function of a 1-D linear diffusion system, then a linear SIMO state space model with *m* states and *m* outputs can be obtained as follows

$$\begin{aligned} \dot{\mathbf{x}} &= \mathbf{A}\mathbf{x} + \mathbf{B}u , \\ \mathbf{y} &= \mathbf{C}\mathbf{x} + \mathbf{D}u , \end{aligned} \tag{5.19}$$

using finite element or finite difference methods. We desire a reduced order model with *n* states ($n < m$) and *m* outputs

$$\begin{aligned} \dot{\mathbf{x}}^* &= \mathbf{A}^*\mathbf{x}^* + \mathbf{B}^*u , \\ \mathbf{y}^* &= \mathbf{C}^*\mathbf{x}^* + \mathbf{D}^*u . \end{aligned} \tag{5.20}$$

The transfer matrix of the SIMO state space model (5.19) is

$$\frac{\mathbf{Y}(s)}{U(s)} = \mathbf{C}(s\mathbf{I} - \mathbf{A})^{-1}\mathbf{B} + \mathbf{D} . \tag{5.21}$$

5.3.1 Eigenvalue/Residue Series

Similar to expressions presented in Sec. 5.1, the transfer matrix (5.21) can be represented in the eigenvector/residue series

$$\frac{\mathbf{Y}(s)}{U(s)} = \mathbf{Z} + \sum_{k=1}^{m} \frac{\mathbf{r}_k\ s}{s-\lambda_k}. \tag{5.22}$$

The m x 1 steady state vector, found by setting $\dot{\mathbf{x}} = 0$ in Eq. (5.19), is

$$\mathbf{Z} = -\mathbf{C}\mathbf{A}^{-1}\mathbf{B} + \mathbf{D}. \tag{5.23}$$

To find the unit step input residue, $\mathbf{r}_k$, we substitute Eq. (5.22) with U(s) = 1 / s into Eq. (5.6) yielding

$$\mathbf{r}_k = \lim_{s\to\lambda_k} (s-\lambda_k) \left[\frac{\mathbf{C}(s\mathbf{I}-\mathbf{A})^{-1}\mathbf{B}}{s} + \frac{\mathbf{D}}{s} \right]. \tag{5.24}$$

The second term in the brackets goes to zero in the limit. We can solve for the first term in the brackets using the m x 1 right eigenvector, $\mathbf{q}_k$, with

$$\mathbf{A}\mathbf{q}_k = \lambda_k \mathbf{q}_k \tag{5.25}$$

and the 1 x m left eigenvector, $\mathbf{p}_k$, with

$$\mathbf{p}_k \mathbf{A} = \lambda_k \mathbf{p}_k. \tag{5.26}$$

If all eigenvalues of **A** are distinct and $\mathbf{p}_k\mathbf{q}_k = 1$ (Ref. [23], pg 84), then

$$(s\mathbf{I}-\mathbf{A})^{-1} = \sum_{k=1}^{n} \frac{1}{s-\lambda_k} \mathbf{q}_k \mathbf{p}_k. \tag{5.27}$$

Substitution of Eq. (5.27) into Eq. (5.24) yields

$$\mathbf{r}_k = \lim_{s\to\lambda_k} \frac{\mathbf{C}}{s} \left[\mathbf{q}_1\mathbf{p}_1 \left(\frac{s-\lambda_k}{s-\lambda_1} \right) + \mathbf{q}_2\mathbf{p}_2 \left(\frac{s-\lambda_k}{s-\lambda_2} \right) + \ldots + \mathbf{q}_k\mathbf{p}_k + \ldots + \mathbf{q}_n\mathbf{p}_n \left(\frac{s-\lambda_k}{s-\lambda_n} \right) \right] \mathbf{B}. \tag{5.28}$$

In the limit, all terms except $\mathbf{q}_k\mathbf{p}_k$ go to zero leaving the m x 1 residue vector

$$\mathbf{r}_k = \frac{\mathbf{C}\mathbf{q}_k\mathbf{p}_k\mathbf{B}}{\lambda_k}. \tag{5.29}$$

Using the residues in Eq. (5.29), we can rewrite Eq. (5.19) in modal form (see Appendix E)

$$\begin{aligned} \dot{\hat{\mathbf{x}}} &= \hat{\mathbf{A}}\hat{\mathbf{x}} + \hat{\mathbf{B}}u, \\ \mathbf{y} &= \hat{\mathbf{C}}\hat{\mathbf{x}} + \hat{\mathbf{D}}u, \end{aligned} \tag{5.30}$$

where

$$\begin{aligned}
\hat{\mathbf{A}} &= diag\begin{bmatrix}\lambda_1 & \lambda_2 & \cdots & \lambda_m\end{bmatrix}, \\
\hat{\mathbf{B}} &= \begin{bmatrix}1 & 1 & \cdots & 1\end{bmatrix}^{\mathrm{T}}, \\
\hat{\mathbf{C}} &= \begin{bmatrix}\mathbf{r}_1\lambda_1 & \mathbf{r}_2\lambda_2 & \cdots & \mathbf{r}_m\lambda_m\end{bmatrix}, \\
\hat{\mathbf{D}} &= \left[\mathbf{Z} + \sum_{k=1}^{m} \mathbf{r}_k\right] = \mathbf{D}.
\end{aligned} \tag{5.31}$$

5.3.2 Eigenvalue/Residue Truncation

As in Sec. 5.1, we may reduce the m^{th} order model by truncating Eq. (5.22) at n terms, yielding an n^{th} order transfer matrix

$$\frac{\mathbf{Y}^*(s)}{U(s)} = \mathbf{Z} + \sum_{k=1}^{n} \frac{\mathbf{r}_k\ s}{s - \lambda_k} \tag{5.32}$$

and an n^{th} order state space model, Eq. (5.20), in modal form with

$$\begin{aligned}
\mathbf{A}^* &= diag\begin{bmatrix}\lambda_1 & \lambda_2 & \cdots & \lambda_n\end{bmatrix}, \\
\mathbf{B}^* &= \begin{bmatrix}1 & 1 & \cdots & 1\end{bmatrix}^{\mathrm{T}}, \\
\mathbf{C}^* &= \begin{bmatrix}\mathbf{r}_1\lambda_1 & \mathbf{r}_2\lambda_2 & \cdots & \mathbf{r}_n\lambda_n\end{bmatrix}, \\
\mathbf{D}^* &= \left[\mathbf{Z} + \sum_{k=1}^{n} \mathbf{r}_k\right].
\end{aligned} \tag{5.33}$$

Order n may be chosen using the bandwidth or magnitude criteria

1. $\lambda_n \approx -2\pi f_c$ $(\lambda_1 > \lambda_2 > \ldots > \lambda_m)$, or
2. $\|\mathbf{r}_n\| < \alpha$ $(\|\mathbf{r}_1\| > \|\mathbf{r}_2\| > \ldots > \|\mathbf{r}_m\|)$.

5.3.3 Eigenvalue/Residue Truncation + Grouping

Using the approach in Sec. 5.1.3, we parcel the frequency range of interest into d bins and group together modes within each bin. The m x 1 grouped residue vector corresponding to bin f is

$$\bar{\mathbf{r}}_f = \sum_{k=k_{f-1}+1}^{k_f} \mathbf{r}_k \tag{5.34}$$

with corresponding grouped eigenvalue, $\bar{\lambda}_f$, placed using the residue-weighted eigenvalue rule

$$\bar{\lambda}_f = \frac{\sum\limits_{k=k_{f-1}+1}^{k_f} \lambda_k \ r_{i,k}}{\bar{r}_{i,f}} . \tag{5.35}$$

where $\mathbf{r}_k = [r_{1,k}, \ldots \, r_{m,k}]^{\mathrm{T}}$ with $r_{i,k}$ corresponding to spatial location x_i. The grouping procedure yields a d^{th} order transfer matrix

$$\frac{\mathbf{Y}^*(s)}{U(s)} = \mathbf{Z} + \sum_{f=1}^{d} \frac{\bar{\mathbf{r}}_f \ s}{s - \bar{\lambda}_f} \tag{5.36}$$

and a d^{th} order state space model

$$\begin{aligned}
\mathbf{A}^* &= diag\left[\bar{\lambda}_1 \quad \bar{\lambda}_2 \quad \cdots \quad \bar{\lambda}_d\right], \\
\mathbf{B}^* &= \left[1 \quad 1 \quad \cdots \quad 1\right]^{\mathrm{T}}, \\
\mathbf{C}^* &= \left[\bar{\mathbf{r}}_1 \bar{\lambda}_1 \quad \bar{\mathbf{r}}_2 \bar{\lambda}_2 \quad \cdots \quad \bar{\mathbf{r}}_d \bar{\lambda}_d\right], \\
\mathbf{D}^* &= \left[\mathbf{Z} + \sum_{f=1}^{d} \bar{\mathbf{r}}_f\right].
\end{aligned} \tag{5.37}$$

5.3.4 Eigenvalue/Residue Optimization

We introduce the d^{th} order transfer matrix

$$\frac{\mathbf{Y}^*(s)}{U(s)} = \mathbf{Z} + \sum_{f=1}^{d} \frac{\bar{\bar{\mathbf{r}}}_f \ s}{s - \bar{\bar{\lambda}}_f} . \tag{5.38}$$

and numerically solve for optimal eigenvalues, $\bar{\bar{\lambda}}_f$, and residue vectors, $\bar{\bar{\mathbf{r}}}_f$, which minimize the error cost functional

$$J = \sum_{k=1}^{n_\omega} \sum_{i=1}^{n_x} \left| \operatorname{Re}\left(Y_i^*(j\omega_k) - Y_i(j\omega_k)\right)\right|^2 + \left| \operatorname{Im}\left(Y_i^*(j\omega_k) - Y_i(j\omega_k)\right)\right|^2 \tag{5.39}$$

where Y_i^* and Y_i are the i^{th} outputs (corresponding to response at location $x = x_i$) of the reduced and original state space models, respectively.

5.4 Examples

We illustrate the model order reduction technique using two examples arising from species conservation within the 6 Ah HEV battery. In the first example, solid state diffusion, we apply the model order reduction methods from Sec. 5.2 to an analytical solution. For the second example, electrolyte phase diffusion, composite geometry makes analytical treatment cumbersome. We use the finite element method to derive a state space model and then reduce its order using the methods from Sec. 5.3.

5.4.1 Solid State Diffusion

A schematic of the solid state diffusion problem is shown in Fig. 5.1. Repeated from Chapter 2 for convenience, the distribution of Li concentration, $c_s(r,t)$, within a single particle is described by

$$\frac{\partial c_s}{\partial t} = \frac{D_s}{r^2}\frac{\partial}{\partial r}\left(r^2 \frac{\partial c_s}{\partial r}\right) \tag{5.40}$$

with a boundary condition that enforces symmetry at the particle center

$$\left.\frac{\partial c_s}{\partial r}\right|_{r=0} = 0, \tag{5.41}$$

and a time-dependent boundary condition at the particle surface,

$$-D_s \left.\frac{\partial c_s}{\partial r}\right|_{r=R_s} = \frac{j^{Li}(t)}{a_s F} \tag{5.42}$$

where D_s is the diffusion coefficient, $j^{Li}(t)$ is the volumetric reaction current, a_s is the specific interfacial surface area, and F is Faradays constant. For the simple case of uniform current density across the electrode, j^{Li} equals the total current, I, divided by electrode volume. We seek a reduced order model with input $j^{Li}(t)$ and surface concentration output $c_{s,e}(t) = c_s(R_s,t)$.

Taking the Laplace transform of Eq. (5.40) and finding a solution that satisfies the boundary conditions, Eqs. (5.41) and (5.42), Jacobsen and West [54] obtain the transcendental transfer function,

$$\frac{C_{s,e}(s)}{J^{Li}(s)} = \frac{1}{a_s F}\left(\frac{R_s}{D_s}\right)\left[\frac{\tanh(\beta)}{\tanh(\beta) - \beta}\right], \tag{5.43}$$

with $\beta = R_s\sqrt{s/D_s}$. While the Laplace domain solution (5.43) is compact and closed form, no similarly compact time domain solution is available. Though not immediately obvious, Eq. (5.43) contains a free integrator term which rises and falls with the particle's bulk concentration, yielding an infinite steady state solution. Bulk concentration of a sphere with time-dependent surface flux $j^{Li}(t) / (a_s F)$ is described by the ODE

$$\frac{dc_{s,avg}}{dt} = -\frac{3}{R_s}\frac{j^{Li}(t)}{a_s F}, \tag{5.44}$$

where the factor $3/R_s$ results from the area to volume ratio of the sphere. The Laplace transform of Eq. (5.44) yields a transfer function for the bulk response

$$\frac{C_{s,avg}(s)}{J^{Li}(s)} = \frac{-3}{R_s a_s F}\frac{1}{s}\cdot \tag{5.45}$$

Subtracting Eq. (5.45) from Eq. (5.43) and defining $\Delta C_{s,e}(s) = C_{s,e}(s) - C_{s,avg}(s)$ yields

$$\frac{\Delta C_{s,e}(s)}{J^{Li}(s)} = \frac{1}{a_s F}\left(\frac{R_s}{D_s}\right)\left[\frac{(\beta^2+3)\tanh(\beta) - 3\beta}{\beta^2(\tanh(\beta) - \beta)}\right] \tag{5.46}$$

which, unlike Eq. (5.43), has a finite steady state. Following model order reduction, the bulk response is reintroduced, giving a low order approximation to Eq. (5.43) that satisfies Li conservation.

Equation (5.46) is decomposed into a modal series following the procedure in Sec. 5.2.1. The poles of Eq. (5.46) are

$$p_k = -D_s\left(\frac{\xi_k}{R_s}\right)^2, \tag{5.47}$$

where ξ_k are roots of $\tan(\xi_k) = \xi_k$ not including $\xi_0 = 0$. The residues of Eq. (5.46) are

$$\mathrm{Res}_k = \frac{-2}{a_s F R_s p_k} \tag{5.48}$$

and the steady state solution is

$$Z = \frac{-R_s}{5 a_s F D_s}\cdot \tag{5.49}$$

Substituting Eqs. (5.47)-(5.49) into Eq. (5.8) yields an infinite series transfer function algebraically equivalent to Eq. (5.46).

Using 6Ah battery model parameters defined in Table 3.1, the characteristic time $t \approx R_s^2 / D_s = 5000$ seconds indicates that it can take over an hour for solid phase concentration gradients to completely stabilize. Discussed in Chapter 3, a high rate current pulse may become solid state transport-limited in as little time as 5 seconds. These disparate time scales complicate the derivation of an accurate low order model. In the present example, we seek to approximate solid state diffusion dynamics from steady state to f_c = 10 Hz, a bandwidth sufficient to capture major pulse events for an HEV battery.

Figure 5.2 plots poles, Eq. (5.47), versus residues, Eq. (5.48), with the slowest pole (and largest residue) of the analytical solution located at -4.04×10^{-3} rad/s. Faster poles are spaced progressively closer together. In the lower left corner of Fig. 5.2, discrete pole/residue pairs appear as almost a continuum of points. Using the truncation method, we retain all poles $p_k > -2\pi f_c$. In the limit, roots of the characteristic equation, $\tan(\xi_k) = \xi_k$ approach $\xi_k = (k + ½)\pi$. Substituted into Eq. (5.47), the truncation method thus requires

$$n \approx R_s\sqrt{\frac{2f_c}{D_s\pi}} - \tfrac{1}{2} \tag{5.50}$$

terms. For the present model parameters and f_c = 10 Hz, n = 178 demonstrating that the truncation approach of Sec. 5.2.2 can result in a high order model.

The grouping approach introduced in Sec. 5.2.3 is motivated by the observation that analytical poles in Fig. 5.2 are tightly spaced with similar residues. A simple grouping approach is to use brackets to partition the real axis into d bins of equal width. Shown in Fig. 5.2 for a fifth order grouped model, we place the slowest bracket at $p_1 / 2$ and the fastest bracket at $-4\pi f_c$. The four intermediate brackets are evenly spaced on a logarithmic scale. The grouped residue of each bin is the sum of all residues in that bin, as defined by Eq. (5.12). The corresponding pole is located using the residue-weighted pole rule, Eq. (5.15). Fifth order grouped pole/residue pairs are plotted with circles in Fig. 5.2.

Figure 5.3 compares the frequency response of a truncated model, Eq. (5.10), and two grouped models, Eq. (5.16), with the exact frequency response, Eq. (5.46). The 180 term truncated series approximation matches the exact magnitude and phase until near 10 Hz where the phase angle diverges from the exact solution. Third and 5th order grouped models have similar characteristics, with the 5th order model producing a better match. The 3rd order grouped model clearly overpredicts the exact magnitude. Phase angle for the grouped models has the qualitative appearance of a curve fit.

Using the method introduced in Sec. 5.2.4, Fig. 5.4 shows 3rd and 5th order optimal models, Eq. (5.17), that minimize the cost functional, Eq (5.18). Each optimization case is run multiple times with different initial parameter guesses to ensure convergence to a global optimum. The optimal models are only slightly more accurate at matching the exact frequency response than their grouped counterparts of the same order. Magnitude is alternately underpredicted and overpredicted across the frequency range. Fifth order optimal pole/residue pairs, plotted with "x" symbols in Fig. 5.2, lie very close to the 5th order grouped pole/residue pairs.

Figure 5.5 compares the unit step response of a 5th order grouped model and a 5th order optimal model to a high order truncated "truth" model. Initially the optimal model has a larger percentage error than the grouped model. The optimal error, however, more quickly decays to zero. The L^2 and L^∞ norms of surface concentration are presented in Table 5.1 for 3rd, 4th, and 5th order grouped and optimal models. The norms decrease with increasing model order for both types of reduced order models. Optimal models give slightly improved performance compared to grouped models. In cases where analytical poles, residues, and steady state solutions are easy to find, however, the grouped pole/residue method generates accurate reduced models of arbitrary order with inexpensive computation.

5.4.2 Electrolyte Phase Diffusion

A schematic of the second example, electrolyte diffusion, is shown in Fig. 5.6. Repeated from Chapter 2 for convenience, distribution of electrolyte concentration, $c_e(x,t)$, across the 1-D cell domain is described by

$$\frac{\partial(\varepsilon_e c_e)}{\partial t} = \frac{\partial}{\partial x}\left(D_e \frac{\partial}{\partial x} c_e\right) + \frac{1-t^o}{F} j^{Li} \tag{5.51}$$

with zero flux conditions at the cell boundaries

$$\left.\frac{\partial c_e}{\partial x}\right|_{x=0} = \left.\frac{\partial c_e}{\partial x}\right|_{x=L_{cell}} = 0. \tag{5.52}$$

In this chapter we consider the simple case of uniform current density across each electrode, where current density, j^{Li}, equals total current, I, divided by electrode volume. A Bruggeman relationship, $D_e = D_e^{ref} \varepsilon_e^{1.5}$, corrects the reference diffusion coefficient for the tortuous path Li$^+$ ions follow through the porous media. Properties ε_e and D_e, and source term j^{Li}, have different constant values in the negative electrode, separator, and positive electrode regions as follows

$$\begin{aligned}
&\text{Neg. Electrode:} \quad && D_{e-} = D_e^{ref} {\varepsilon_{e-}}^{1.5}, && j_-^{Li} = \frac{I}{A\delta_-} \\
&\text{Separator:} \quad && D_{e,sep} = D_e^{ref} {\varepsilon_{e,sep}}^{1.5}, && j_{sep}^{Li} = 0 \\
&\text{Pos. Electrode:} \quad && D_{e+} = D_e^{ref} {\varepsilon_{e+}}^{1.5}, && j_+^{Li} = \frac{-I}{A\delta_+}.
\end{aligned}$$

Analytical treatment requires three individual solutions – one for each region – connected by concentration and flux matching conditions at the negative electrode/separator and separator/positive electrode interfaces. The finite element method allows a more convenient single domain approach because the assembly process automatically satisfies internal matching conditions.

Spatially discretizing the 1-D domain with m linear basis functions, the finite element model represents $c_e(x,t)$ as an m x 1 vector $\mathbf{c}_e(t)$ containing values of concentration at discrete node points, $x = x_i$, where $i \in \{1,2,\ldots m\}$. The finite element representation of Eq. (5.51) is

$$\mathbf{M}\,\dot{\mathbf{c}}_e = -\mathbf{K}\,\mathbf{c}_e + \mathbf{F}\,I \tag{5.53}$$

where **M**, **K**, and **F** are the mass, stiffness, and forcing matrices respectively [64]. Multiplying through by $\mathbf{M}^{-1}$ yields

$$\dot{\mathbf{c}}_e = -\mathbf{M}^{-1}\,\mathbf{K}\,\mathbf{c}_e + \mathbf{M}^{-1}\mathbf{F}\,I \tag{5.54}$$

and the model is now expressed in linear state variable form, Eq. (5.19). Equation (5.54) is not a minimal realization due to a pole/zero cancellation at the origin. To strictly enforce species conservation, we define a new field variable $\Delta c_e(x,t) = c_e(x,t) - c_e(0,t)$, and Eq. (5.54) becomes

$$\Delta\dot{\mathbf{c}}_e = -(\mathbf{M}^{-1}\,\mathbf{K})_\Delta\,\Delta\mathbf{c}_e + (\mathbf{M}^{-1}\,\mathbf{F})_\Delta\,I \tag{5.55}$$

where the (m-1) x (m-1) matrix $(\mathbf{M}^{-1}\mathbf{K})_\Delta$ is generated by subtracting the first row of m x m matrix $(\mathbf{M}^{-1}\mathbf{K})$ from each row of $(\mathbf{M}^{-1}\mathbf{K})$ and dropping the first row and first column. Similarly, the (m-1) x 1 vector $(\mathbf{M}^{-1}\mathbf{F})_\Delta$ is generated by subtracting the first row of $\mathbf{M}^{-1}\mathbf{F}$ from each row of $\mathbf{M}^{-1}\mathbf{F}$ and dropping the first row. With states $\mathbf{x} = \Delta\mathbf{c}_e$, the state variable model, Eq. (5.19), is defined by $\mathbf{A} = -(\mathbf{M}^{-1}\mathbf{K})_\Delta$, $\mathbf{B} = (\mathbf{M}^{-1}\mathbf{F})_\Delta$, $\mathbf{C} = \mathbf{I}$, and $\mathbf{D} = 0$.

For the present example, we discretize the 1-D domain using 45 linear basis elements. CFD modelers commonly perform a grid independence test to check whether spatial discretization has been performed with a fine enough mesh. Results from a coarse mesh model are compared to those from a fine mesh model to validate the lower order model. Here, the grouping method efficiently produces low order models from the high order models associated with fine meshes.

Figure 5.7 plots eigenvalues of the **A** matrix versus residues, calculated with Eq. (5.29), at the location $x = L$. To distinguish the sign of each residue on the log-log plot, Fig. 5.7 uses different symbols for residues with positive magnitude versus those with negative magnitude. In the present example, the source term in the negative electrode is offset by a sink term in the positive electrode. Adjacent residues in Fig. 5.7 generally have alternating sign, causing near pole/zero cancellations and further motivating the grouping method introduced in Sec. 5.3.3. Applying the same grouping procedure as the previous example, Fig. 5.7 shows brackets and eigenvalue/residue pairs corresponding to a 3rd order grouped model.

Figure 5.8 compares the frequency response of a model truncated at 10 Hz and a 3rd order grouped model with the full order model frequency response. Results shown are at $x = L$, but the 3rd order grouped model provides similar accuracy across the entire spatial domain. Unlike the previous example, the low order model tightly matches the high order model phase angle.

Using the method introduced in Sec. 5.3.4, Fig. 5.9 presents 2nd and 3rd order optimal models in which empirical eigenvalues and residues are numerically fit to the 45th order finite element model frequency response. Both the 2nd and 3rd order optimal models are accurate at the location $x = L$. The L_{Ω}^{2} and L_{Ω}^{∞} norms, evaluated from unit step response simulation results, are displayed in Table 5.2, providing a quantitative metric of performance across the entire 1-D domain. Judged on this basis, the 3rd order optimal model has 4-6 times better performance than the 2nd order optimal model. A similar trend is evident for the 2nd and 3rd order grouped models.

Figure 5.10 compares the unit step response of a 3rd order grouped model and a 3rd order optimal model with the full finite element model across the entire spatial domain. Small differences between the grouped and optimal models occur near the separator region. In general, the grouped residue models are near optimal and grouped model performance improves as model order is increased. An exception is noted in Table 5.2, where the 4th order grouped model shows worse performance than the 3rd order grouped model and is far from optimal. Here, our simple approach of partitioning the eigenspectrum with logarithmic evenly-spaced brackets has not yielded the best possible 4th order grouped model. By manually adjusting the bracket placement, it is possible to obtain other 4th order grouped models with performance close to the 4th order optimal model.

5.5 Conclusions

Residue grouping is a convenient method for combining closely spaced modes of a distributed parameter system with negative real eigenvalues. In traditional finite element or finite difference model grid generation, discretization presents a tradeoff between model size and spatial resolution, with the former impacting execution speed and numerical stability. Using the approach in this chapter to reduce the order of a model generated with very fine mesh grid, a low order model can be obtained with good spatial resolution.

Reduced order grouped models are shown to provide near-optimal performance, matching full order simulation results to within 6.3% for the 5th order solid state diffusion model and 1.2% for the 3rd order electrolyte diffusion model. Compared to the 180th order truncated solid state diffusion model and the 45th order finite element electrolyte diffusion model, these grouped models execute 36x and 15x faster, respectively. The grouping procedure identifies these models using just 0.01 and 0.07 seconds CPU time on a 1200 MHz Pentium III processor, compared to 8.1 and 390 seconds, respectively, for the optimization procedure.

Model order reduction is performed in the frequency domain, and for control applications where only a rough approximate model is required, one may quickly obtain low order models with reasonable accuracy across a wide frequency range. As with the Karhuenen-Loève Galerkin procedure [34], eigenvalue decomposition is a necessary step for generating a reduced order model, however in the present investigation, the model itself is decomposed rather than field variable time response, eliminating the need for time simulation. Although this restricts the method to linear systems, it saves computation time and maintains a tighter connection between the parameters of the full and reduced models.

Model Order	Reduction Method	Surface Concentration [mol/cm^3 x 10^{-4}]	
		L^2	L^∞
3	Grouped	5.28	9.84
	Optimal	2.50	4.07
4	Grouped	3.19	5.31
	Optimal	1.261	2.24
5	Grouped	1.742	2.61
	Optimal	1.178	2.18

Table 5.1. Solid state diffusion reduced order model error norms.

Model Order	Reduction Method	Electrolyte Concentration [mol/cm^3 x 10^{-7}]	
		L_Ω^2	L_Ω^∞
2	Grouped	0.821	4.90
	Optimal	0.820	4.89
3	Grouped	0.1601	1.161
	Optimal	0.1435	1.098
4	Grouped	0.1618	1.167
	Optimal	0.0163	0.082

Table 5.2. Electrolyte phase diffusion reduced order model error norms.

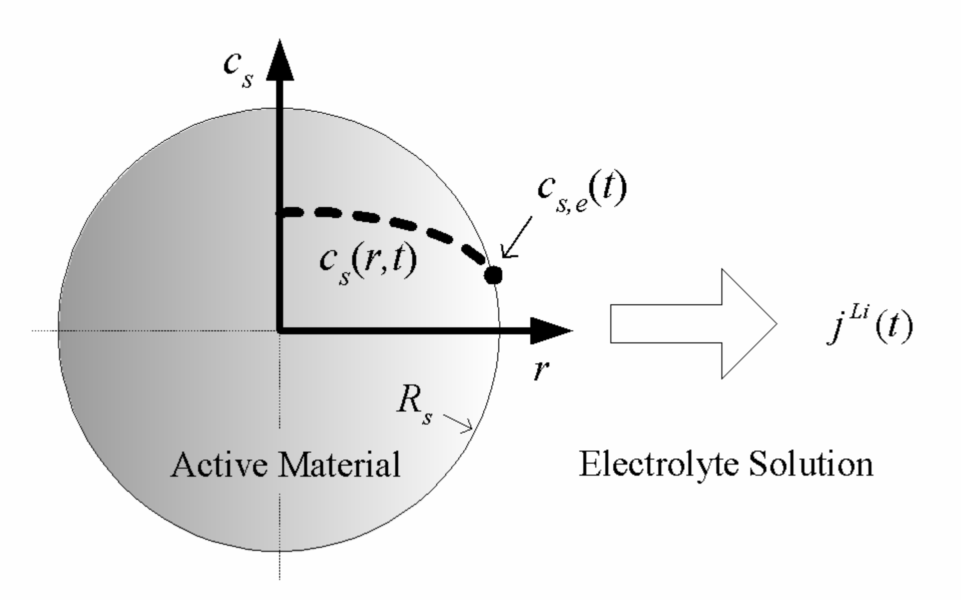

Figure 5.1. Solid state diffusion problem.

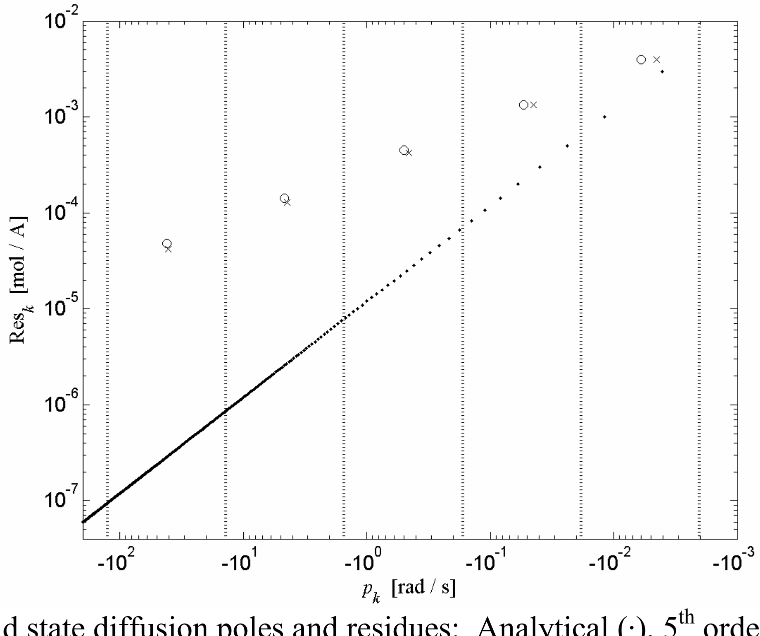

Figure 5.2. Solid state diffusion poles and residues: Analytical (·), 5th order grouped (○), and 5th order optimal (x). 5th order grouping brackets shown with vertical dotted lines.

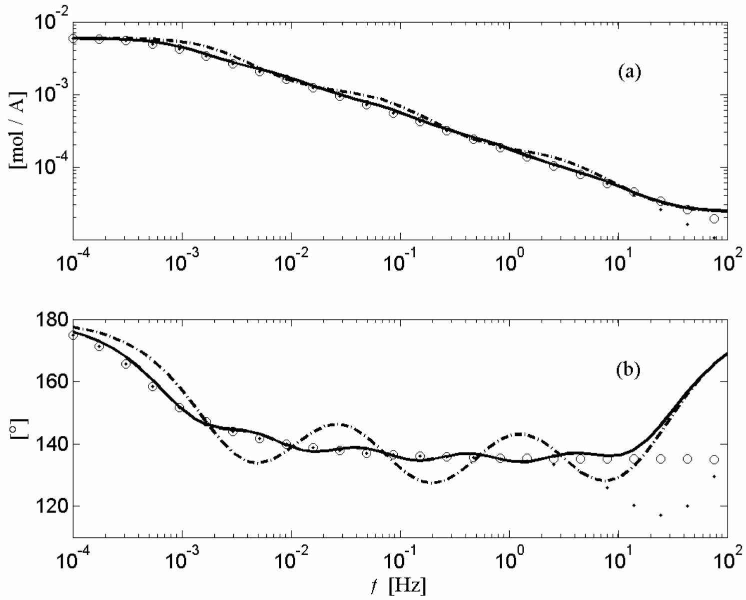

Figure 5.3. Truncated and grouped solid state diffusion ROMs vs. exact frequency response: Exact (○), 180th order truncated (·), 3rd order grouped (−·), and 5th order grouped (−). (a) Magnitude, $|\Delta C_{s,e}(s) \,/\, J^{Li}(s)|$. (b) Phase angle, $\angle(\Delta C_{s,e}(s) \,/\, J^{Li}(s))$.

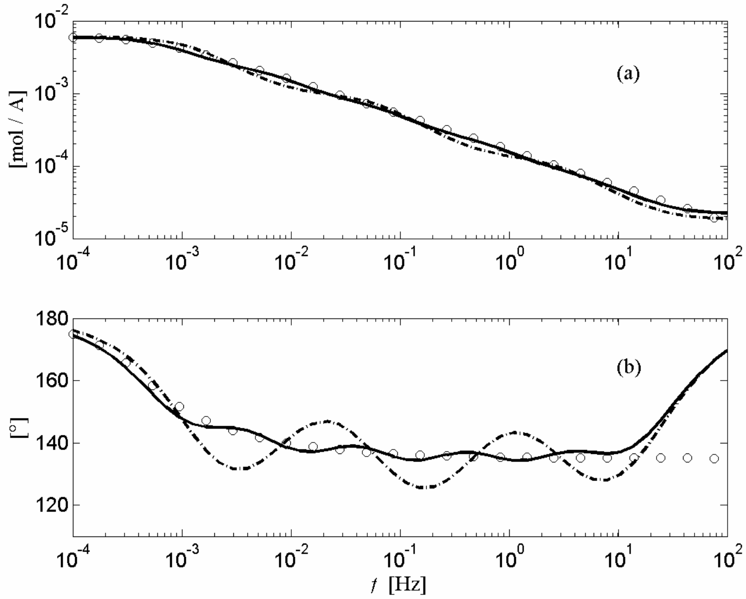

Figure 5.4. Optimal solid state diffusion ROMs versus exact frequency response: Exact (○), 3rd order optimal (−·), and 5th order optimal (−). (a) Magnitude, $|\Delta C_{s,e}(s) \,/\, J^{Li}(s)|$. (b) Phase angle, $\angle(\Delta C_{s,e}(s) \,/\, J^{Li}(s))$.

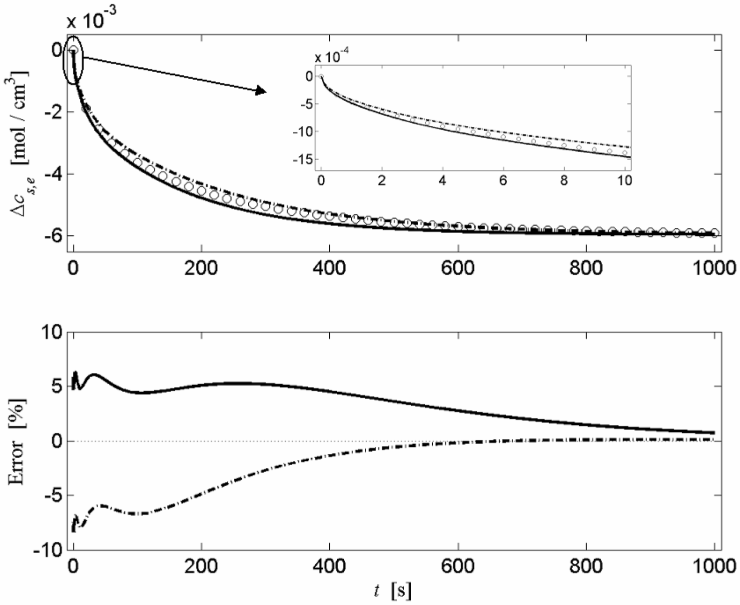

Figure 5.5. Grouped and optimal solid state diffusion ROMs versus higher order model unit step response: 1000th order truncated (○), 5th order grouped (−), and 5th order optimal (−·).

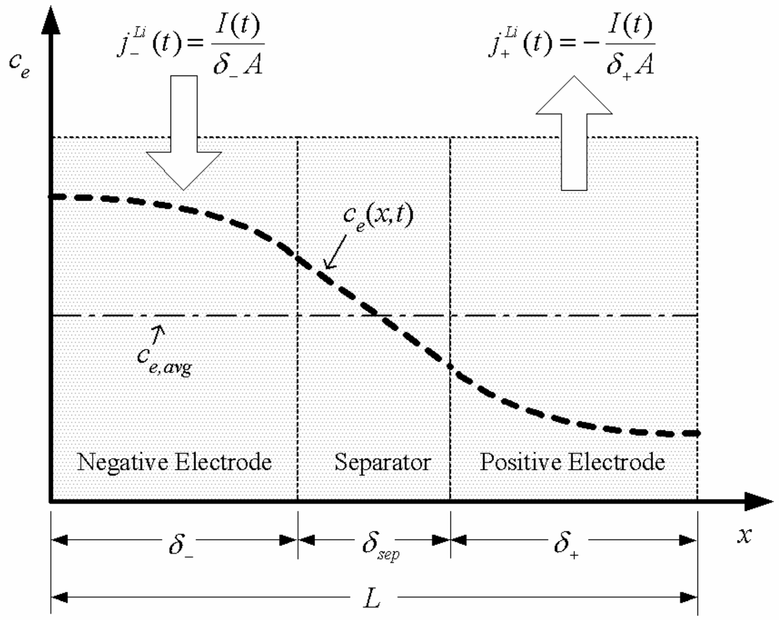

Figure 5.6. Electrolyte phase diffusion problem for Li-ion cell with uniform reaction current distribution.

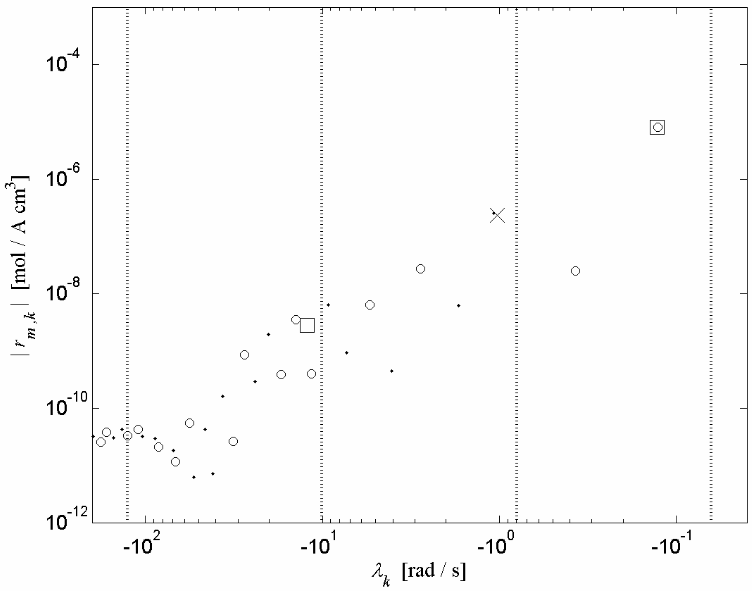

Figure 5.7. Electrolyte phase diffusion eigenvalues and residues at $x = L$: 45th order finite element $r_{m,k} > 0$ (○) and $r_{m,k} < 0$ (·), and 3rd order grouped $\bar{r}_{m,k} > 0$ (□) and $\bar{r}_{m,k} < 0$ (x). 3rd order grouping brackets shown with vertical dotted lines.

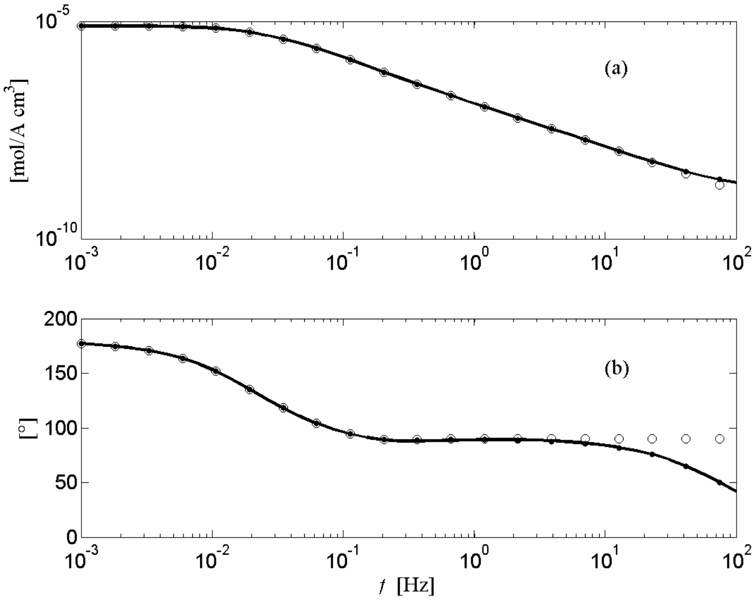

Figure 5.8. Truncated and grouped electrolyte phase diffusion ROMs versus higher order model frequency response at $x = L$: 45th order finite element (○), 28th order truncated (·), and 3rd order grouped (−). (a) Magnitude, $|\Delta C_e(L,s) / I(s)|$. (b) Phase angle, $\angle(\Delta C_e(L,s) / I(s))$.

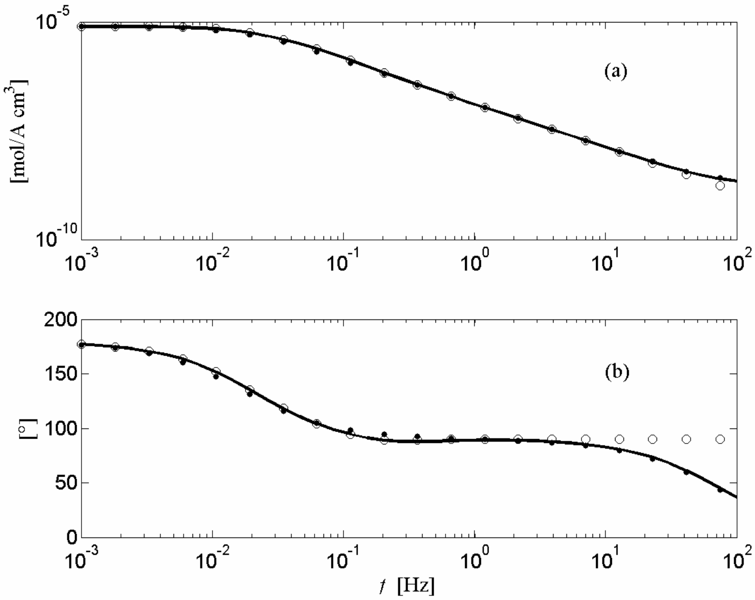

Figure 5.9. Optimal electrolyte phase diffusion ROMs versus higher order model frequency response at $x = L$: 45th order finite element (○), 2nd order optimal (·), and 3rd order optimal (−). (a) Magnitude, $|\Delta C_e(L,s) / I(s)|$. (b) Phase angle, $\angle(\Delta C_e(L,s) / I(s))$.

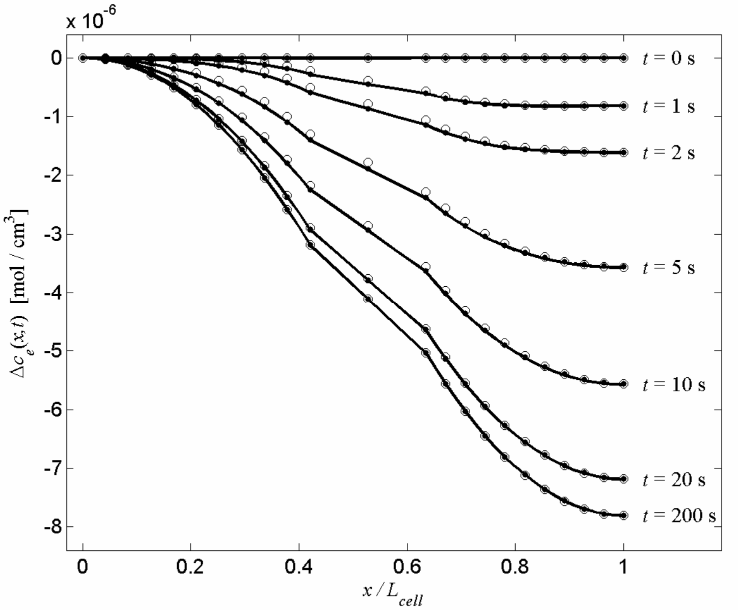

Figure 5.10. Grouped and optimal electrolyte phase diffusion ROMs versus higher order model unit step response: 45th order finite element (○), 3rd order grouped (−), and 3rd order optimal (·).

Chapter 6 – CONTROL-ORIENTED 1-D ELECTROCHEMICAL MODEL

This chapter derives transfer functions/matrices from the electrochemical kinetic, species and charge partial differential equations introduced in Chapter 2, reduces their order using the cost function minimization method introduced in Chapter 5, and numerically generates a state variable model of the 6Ah Li-ion battery. Validated against the CFD model, a 12th order state variable model predicts terminal voltage to within 25 mV (<1%) for pulse and constant current profiles at rates up to 50C. Open circuit potential, electrode surface concentration/reaction distribution coupling, and electrolyte concentration/ionic conductivity nonlinearities are explicitly approximated in the model output equation on a local, electrode-averaged, and distributed basis, respectively. Controllability and observability properties of the model are discussed.

6.1 Impedance Model Derivation

We manipulate the governing equations (Chapter 2) to derive analytical transfer functions in Sec. 6.1.1 and numerical transfer matrices in Sec. 6.1.2 describing the output response of the impedance model field variables $\bar{c}_{s,e}(x,s)$, $\bar{c}_e(x,s)$, $\bar{\phi}_s(x,s)$, and $\bar{\phi}_e(x,s)$ to an input current, $\bar{I}(s)$, where the overbar denotes a Laplace-transformed variable. Individual submodels are combined to form the voltage response, $\bar{V}(s)$, in Sec. 6.1.3. In preparation for model order reduction, transfer functions/matrices are modified as necessary so that they have finite steady state solution. Impedance model assumptions are:

(i) Linear behavior (i.e. constant properties), and

(ii) Reaction current, $\bar{j}^{Li}(x,s)$, decoupled from electrolyte concentration, $\bar{c}_e(x,s)$.

For other fundamental impedance models, see [13,50,65] and the references therein.

6.1.1 Electrode Submodel

Repeated here for convenience, the solid state diffusion impedance of a spherical active material particle is [54]

$$\frac{\bar{c}_{s,e}(s)}{\bar{j}^{Li}(s)} = \frac{1}{a_s F}\left(\frac{R_s}{D_s}\right)\left[\frac{\tanh(\beta)}{\tanh(\beta)-\beta}\right], \tag{6.1}$$

where $\beta = R_s\sqrt{s/D_s}$. Linearization of the Butler-Volmer kinetic relationship (2.12) yields

$$\bar{\eta} = \frac{R_{ct}}{a_s}\bar{j}^{Li} \tag{6.2}$$

with charge transfer resistance, $R_{ct} = RT / [i_0F(\alpha_a+\alpha_c)]$.

Define dimensionless spatial variable $z = x / \delta$, where δ is the electrode thickness, $z = 0$ represents the current collector interface, and $z = 1$ represents the separator interface. The solid phase charge conservation equation (2.6), linearized and expressed as a function of z, is

$$\frac{\sigma^{eff}}{\delta^2}\frac{\partial^2\bar{\phi}_s}{\partial z^2} - \bar{j}^{Li} = 0 \tag{6.3}$$

with boundary conditions

$$-\frac{\sigma^{eff}}{\delta}\frac{\partial\bar{\phi}_s}{\partial z}\bigg|_{z=0} = \frac{\bar{I}}{A} \tag{6.4}$$

$$\frac{\partial\bar{\phi}_s}{\partial z}\bigg|_{z=1} = 0 \tag{6.5}$$

Consistent with assumption (ii), we neglect the 2nd term on the left hand side of electrolyte charge conservation equation (2.9) and assume constant κ^{eff}, yielding

$$\frac{\kappa^{eff}}{\delta^2}\frac{\partial^2\bar{\phi}_e}{\partial z^2} + \bar{j}^{Li} = 0 \tag{6.6}$$

with boundary conditions

$$\frac{\partial\bar{\phi}_e}{\partial z}\bigg|_{z=0} = 0, \tag{6.7}$$

$$\frac{\kappa^{eff}}{\delta}\frac{\partial\bar{\phi}_e}{\partial z}\bigg|_{z=1} = \frac{\bar{I}}{A}. \tag{6.8}$$

We subtract Eqs. (6.6)-(6.8) from Eqs. (6.3)-(6.5) to arrive at a single static ODE for phase potential difference, $\phi_{s-e} = \phi_s - \phi_e$,

$$\frac{\partial^2 \bar{\phi}_{s-e}}{\partial z^2} = \delta^2 \left(\tfrac{1}{\kappa^{eff}} + \tfrac{1}{\sigma^{eff}} \right) \bar{j}^{Li} \tag{6.9}$$

with boundary conditions

$$-\frac{\sigma^{eff}}{\delta} \frac{\partial \bar{\phi}_{s-e}}{\partial z} \bigg|_{z=0} = \frac{\kappa^{eff}}{\delta} \frac{\partial \bar{\phi}_{s-e}}{\partial z} \bigg|_{z=1} = \frac{\bar{I}}{A} . \tag{6.10}$$

Phase potential difference may be expressed as a function of overpotential, and thus reaction rate, as

$$\bar{\phi}_{s-e} = \bar{\eta} - \bar{U} = \frac{R_{ct}}{a_s} \bar{j}^{Li} - \bar{U} \tag{6.11}$$

Express the equilibrium potential impedance using the diffusional impedance transfer function (6.1) to yield

$$\bar{\phi}_{s-e}(s) = \left[\frac{R_{ct}}{a_s} + \frac{\partial U}{\partial c_s} \left(\frac{\bar{c}_{s,e}(s)}{\bar{j}^{Li}(s)} \right) \right] \bar{j}^{Li}(s) , \tag{6.12}$$

valid for small perturbations in $c_{s,e}$ where $\partial U / \partial c_s$ is approximately constant. Combining (6.12) with (6.9) we eliminate $\bar{j}^{Li}$ to obtain an ODE in $\bar{\phi}_{s-e}$

$$\frac{\partial^2 \bar{\phi}_{s-e}(z,s)}{\partial z^2} = \delta^2 \left(\tfrac{1}{\kappa^{eff}} + \tfrac{1}{\sigma^{eff}} \right) \left[\frac{R_{ct}}{a_s} + \frac{\partial U}{\partial c_s} \left(\frac{\bar{c}_{s,e}(s)}{\bar{j}^{Li}(s)} \right) \right]^{-1} \bar{\phi}_{s-e}(z,s) \tag{6.13}$$

with boundary conditions

$$-\frac{\sigma^{eff}}{\delta} \frac{\partial \bar{\phi}_{s-e}(z,s)}{\partial z} \bigg|_{z=0} = \frac{\kappa^{eff}}{\delta} \frac{\partial \bar{\phi}_{s-e}(z,s)}{\partial z} \bigg|_{z=1} = \frac{\bar{I}(s)}{A} . \tag{6.14}$$

Equations (6.13) and (6.14) may now be solved analytically to provide distributed transfer functions for physiochemical variables. Define dimensionless variable ν as

$$\nu(s) = \delta \left(\tfrac{1}{\kappa} + \tfrac{1}{\sigma} \right)^{\frac{1}{2}} \left(\frac{R_{ct}}{a_s} + \frac{\partial U}{\partial c_s} \left(\frac{\bar{c}_{s,e}(s)}{\bar{j}^{Li}(s)} \right) \right)^{-\frac{1}{2}} \tag{6.15}$$

and we have transcendental transfer functions

$$\frac{\bar{\phi}_{s-e}(z,s)}{\bar{I}(s)} = \frac{1}{A} \frac{\delta}{\nu(s) \sinh \nu(s)} \left\{ \tfrac{1}{\sigma^{eff}} \cosh[\nu(s)(z-1)] + \tfrac{1}{\kappa^{eff}} \cosh[\nu(s)(z)] \right\} \tag{6.16}$$

$$\begin{aligned}\frac{\bar{j}^{Li}(z,s)}{\bar{I}(s)} &= \frac{\bar{j}^{Li}(s)}{\bar{\phi}_{s-e}(s)}\frac{\bar{\phi}_{s-e}(z,s)}{\bar{I}(s)} \\ &= \tfrac{1}{\delta A}\tfrac{1}{\kappa^{eff}+\sigma^{eff}}\frac{\nu(s)}{\sinh\nu(s)}\left\{\kappa^{eff}\cosh\left[\nu(s)(z-1)\right]+\sigma^{eff}\cosh\left[\nu(s)(z)\right]\right\}\end{aligned} \tag{6.17}$$

$$\frac{\bar{\eta}(z,s)}{\bar{I}(s)} = \frac{R_{ct}}{a_s}\frac{\bar{j}^{Li}(z,s)}{\bar{I}(s)} \tag{6.18}$$

$$\frac{\Delta\bar{c}_{s,e}(z,s)}{\bar{I}(s)} = \frac{\bar{c}_{s,e}(s)}{\bar{j}^{Li}(s)}\frac{\bar{j}^{Li}(z,s)}{\bar{I}(s)} - \frac{\bar{c}_{s,\mathrm{avg}}(s)}{\bar{I}(s)} \tag{6.19}$$

where, in Eq. (6.19), the bulk electrode solid phase concentration response is

$$\frac{\bar{c}_{s,\mathrm{avg}}(s)}{\bar{I}(s)} = -\frac{1}{\delta A\varepsilon_s F}\frac{1}{s}. \tag{6.20}$$

Equations (6.16)-(6.19) have finite steady state and negative real eigenvalues. By defining solid surface concentrations as the difference $\Delta c_{s,e}(z,t) = c_{s,e}(z,t) - c_{s,\mathrm{avg}}(t)$, we have removed an eigenvalue at the origin from $\bar{c}_{s,e}(z,s)/\bar{I}(s)$. Equations (6.16)-(6.19) are written for the negative electrode. To obtain transfer functions for the positive electrode, multiply by –1. Ong and Newmann [12] present a similar solution to (6.16) including high frequency double layer capacitance dynamics, but neglecting low frequency diffusional impedance. The double layer capacitive effect, relevant on the millisecond time scale, may be included in (6.16)-(6.19) with minor modification of (6.15), necessary only if the desired battery model bandwidth is greater than ~100Hz.

6.1.2 Electrolyte Submodel

The previous section derived analytical transfer functions in a single electrode region. In electrolyte phase conservation equations (2.4) and (2.9), parameters ε_e, κ^{eff}, and D_e^{eff} take on different values in the negative electrode, separator and positive electrode regions making analytical treatment cumbersome. We use the finite element method to obtain spatially discretized transfer matrices with solutions at node points x_i across the 1D domain.

The source term $j^{Li}(x,t)$ in Eqs. (2.4) and (2.9) is approximated as the n_{cell} x 1 vector $\mathbf{j}^{Li}(t)$. The Laplace transform of $\mathbf{j}^{Li}(t)$ is constructed by applying Eq. (6.17) at discrete locations in the negative and positive (with proper sign) electrodes, and setting separator node points to zero

$$\bar{\mathbf{j}}^{Li}(s) = \left[\bar{j}_{-}^{Li}(x_1, s), \ldots, \bar{j}_{-}^{Li}(x_{n_-}, s), 0, \ldots, 0, \bar{j}_{+}^{Li}(x_{n_{cell}-n_+ +1}, s), \ldots, \bar{j}_{+}^{Li}(x_{n_{cell}}, s)\right]^T . \tag{6.21}$$

Finite element discretization of the electrolyte phase diffusion equation (2.4) yields

$$\mathbf{M}_{c_e} \dot{\mathbf{c}}_e(t) = -\mathbf{K}_{c_e} \mathbf{c}_e(t) + \mathbf{F}_{c_e} \mathbf{j}^{Li}(t) \tag{6.22}$$

where $\mathbf{M}_{c_e}$, $\mathbf{K}_{c_e}$, and $\mathbf{F}_{c_e}$ are the mass, stiffness, and forcing matrices, respectively [64]. Laplace transform of (6.22) yields transfer matrix

$$\frac{\bar{\mathbf{c}}_e(s)}{\bar{I}(s)} = (\mathbf{K}_{c_e} + s\mathbf{M}_{c_e})^{-1} \mathbf{F}_{c_e} \frac{\bar{\mathbf{j}}^{Li}(s)}{\bar{I}(s)} . \tag{6.23}$$

Equation (6.23) contains an eigenvalue/zero cancellation at the origin which we eliminate by defining $\Delta c_e(x,t) = c_e(x,t) - c_e(0,t)$. The transfer matrix

$$\frac{\Delta\bar{\mathbf{c}}_e(s)}{\bar{I}(s)} = \frac{\bar{\mathbf{c}}_e(s)}{\bar{I}(s)} - \frac{\bar{c}_e(0,s)}{\bar{I}(s)} \tag{6.24}$$

contains no eigenvalue/zero at the origin. Following reduction, $c_e(x,t)$ is recovered by enforcing charge conservation across the cell to find $c_e(0,t)$,

$$c_e(0,t) = c_{e,0} - \tfrac{1}{L} \int_0^L \Delta c_e(x,t)\, dx . \tag{6.25}$$

The electrolyte phase charge conservation equation (2.9) is linearized to

$$\kappa^{eff} \frac{\partial^2 \phi_e}{\partial x^2} + \frac{\kappa_D^{eff}}{c_{e,0}} \frac{\partial^2 c_e}{\partial x^2} + j^{Li} = 0 \tag{6.26}$$

and spatially discretized to

$$-\mathbf{K}_{\phi_e^I} \boldsymbol{\varphi}_e(t) - \mathbf{K}_{\phi_e^{II}} \mathbf{c}_e(t) + \mathbf{F}_{\phi_e} \mathbf{j}^{Li}(t) = 0 . \tag{6.27}$$

Electrolyte phase potential, having no absolute reference, is given one by defining $\Delta\phi_e(x,t) = \phi_e(x,t) - \phi_e(0,t)$, thus fixing $\Delta\phi_e(0,t) = 0$. We subtract the (1,1) element of $\mathbf{K}_{\phi_e^I}$ in (42) from the first column of all rows of $\mathbf{K}_{\phi_e^I}$,

$$\mathbf{K}_{\Delta\phi_e^I} = \mathbf{K}_{\phi_e^I} - (\mathbf{K}_{\phi_e^I})_{1,1}\begin{bmatrix} 1 & 0 & \cdots & 0 \\ 1 & 0 & & \\ \vdots & & \ddots & \\ 1 & 0 & \cdots & 0 \end{bmatrix}, \tag{6.28}$$

to produce a transfer matrix approximating $\Delta\bar{\phi}_e(x,s)$ at discrete node points x_i,

$$\frac{\Delta\bar{\boldsymbol{\varphi}}_e(s)}{\bar{I}(s)} = (\mathbf{K}_{\Delta\phi_e^I})^{-1}\left(-\mathbf{K}_{\phi_e^{II}}\frac{\Delta\bar{\mathbf{c}}_e(s)}{\bar{I}(s)} + \mathbf{F}_{\phi_e}\frac{\bar{\mathbf{j}}^{Li}(s)}{\bar{I}(s)}\right). \tag{6.29}$$

6.1.3 Current/Voltage Model

Substituting Eq. (2.13) into (2.15), the voltage equation is expanded as

$$V(t) = \phi_e(L,t) - \phi_e(0,t) + \eta(L,t) - \eta(0,t) + U_+(c_{s,e}(L,t)) - U_-(c_{s,e}(0,t)) - \tfrac{R_f}{A} I(t). \tag{6.30}$$

After Laplace transform, the voltage response of the linear impedance model is

$$\frac{\bar{V}(s)}{\bar{I}(s)} = \frac{\bar{V}_{OC}(s)}{\bar{I}(s)} + \frac{\bar{V}_-(s)}{\bar{I}(s)} + \frac{\bar{V}_+(s)}{\bar{I}(s)} + \frac{\bar{V}_e(s)}{\bar{I}(s)} - \tfrac{R_f}{A} \tag{6.31}$$

with individual terms arising due to bulk concentration, or open-circuit voltage dynamics,

$$\frac{\bar{V}_{OC}(s)}{\bar{I}(s)} = \tfrac{\partial U_+}{\partial c_{s+}}\frac{\bar{c}_{s,\text{avg}+}(s)}{\bar{I}(s)} - \tfrac{\partial U_-}{\partial c_{s-}}\frac{\bar{c}_{s,\text{avg}-}(s)}{\bar{I}(s)} = \tfrac{1}{AF}\left[\tfrac{\partial U_+}{\partial c_{s+}}\tfrac{1}{\delta_+\varepsilon_{s+}} - \tfrac{\partial U_-}{\partial c_{s-}}\tfrac{1}{\delta_-\varepsilon_{s-}}\right]\frac{1}{s}, \tag{6.32}$$

negative electrode solid state diffusion dynamics,

$$\frac{\bar{V}_-(s)}{\bar{I}(s)} = -\tfrac{\partial U_-}{\partial c_{s-}}\frac{\Delta\bar{c}_{s,e-}(0,s)}{\bar{I}(s)} - \frac{\bar{\eta}_-(0,s)}{\bar{I}(s)} + \frac{\Delta\bar{\phi}_e^{j_-^{Li}}(L,s)}{\bar{I}(s)}, \tag{6.33}$$

positive electrode solid state diffusion dynamics,

$$\frac{\bar{V}_+(s)}{\bar{I}(s)} = +\tfrac{\partial U_+}{\partial c_{s+}}\frac{\Delta\bar{c}_{s,e+}(0,s)}{\bar{I}(s)} + \frac{\bar{\eta}_+(0,s)}{\bar{I}(s)} + \frac{\Delta\bar{\phi}_e^{j_+^{Li}}(L,s)}{\bar{I}(s)}, \tag{6.34}$$

and electrolyte phase diffusion dynamics,

$$\frac{\bar{V}_e(s)}{\bar{I}(s)} = \frac{\Delta\bar{\phi}_e^{\Delta c_e}(L,s)}{\bar{I}(s)}. \tag{6.35}$$

In defining Eqs. (6.33)-(6.35), we have used superposition to break up Eq. (6.29) into individual components $\Delta\bar{\phi}_e^{j_-^{Li}}$, $\Delta\bar{\phi}_e^{j_+^{Li}}$, and $\Delta\bar{\phi}_e^{\Delta c_e}$, recognizing that each is a static gain on top of $\bar{j}_-^{Li}(x,s)/\bar{I}(s)$, $\bar{j}_+^{Li}(x,s)/\bar{I}(s)$, and $\Delta\bar{c}_e(x,s)/\bar{I}(s)$ dynamics, respectively.

6.2 Reduced Order State Variable Realization

Given full order transfer matrix $\bar{\mathbf{y}}(s)/\bar{u}(s)$ the reduced order transfer matrix is defined as

$$\frac{\bar{\mathbf{y}}^*(s)}{\bar{u}(s)} = \mathbf{z} + \sum_{k=1}^{n} \frac{\mathbf{r}_k \; s}{s-\lambda_k} \tag{6.36}$$

with steady state vector **z** obtained from the full order model as $\mathbf{z} = \lim_{s\to 0} \bar{\mathbf{y}}(s)/\bar{u}(s)$ and eigenvalues λ_k and residue vectors $\mathbf{r}_k$ numerically generated by minimizing the cost function

$$J = \sum_{k=1}^{n_\omega} \sum_{i=1}^{n_x} \left| \operatorname{Re}\left(\bar{\mathbf{y}}_i^*(j\omega_k) - \bar{\mathbf{y}}_i(j\omega_k)\right) \right|^2 + \left| \operatorname{Im}\left(\bar{\mathbf{y}}_i^*(j\omega_k) - \bar{\mathbf{y}}_i(j\omega_k)\right) \right|^2 \tag{6.37}$$

across the frequency range $\omega \in [0, 2\pi f_c]$ where f_c is the model cutoff frequency. Error attributable to model order reduction, $\hat{\bar{y}} = \bar{y}^* - \bar{y}$, is quantified using error norms

$$\begin{aligned} L^2 &= \left[\tfrac{1}{n_\omega} \sum_{k=1}^{n_\omega} \tfrac{1}{L} \int_0^L \left| \hat{\bar{y}}(x, j\omega_k) \right|^2 dx \right]^{\frac{1}{2}}, \\ L^\infty &= \max_{x\in[0,L],\, \omega\in[0,2\pi f_c]} \left| \hat{\bar{y}}(x, j\omega) \right|. \end{aligned} \tag{6.38}$$

The reduced order SIMO state variable model

$$\begin{aligned} \dot{\mathbf{x}} &= \mathbf{A}\mathbf{x} + \mathbf{B}u \\ \mathbf{y}^* &= \mathbf{C}\mathbf{x} + \mathbf{D}u + \mathbf{y}_0 \end{aligned} \tag{6.39}$$

is constructed with

$$\mathbf{A} = diag[\lambda_1 \cdots \lambda_n], \quad \mathbf{B} = [1 \cdots 1]^{\mathrm{T}}, \quad \mathbf{C} = [\mathbf{r}_1\lambda_1 \cdots \mathbf{r}_n\lambda_n], \quad \mathbf{D} = \left[\mathbf{z} + \sum_{k=1}^{n} \mathbf{r}_k \right] \tag{6.40}$$

and static constant $\mathbf{y}_0$ giving output $\mathbf{y}^*$ the proper value at the linearization point. In the following, we drop the * symbol and refer to the reduced order state variable model output as $\mathbf{y}$.

6.3 Linear Models

6.3.1 Submodel Identification

Figure 6.1 compares $\bar{c}_{s,e-}(x,s)/\bar{I}(s)$ frequency response of the exact, infinite dimensional transcendental transfer function (6.19) to a 5th order rational polynomial transfer function approximation (6.36). The approximate transfer function minimizes the cost functional (6.37) in the frequency range $f = \omega/2\pi \in [0, 10\text{ Hz}]$. Note that phase angle of the 5th order model departs from the exact value for $f > 10$ Hz. Lower order models yield visibly poorer results, alternately underpredicting and overpredicting magnitude and phase angle. Following the same procedure, we fit low order models to Eqs. (6.17) and (6.19) (once for each electrode) and Eq. (6.23) at the 50% SOC operating point. Equations (6.18) and (6.29) are calculated as static gains of low order models fit to Eqs. (6.17) and (6.23).

The **A**, **B**, **C**, and **D** matrices of SIMO time domain models are assembled from numerically identified parameters $\mathbf{z}$, λ_k, and $\mathbf{r}_k$ using Eq. (6.40). Figure 6.2 shows distributions of j^{Li}, $c_{s,e}$, and c_e across the cell at various times during a 5C (30 A) discharge from the 50% SOC initial condition. Initial spikes in reaction current, j^{Li}, near the separator decay as Li is de-inserted/inserted from the negative/positive electrode surface. Equilibrium potentials rise/fall most rapidly near the separator penalizing further reaction and over time j^{Li} becomes more uniform. Surface concentrations, $c_{s,e}$, fall/rise in a distributed manner consistent with the time history of reaction, j^{Li}. While discharge continues, $c_{s,e}$ continues to rise/fall, and, unlike $\Delta c_{s,e}$, never reaches steady state due to the electrode bulk concentration free integrator term (6.20). Shown at the bottom of Fig. 6.2, electrolyte concentration, c_e, does approach a steady state distribution due to offsetting source/sink terms, j^{Li}, in the negative/positive electrode regions of Eq. (2.4).

6.3.2 Model Order Selection

Choice of model order is application-dependent. Accurate prediction of electrochemical field variable distributions sometimes requires higher order models than what is necessary to predict current/voltage behavior at the cell boundaries (6.30). Our primary focus in this chapter is to predict voltage response with < 25 mV error.

Transfer functions with similar eigenvalues may be fit simultaneously and forced to share eigenvalues, reducing the number of model states. As a general approach, we create 3 separate reduced order submodels per Eqs. (6.33-35), and force each to share a common set of eigenvalues. We refer to them as the negative electrode submodel, positive electrode submodel, and electrolyte submodel. The open circuit voltage submodel, Eq. (6.32), containing a single eigenvalue at the origin, plays no role in model order reduction.

Table 6.1 displays error metrics of the three submodels for different choices of model order. Tabulated error values are normalized by each transfer function's steady state impedance at the current collector, $x = 0$ or L, listed in parenthesis in the left most column. L^2 and L^∞ norms (6.38) provide information on the quality of fit for 1D field variable distributions, while values listed at $x = 0$ or L quantify submodel error contributions to cell voltage response. At 50% SOC, positive electrode surface concentration represents the dominant impedance due to the strong equilibrium potential coupling, $\partial U_+ / \partial c_{s+}$. Overpotential impedance is almost negligible.

For the present model to achieve < 25 mV cell voltage error at the 50C current rate requires total impedance error $< 8.3 \times 10^{-5}\ \Omega$. Current collector errors listed in Table 6.1 are not strictly additive, however, as individual transfer function errors occur at different frequencies and sometimes cancel one another. For small perturbations about the 50% SOC linearization point, 3rd order electrode models are often sufficient. Sustained high rate currents are more difficult to accurately model and, in particular, to capture electrode surface saturation/depletion nonlinearities at the end of 50C discharge we must use 5th order models for each electrode. Much of the $\phi_e^{\Delta c_e}$ impedance is static and we find a 1st order model of electrolyte dynamics sufficient for the present cell. Except where noted, the $5D_{s-}/5D_{s+}/1D_e$ model is used for all simulations. The eigenvalues are:

$$\lambda_- = -[0.0050, 0.0605, 0.06576, 6.3763, 62.43] \quad \text{rad/s}$$

$$\lambda_- = -[0.0085, 0.0608, 0.05691, 5.8226, 63.69] \quad \text{rad/s}$$

$$\lambda_e = -0.098 \quad \text{rad/s}$$

Including open circuit potential submodel (6.32) with $\lambda_{OC} = 0$, the complete cell model is 12th order.

Before proceeding, we note that lower order SVMs may be obtained by forcing submodels to share eigenvalues. By simultaneously fitting negative and positive electrode transfer functions we may replace eigenvalues λ_- and λ_+ with a single set of eigenvalues, $\lambda_\pm$. This order reduction is achieved at the expense of increased impedance error quantified in Table 6.2.

6.3.3 Current/Voltage Model

The current/voltage model is a state variable realization of Eq. (6.31), with reduced order submodels identified as described in Sec. 6.3.1 and Sec. 6.3.2. Unlike the transfer function (6.31), the SVM may take on non-zero initial conditions for $c_{s,\mathrm{avg}-}$ and $c_{s,\mathrm{avg}+}$. Following typical convention, we define SOC as the fraction of capacity, Q, stored in the cell. Given an initial SOC at $t = 0$ and assuming 100% coulombic efficiency, SOC may be calculated in time as

$$SOC(t) = -\frac{1}{Q}\int_0^t I(t)dt\,. \tag{6.41}$$

We express $c_{s,\mathrm{avg}-} = f(SOC)$ and $c_{s,\mathrm{avg}+} = f(SOC)$ by defining a reference stoichiometry, $\theta = c_{s,\mathrm{avg}} / c_{s,\max}$, for each electrode at the 100% SOC condition, $\theta_{100\%}$, listed in Table 3.1. The 0% SOC reference stoichiometry, $\theta_{0\%}$, is calculated by subtracting $Q = 7.19$ Ah from $\theta_{100\%}$ with appropriate units conversion,

$$\theta_{0\%} = \theta_{100\%} - Q\left(\tfrac{1}{AF}\tfrac{1}{\delta\varepsilon_s}\tfrac{1}{c_{s,\max}}\right). \tag{6.42}$$

With reference stoichiometries, we may express each electrode's bulk concentration as a linear function of SOC,

$$c_{s,\mathrm{avg}}(t) = \left[SOC(t)\left(\theta_{100\%} - \theta_{0\%}\right) + \theta_{0\%}\right]c_{s,\max}\,, \tag{6.43}$$

valid at any point in time.

Linearized about 50% SOC, the linear current/voltage SVM is

$$\frac{d}{dt}\begin{bmatrix} SOC \\ \mathbf{x}_- \\ \mathbf{x}_+ \\ \mathbf{x}_e \end{bmatrix} = \begin{bmatrix} 0 & & & \\ & \mathbf{A}_- & & \\ & & \mathbf{A}_+ & \\ & & & \mathbf{A}_e \end{bmatrix} \begin{bmatrix} SOC \\ \mathbf{x}_- \\ \mathbf{x}_+ \\ \mathbf{x}_e \end{bmatrix} + \begin{bmatrix} -\frac{1}{Q} \\ 1 \\ \vdots \\ 1 \end{bmatrix} I(t)$$

$$V(t) = \begin{bmatrix} \frac{\partial V_{OC}}{\partial SOC} & \mathbf{C}_- & \mathbf{C}_+ & \mathbf{C}_e \end{bmatrix} \begin{bmatrix} SOC \\ \mathbf{x}_- \\ \mathbf{x}_+ \\ \mathbf{x}_e \end{bmatrix} + \begin{bmatrix} \mathbf{D}_- + \mathbf{D}_+ + \mathbf{D}_e - \frac{R_f}{A} \end{bmatrix} I(t) + V_{\text{static}} \tag{6.44}$$

where

$$\begin{aligned} \mathbf{C}_- &= \mathbf{C}^{\Delta c_{s,e-}} + \mathbf{C}^{\eta_-} + \mathbf{C}^{\Delta\phi_e^{j_-^{Li}}} & \mathbf{D}_- &= \mathbf{D}^{\Delta c_{s,e-}} + \mathbf{D}^{\eta_-} + \mathbf{D}^{\Delta\phi_e^{j_-^{Li}}} \\ \mathbf{C}_+ &= \mathbf{C}^{\Delta c_{s,e+}} + \mathbf{C}^{\eta_+} + \mathbf{C}^{\Delta\phi_e^{j_+^{Li}}} & \mathbf{D}_+ &= \mathbf{D}^{\Delta c_{s,e+}} + \mathbf{D}^{\eta_+} + \mathbf{D}^{\Delta\phi_e^{j_+^{Li}}} \\ \mathbf{C}_e &= \mathbf{C}^{\Delta\phi_e^{\Delta c_e}} & \mathbf{D}_e &= \mathbf{D}^{\Delta\phi_e^{\Delta c_e}} \end{aligned} \tag{6.45}$$

$$\frac{\partial V_{OC}}{\partial SOC} = \frac{Q}{AF}\left(\left.\frac{\partial U_+}{\partial c_{s+}}\right|_{50\%} \frac{1}{\delta_+ \varepsilon_{s+}} - \left.\frac{\partial U_-}{\partial c_{s-}}\right|_{50\%} \frac{1}{\delta_- \varepsilon_{s-}} \right) \tag{6.46}$$

$$\left.V_{\text{static}}\right|_{50\%} = \left.U_+\right|_{50\%} - \left.U_-\right|_{50\%} - \left.\frac{\partial V_{OC}}{\partial SOC}\right|_{50\%} . \tag{6.47}$$

Figure 6.3 compares voltage response of the $5D_{s-}/5D_{s+}/1D_e$ linear SVM to the nonlinear CFD model for a stepped current profile at the 50% SOC initial condition. The current profile, serving as input to both models, consists of 10C, 20C, 30C, and 40C discharge/charge/rest cycles. Each discharge/charge cycle returns the cell to 50% SOC. Voltage prediction for the linear SVM is reasonably good, although we see from Fig. 6.3d that individual submodel errors cancel one another throughout much of the profile. Submodel errors worsen with increasing current rate as electrode surface concentrations are perturbed far from the 50% SOC linearization point.

6.3.4 Observability and Controllability Properties

Using standard techniques [23], we assemble observability

$$\vartheta_o = [\mathbf{C}^T \ (\mathbf{CA})^T \ (\mathbf{CA}^2)^T \ \ldots (\mathbf{CA}^{n-1})^T]^T \tag{6.48}$$

and controllability

$$\vartheta_c = [\mathbf{A} \quad \mathbf{AB} \quad \mathbf{A}^2\mathbf{B} \quad \ldots \quad \mathbf{A}^{n-1}\mathbf{B}] \tag{6.49}$$

matrices. Both have full rank, indicating that the model is fully observable and controllable.

Some model states may be less observable/controllable than others, however, which we quantify using the observability/controllability gramian of a balanced realization model. We define observability gramian, $\mathbf{W}_o$, as the solution to

$$\mathbf{A}^T\mathbf{W}_o + \mathbf{W}_o\mathbf{A} + \mathbf{C}^T\mathbf{C} = 0 \tag{6.50}$$

and controllability gramian, $\mathbf{W}_c$, as the solution to

$$\mathbf{A}\mathbf{W}_c + \mathbf{W}_c\mathbf{A}^T + \mathbf{B}\mathbf{B}^T = 0\,. \tag{6.51}$$

Applying transformation $\overline{\mathbf{x}} = \mathbf{T}\,\mathbf{x}$, an alternative realization of the SVM is

$$\begin{aligned} \dot{\overline{\mathbf{x}}} &= \mathbf{T}\mathbf{A}\mathbf{T}^{-1}\,\overline{\mathbf{x}} + \mathbf{T}\mathbf{B}\,u \\ y &= \mathbf{C}\mathbf{T}^{-1}\,\overline{\mathbf{x}} + \mathbf{D}u \end{aligned} \tag{6.52}$$

with observability and controllability gramians, $\overline{\mathbf{W}}_o = \mathbf{T}^{-T}\mathbf{W}_o\mathbf{T}^{-1}$ and $\overline{\mathbf{W}}_c = \mathbf{T}\mathbf{W}_c\mathbf{T}^T$, respectively. The balanced realization of (6.52) results when transform matrix $\mathbf{T}$ is such that $\overline{\mathbf{W}}_o = \overline{\mathbf{W}}_c = diag(\mathbf{g})$.

Table 6.3 presents the observability/controllability gramian of the balanced realization $5D_{s-}/5D_{s+}/1D_e$ linear SVM. Fast electrode states are most observable/ controllable. This is intuitive, as the rapid perturbations in electrode surface concentration (of which voltage response is a strong function) are predominantly influenced by recent current history. In contrast, electrode bulk concentrations (*i.e.* SOC) rise and fall slowly and are weakly coupled to voltage response. For estimation/control schemes in fast dynamic applications, it may be possible to reduce order by dropping slow electrode states with weak observability/ controllabity. The electrolyte submodel state is also weakly observable/ controllable, indicating that it will probably be difficult to ascertain electrolyte concentration gradients using a linear observer. Nonetheless, the results are encouraging. To date, the battery estimation literature has predominantly focused on SOC estimation. In high power, pulse-type applications however, it is attractive to estimate electrode surface concentrations, as their saturation/depletion are responsible for sudden loss of power and side reactions. Table 6.3 indicates that electrode surface concentrations are more controllable/ observable than SOC.

6.4 Nonlinear Models

Concentration dependent properties represent the dominant nonlinearities in Eqs. (2.1-15). Those appearing explicitly in the output equation of (6.44) are readily included in the SVM. Other nonlinearities exhibit complex spatial dependency which, for the electrode submodels, we approximate on a lumped, electrode-averaged basis.

6.4.1 Open Circuit Potential

The open circuit potential (OCP) nonlinearity is incorporated by introducing equilibrium potential relationships, $U_+(c_{s,e}(L,t))$ and $U_-(c_{s,e}(0,t))$ listed in Table 3.1, into the model output equation. The SVM (6.44) is modified with

$$\tfrac{\partial V_{OC}}{\partial SOC} = \tfrac{\partial V_{OC}}{\partial SOC}\left(c_{s,e}(L,t), c_{s,e}(0,t)\right) \tag{6.53}$$

and

$$V_{\text{static}} = V_{\text{static}}\left(c_{s,e}(L,t), c_{s,e}(0,t)\right) \tag{6.54}$$

now expressed as nonlinear functions, rather than constants (6.46-47). The nonlinear SVM takes the form

$$\begin{aligned} \dot{\mathbf{x}} &= \mathbf{A}\,\mathbf{x} + \mathbf{B}\,I \\ V &= h(\mathbf{x}, I) \end{aligned} \tag{6.55}$$

Unlike the linear SVM, the nonlinear OCP SVM correctly predicts battery rest voltage, or open circuit voltage (OCV) at all values of SOC. Dynamic response is still lacking, however.

Figure 6.4 shows voltage response for constant current (1C to 50C) discharge simulations initiated from 0% depth of discharge (DOD), i.e. 100% SOC, as predicted by the CFD model, linear SVM (6.44) and nonlinear OCP SVM. At low current rates, the linear SVM gives reasonable approximation only in the middle of the discharge as surface concentrations $c_{s,e}(0,t)$ and $c_{s,e}(L,t)$ pass through their 50% SOC linearization point. The nonlinear OCP SVM greatly improves voltage prediction over the linear model at beginning of discharge, near 100% SOC. End of discharge voltage prediction is poor, however, for all but the lowest rate, 1C case.

6.4.2 Electrode Surface Concentration

End of discharge voltage may be substantially improved by interpolating between local linear models identified at various electrode surface concentration set points. Voltage response predicted by the nonlinear OCP/$c_{s,e}$ SVM, shown in Fig. 6.4 with the "·" symbol, lays almost directly on top of CFD model results. The nonlinear OCP/$c_{s,e}$ SVM also utilizes Eqs. (6.53)-(6.54) but, unlike Sec. 4.2.1, $c_{s,e}(0,t)$ and $c_{s,e}(L,t)$ are approximated by nonlinear, rather than linear models.

Shown in Fig 6.5, local electrode submodels are identified at roughly 20% increments in surface stoichiometry, with finer discretization in less linear regions of $U_+(c_{s,e})$ and $U_-(c_{s,e})$. There is negligible advantage in allowing each localized electrode submodel its own independent eigenvalues. We obtain good impedance fits at all set points utilizing the eigenvalues identified at 50% SOC. **A** and **B** matrices of (6.44) thus remain constant. The **C** and **D** matrices vary by interpolating between locally-identified electrode submodels as a function of solid phase surface concentration averaged across each electrode,

$$\begin{aligned} \mathbf{C}_- &= \mathbf{C}_-(c_{s,e\,\text{avg-}}) \qquad \mathbf{D}_- = \mathbf{D}_-(c_{s,e\,\text{avg-}}) \\ \mathbf{C}_+ &= \mathbf{C}_+(c_{s,e\,\text{avg+}}) \qquad \mathbf{D}_+ = \mathbf{D}_+(c_{s,e\,\text{avg+}}) \end{aligned} \tag{6.56}$$

The nonlinear OCP/$c_{s,e}$ SVM keeps the form of Eq. (6.55).

Figure 6.6 elucidates the substantial improvement in end of discharge voltage prediction at the 50C rate (Fig. 6.4) achieved by approximating $c_{s,e}$ nonlinearities. Comparing surface concentrations predicted by the CFD model, linear model and nonlinear $c_{s,e}$ model, there is little difference between the three in the positive electrode. In the negative electrode however, the relatively flat U_- relationship at moderate-to-high surface stoichiometries causes reaction to be heavily favored near the separator at short times. At t = 6 sec, the CFD model shows surface concentrations drastically different from the linear model. Around this time, local values of $c_{s,e-}$ fall below ~$0.2c_{s,\max}$ causing U_- to sharply rise (Fig. 6.5). At t = 13 sec, surface concentrations are near uniformly depleted across the negative electrode, a condition accurately captured by the nonlinear $c_{s,e}$ model. The linear model, predicting local concentrations less than zero, is physically unrealistic.

Figure 6.7 displays cell voltage error and submodel voltage error for the nonlinear OCP/$c_{s,e}$ SVM during the same 50C discharge from 100% SOC. Equilibrium potentials at the current collectors, $U_+(c_{s,e}(L,t))$ and $U_-(c_{s,e}(0,t))$, are predicted to within 25 mV. Electrolyte phase potential error continually grows throughout the discharge, however, as a large electrolyte concentration gradient builds across the cell. Non-uniform $c_e(x,t)$ increases the significance of the electrolyte conductivity concentration dependence, $\kappa^{eff}(c_e)$.

Figure 6.8 displays voltage errors for the nonlinear OCP/$c_{s,e}$ SVM in simulating the 50% SOC pulse current profile from Fig. 6.3. Here, the cell is alternately discharged and charged by short pulses, no substantial electrolyte concentration gradient is established and electrolyte phase potential error is negligible. Rapid reversals in current cause brief spikes in cell voltage error > 25 mV at 40, 65, and 80 seconds which quickly dissipate. Individual submodel errors are now all < 25 mV, a large improvement over the linear SVM results shown in Fig. 6.3.

6.4.3 Electrolyte Concentration

The impedance model assumption of $j^{Li}(x,t)$ decoupled from $c_e(x,t)$ loses validity as $c_e \rightarrow 0$, a condition which we explore here. With $j^{Li}(x,t)$ and $c_e(x,t)$ provided by our linear model it is possible to explicitly solve for $\phi_e(L,t)$ by twice integrating Eq. (2.9),

$$\Delta\phi_e(L,t) = \tfrac{2RT(t_+^o-1)}{F}\ln\left(\frac{c_e(0,t)}{c_e(L,t)}\right) - \int_0^L \frac{1}{\kappa^{eff}(c_e(x,t))}\int j^{Li}(x,t)\,dx\;\;dx\,, \tag{6.57}$$

valid for constant t_+^o and $f_\pm$. (See [49] for discussion of non-constant t_+^o and $f_\pm$.) For brevity, we refer to term 1 on the right hand side of (6.57) as the $\ln(c_e)$ nonlinearity and term 2 as the $\kappa^{eff}(c_e)$ nonlinearity. Each is a modification of the output equation of (6.44) with nonlinear SVM realization (6.55).

The present cell model with parameters listed in Table 3.1 does not experience electrolyte depletion at any current rate, however other cells with less porous electrodes and/or separator may experience this limitation. To examine voltage response with end of discharge induced by electrolyte depletion, we reduce the electrolyte diffusion coefficient by one order of magnitude to $D_e = 2.6 \times 10^{-7}$ cm^2/s.

Figure 6.9 presents the voltage response of this electrolyte transport-limited cell for 10-50C constant current discharge cases initiated from 100% SOC. Rate capability is substantially reduced compared to the nominal D_e model (Fig. 6.4). Figure 6.9 shows the nonlinear OCP/$c_{s,e}$ SVM (Sec. 6.4.2) overpredicts voltage and fails to capture end of discharge caused by electrolyte depletion. Introduction of the $\kappa^{eff}(c_e)$ nonlinearity slightly improves voltage prediction at intermediate times, however end of discharge prediction remains poor. Voltage prediction degrades when the $\ln(c_e)$ nonlinearity is included as it is very sensitive to small errors in absolute (not relative) values of $c_e(0,t)$ and $c_e(L,t)$

To elucidate these errors, Fig. 6.10 shows electrolyte concentration distributions at various times during the 30C discharge case. During discharge of a cell with sluggish electrolyte transport, electrolyte depletion occurs first at $x = L$ and then spreads back across the positive electrode. Early in the discharge, the linear model predicts $c_e(x,t)$ to good accuracy, however around $t = 15$ seconds (corresponding to ~10% DOD in Fig. 6.9), the linear model begins to substantially underpredict $c_e(L,t)$. By $t = 18.7$ seconds, the linear model predicts negative values of c_e which are physically impossible. Extending the SVM to capture electrolyte depletion may require online PDE solution, as nonlinearities governing j^{Li} distribution are highly spatially dependent and do not appear conducive to a lumping. But provided local values of c_e remain above $0.15c_{e,0}$, the present impedance model assumptions are valid and the nonlinear OCP/$c_{s,e}$/$\kappa^{eff}(c_e)$ SVM predicts voltage response to within 25 mV regardless of sluggish or facile D_e.

6.5. Conclusions

This chapter numerically derives a fully observable/ controllable state variable model from an impedance representation of electrochemical kinetic, species and charge conservation equations governing discharge/charge behavior of a Li-ion cell. Validated against a 313th order nonlinear CFD model of a 6 Ah HEV cell, a 12th order state variable model, with 0 to 10 Hz bandwidth, predicts terminal voltage to within 1% for pulse and constant current profiles at rates up to 50C. Model properties indicate that electrode surface concentrations (with fast dynamics related to sudden loss of power and side reactions) are more observable/controllable than electrode bulk concentrations (SOC).

The state equation has modal form with negative real eigenvalues distributed in frequency between the slowest system eigenvalue (negative electrode solid state diffusion) and 10 Hz. A single eigenvalue at the origin represents SOC dynamics. The model order reduction procedure is somewhat insensitive to numerical eigenvalue location (given the thousands of actual system eigenvalues) and we can approximate the range of admissible electrode surface concentrations using local linear models sharing a single set of eigenvalues. Open circuit potential, electrode surface concentration/reaction distribution coupling, and electrolyte concentration/ionic conductivity nonlinearities are explicitly approximated in the model output equation on a local, electrode-averaged, and distributed basis, respectively.

This chapter (particularly the sluggish electrolyte diffusion case explored in Sec. 6.4.3) highlights challenges associated with control-oriented modeling of infinite dimensional nonlinear distributed parameters systems. We quantify error attributable to rational approximation of infinite dimensional processes in the frequency domain using impedance error norms. Errors attributable to model assumptions and lumped approximation of spatially varying nonlinearities are quantified in the time domain using the CFD model. By inducing sluggish electrolyte transport, we show the present model loses validity near electrolyte depletion ($c_e < 0.15 c_{e,0}$) where the system exhibits strong spatially varying nonlinearities.

Transfer Function (steady state impedance)	**Error**	**Negative Electrode Submodel Order**		
		3	**4**	**5**
$\left\|\left(\frac{\partial U_-}{\partial c_{s-}}\right)\Delta\bar{c}_{s,e-}(x,j\omega)/\bar{I}(j\omega)\right\|$ (3.65 x 10^{-4} Ω @ x=0, ω=0)	$x = 0$	0.1215	0.0689	0.0387
	L^∞	0.1440	0.0711	0.0453
	L^2	0.0672	0.0319	0.0175
$\left\|\bar{\eta}_-(x,j\omega)/\bar{I}(j\omega)\right\|$ (7.85 x 10^{-6} Ω @ x=0, ω=0)	$x = 0$	0.0674	0.0283	0.0159
	L^∞	0.2636	0.1030	0.0391
	L^2	0.0558	0.0227	0.0103
$\left\|\Delta\bar{\phi}_e^{j_-^{Li}}(x,j\omega)/\bar{I}(j\omega)\right\|$ (2.44 x 10^{-4} Ω @ x=L, ω=0)	$x = L$	0.0473	0.0236	0.0111
	L^∞	0.0566	0.0281	0.0132
	L^2	0.0304	0.0129	0.0063
		Positive Electrode Submodel Order		
		3	**4**	**5**
$\left\|\left(\frac{\partial U_+}{\partial c_{s+}}\right)\Delta\bar{c}_{s,e+}(x,j\omega)/\bar{I}(j\omega)\right\|$ (2.50 x 10^{-3} Ω @ x=0, ω=0)	$x = L$	0.1203	0.0353	0.0089
	L^∞	0.1213	0.0354	0.0095
	L^2	0.0526	0.0165	0.0053
$\left\|\bar{\eta}_+(x,j\omega)/\bar{I}(j\omega)\right\|$ (1.45 x 10^{-5} Ω @ x=0, ω=0)	$x = L$	0.0668	0.0424	0.0219
	L^∞	0.2597	0.1165	0.0724
	L^2	0.0378	0.0217	0.0108
$\left\|\Delta\bar{\phi}_e^{j_+^{Li}}(x,j\omega)/\bar{I}(j\omega)\right\|$ (2.42 x 10^{-4} Ω @ x=L, ω=0)	$x = L$	0.0227	0.0141	0.0077
	L^∞	0.0227	0.0141	0.0077
	L^2	0.0049	0.0029	0.0014
		Electrolyte Submodel Order		
		1	**2**	**3**
$\left\|\Delta\bar{\phi}_e^{\Delta c_e}(x,j\omega)/\bar{I}(j\omega)\right\|$ (2.13 x 10^{-4} Ω @ x=L, ω=0)	$x = L$	0.0555	0.0447	0.0365
	L^∞	0.1123	0.0944	0.0407
	L^2	0.0318	0.0255	0.0155

Table 6.1. Impedance error magnitude for negative electrode, positive electrode, and electrolyte submodels of various orders across frequency range $0 \le f \le 10$ Hz. Local error quantified at the current collector appropriate for the given submodel, either $x = 0$ or $x = L$. Distributed error quantified with L^∞ and L^2 error norms. All errors normalized by steady state impedance at the current collector.

Transfer Function (steady state impedance)	**Error**	**Negative/Positive Electrode Submodel Order**		
		3	**4**	**5**
$\left\|\left(\frac{\partial U_-}{\partial c_{s-}}\right)\Delta\bar{c}_{s,e-}(x,j\omega)/\bar{I}(j\omega)\right\|$ (3.65 x 10^{-4} Ω @ x=0, ω=0)	$x = 0$	0.2330	0.1410	0.1089
	L^∞	0.2425	0.1529	0.1199
	L^2	0.1005	0.0581	0.0453
$\left\|\bar{\eta}_-(x,j\omega)/\bar{I}(j\omega)\right\|$ (7.85 x 10^{-6} Ω @ x=0, ω=0)	$x = 0$	0.0559	0.0273	0.0161
	L^∞	0.2485	0.1043	0.0421
	L^2	0.0495	0.0227	0.0111
$\left\|\Delta\bar{\phi}_e^{j_-^{Li}}(x,j\omega)/\bar{I}(j\omega)\right\|$ (2.44 x 10^{-4} Ω @ x=L, ω=0)	$x = L$	0.0389	0.0229	0.0112
	L^∞	0.0478	0.0276	0.0132
	L^2	0.0261	0.0128	0.0067
$\left\|\left(\frac{\partial U_+}{\partial c_{s+}}\right)\Delta\bar{c}_{s,e+}(x,j\omega)/\bar{I}(j\omega)\right\|$ (2.50 x 10^{-3} Ω @ x=0, ω=0)	$x = L$	0.1086	0.0787	0.0534
	L^∞	0.1086	0.0803	0.0534
	L^2	0.0481	0.0327	0.0219
$\left\|\bar{\eta}_+(x,j\omega)/\bar{I}(j\omega)\right\|$ (1.45 x 10^{-5} Ω @ x=0, ω=0)	$x = L$	0.0744	0.0417	0.0198
	L^∞	0.2078	0.1139	0.0675
	L^2	0.0411	0.0212	0.0099
$\left\|\Delta\bar{\phi}_e^{j_+^{Li}}(x,j\omega)/\bar{I}(j\omega)\right\|$ (2.42 x 10^{-4} Ω @ x=L, ω=0)	$x = L$	0.0252	0.0137	0.0070
	L^∞	0.0252	0.0137	0.0070
	L^2	0.0054	0.0028	0.0013

Table 6.2. Impedance error magnitude for combined negative electrode/ positive electrode submodels (with common eigenvalues) of various orders across frequency range $0 \leq f \leq$ 10 Hz. Local error quantified at the current collector appropriate for the given submodel, either $x = 0$ or $x = L$. Distributed error quantified with L^∞ and L^2 error norms. All errors normalized by steady state impedance at the current collector.

	Eigenvalue, λ_k [rad/s]	**Gramian**, g_k [$(\Omega\ \mathrm{s})^{1/2}$]
Negative Electrode Submodel (5th Order)	-5.56×10^{-3}	4.33×10^{-8}
	-6.05×10^{-2}	4.39×10^{-12}
	-6.58×10^{-1}	6.31×10^{-6}
	-6.38	4.34×10^{-5}
	-62.4	1.146×10^{-4}
Positive Electrode Submodel (5th Order)	-8.53×10^{-3}	2.07×10^{-6}
	-6.08×10^{-2}	2.16×10^{-10}
	-5.69×10^{-1}	2.98×10^{-6}
	-5.82	1.400×10^{-5}
	-63.7	7.42×10^{-4}
Electrolyte Submodel (1st Order)	-9.49×10^{-1}	7.54×10^{-9}

Table 6.3. Observability/controllability gramian of balanced realization $5D_{s-}/5D_{s+}/1D_e$ SVM linearized at 50% SOC.

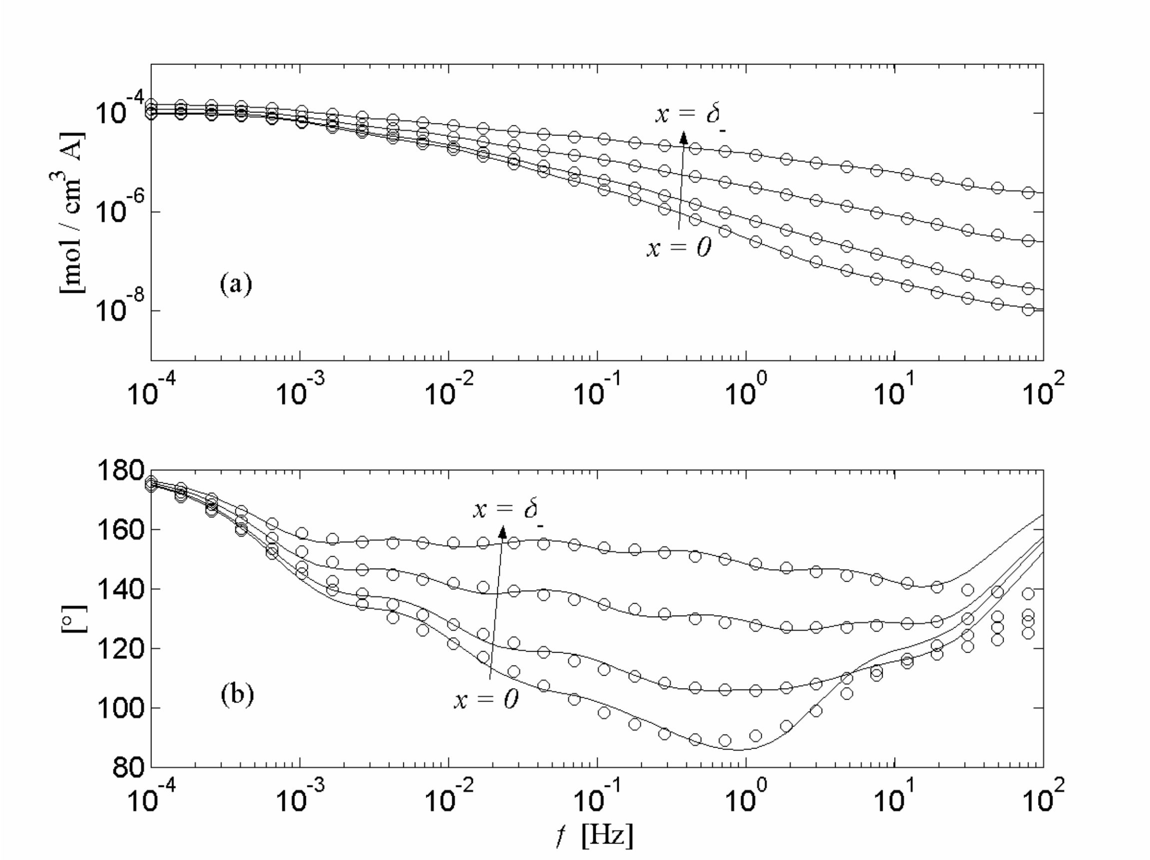

Figure 6.1. Negative electrode surface concentration frequency response: Exact transfer function (○) and 5th order polynomial transfer function (−). (a) Magnitude, $\left|\Delta\bar{c}_{s,e-}(x,s)/\bar{I}(s)\right|$. (b) Phase angle, $\angle(\Delta\bar{c}_{s,e-}(x,s)/\bar{I}(s))$.

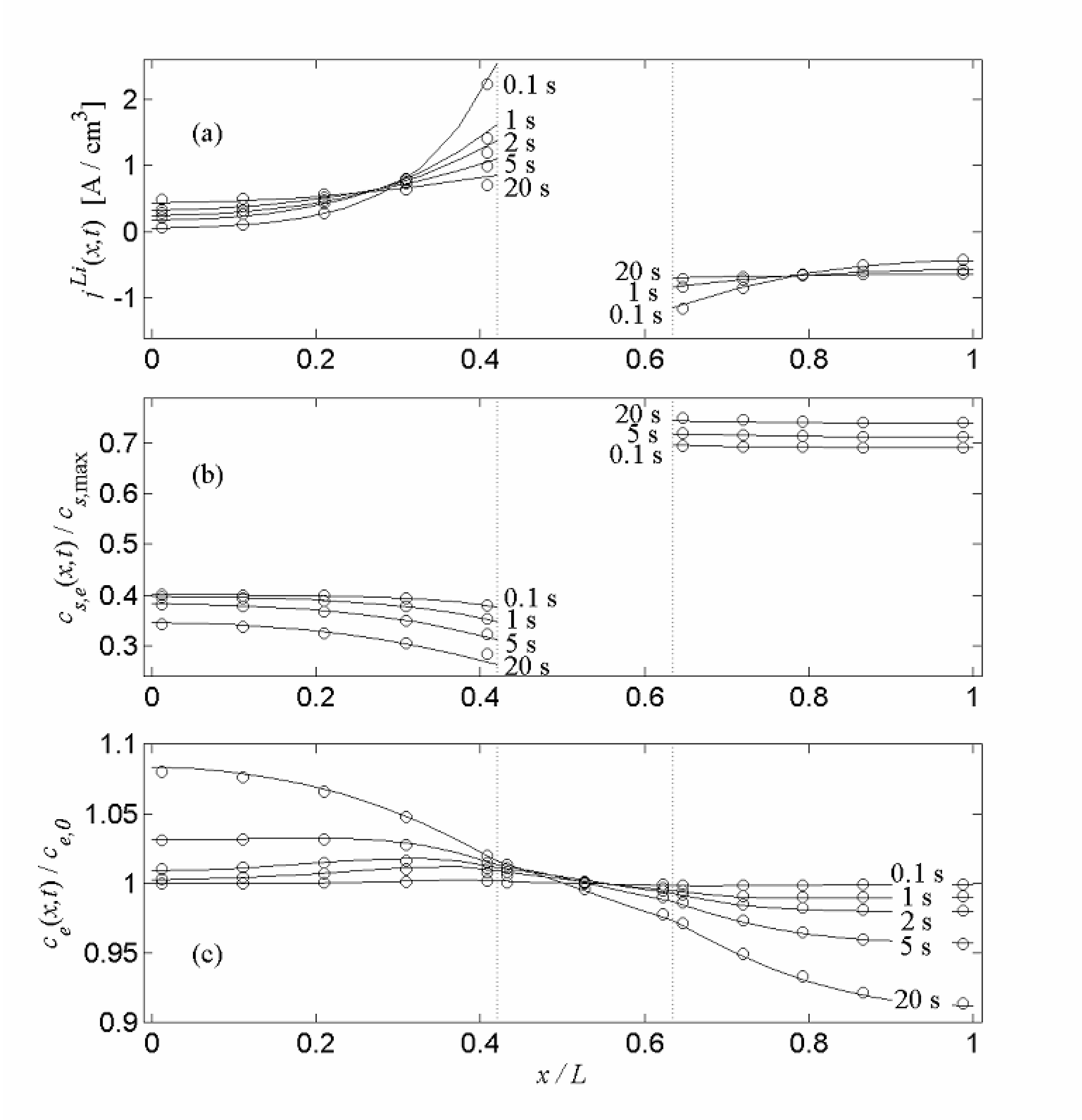

Figure 6.2. Reaction and concentration distributions during 5C discharge from 50% SOC initial condition: CFD model (○) and 5th order negative electrode/ 5th order positive electrode/ 3rd order electrolyte linear submodels (−). (a) Reaction current density. (b) Electrode surface concentration. (c) Electrolyte concentration.

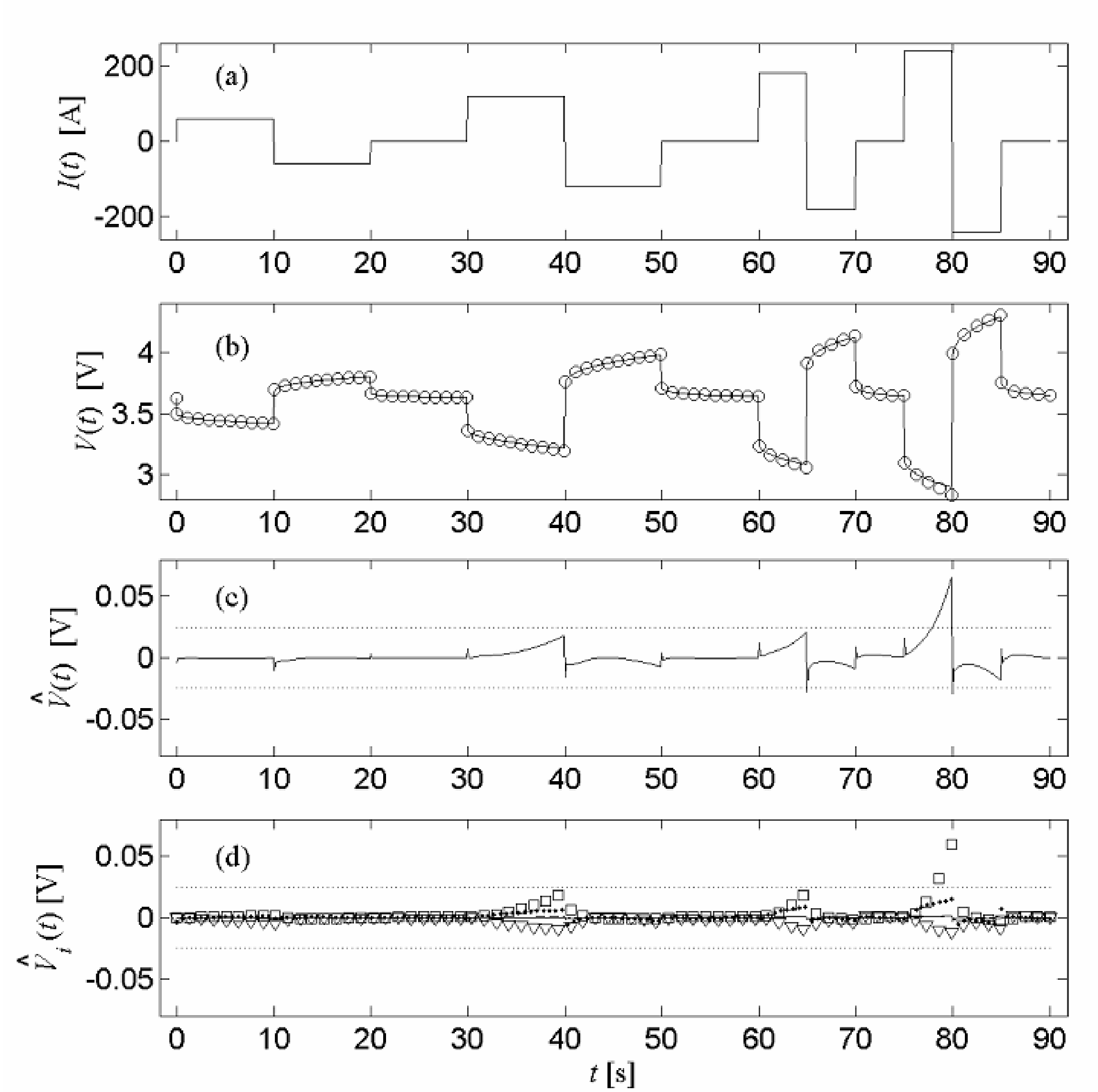

Figure 6.3. Linear SVM voltage response and error for pulse current profile at 50% SOC. (a) Current profile. (b) Voltage response of CFD model (○) and linear SVM (-). (c) Voltage response error of linear SVM (-) with 25 mV error threshold (···). (d) Individual submodel contributions to voltage error: $\hat{\eta}_{-}(0,t)$ (-), $\hat{\eta}_{+}(L,t)$ (--), $\hat{U}_{-}(0,t)$ (□), $\hat{U}_{+}(L,t)$ (▽), $\Delta\hat{\phi}_{e}(L,t)$ (•), with 25 mV error threshold (···).

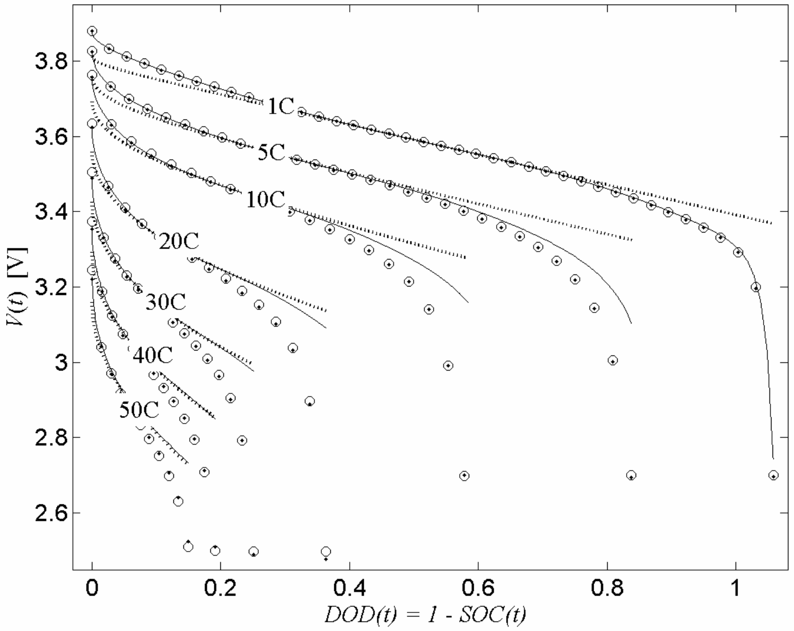

Figure 6.4. Voltage response of various SVMs versus CFD model during constant current discharge from 100% SOC initial condition: CFD model (○), linear SVM (···), nonlinear OCP SVM (-), and nonlinear OCP/$c_{s,e}$ SVM (•).

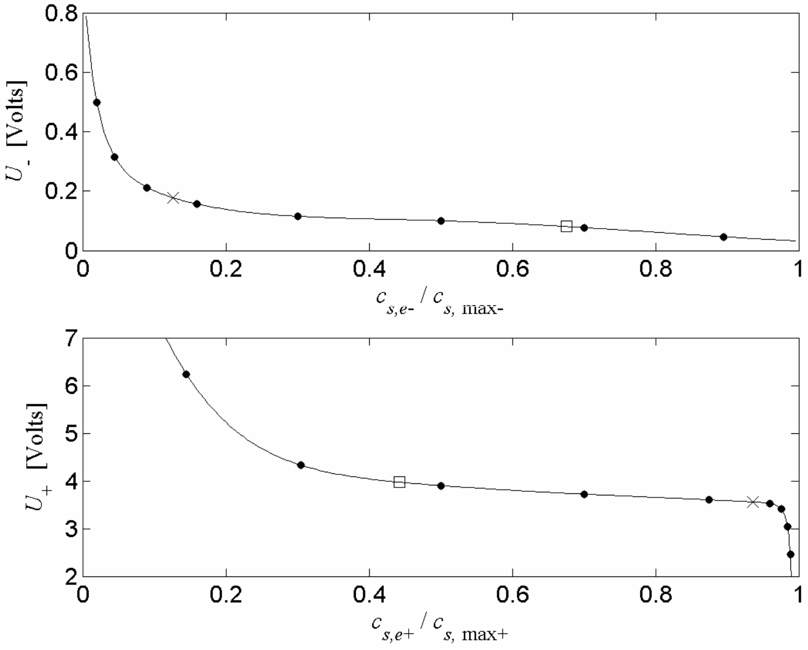

Figure 6.5. Equilibrium (or open-circuit) potential versus electrode surface concentration: Empirical relationships, *U*, from Table 1 (-), linearization setpoints used for nonlinear $c_{s,e}$ SVM submodel identification (•), 100% SOC reference (□) and 0% SOC reference (x).

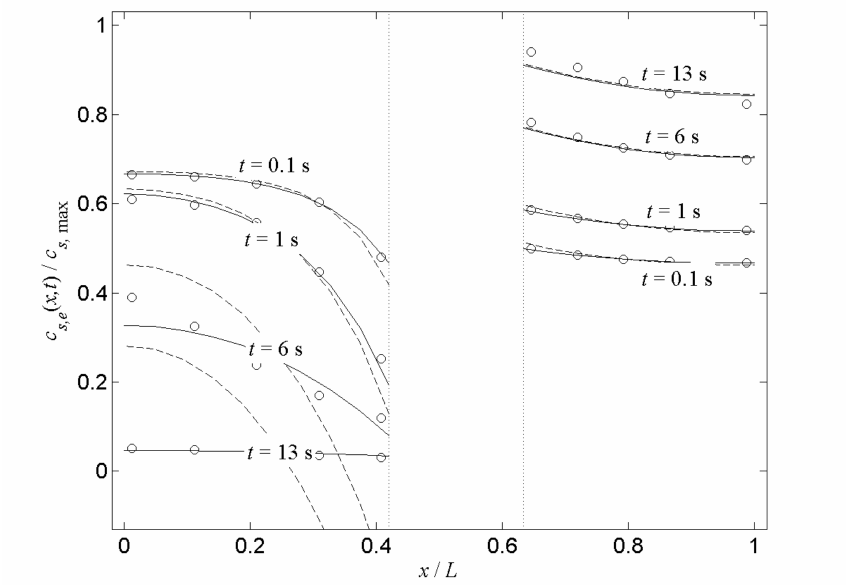

Figure 6.6. Distribution of electrode surface concentration at various times during 50C discharge from 100% SOC initial condition (voltage response shown in Fig. 5): CFD model (○), linear SVM (--), and nonlinear $c_{s,e}$ SVM (-).

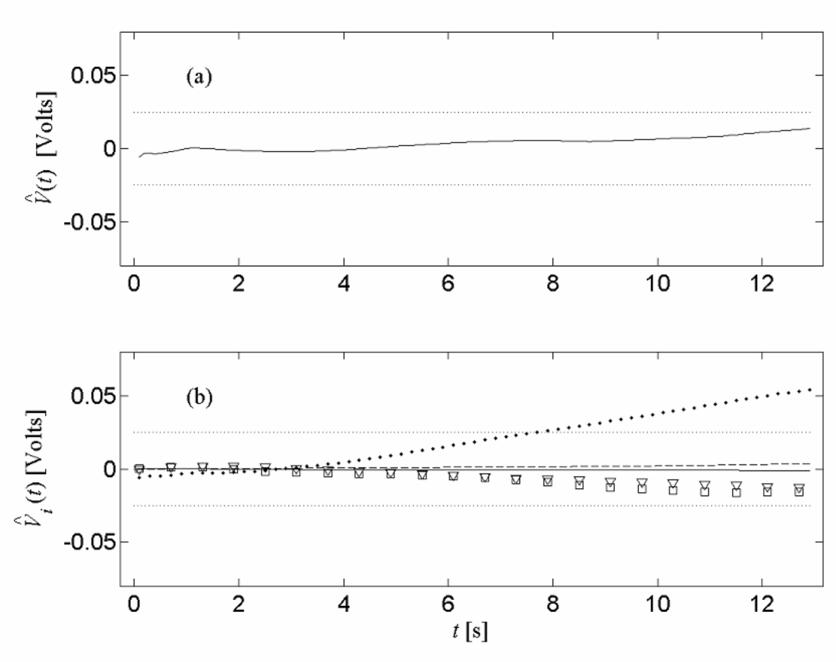

Figure 6.7. Nonlinear OCP/ $c_{s,e}$ SVM error during 50C discharge from 100% SOC initial condition (voltage response shown in Fig. 5): (a) Voltage response error (-) with 25 mV error threshold (···). (b) Individual submodel contributions to voltage error: $\hat{\eta}_-(0,t)$ (-), $\hat{\eta}_+(L,t)$ (--), $\hat{U}_-(0,t)$ (□), $\hat{U}_+(L,t)$ (▽), $\Delta\hat{\phi}_e(L,t)$ (•), with 25 mV error threshold (···).

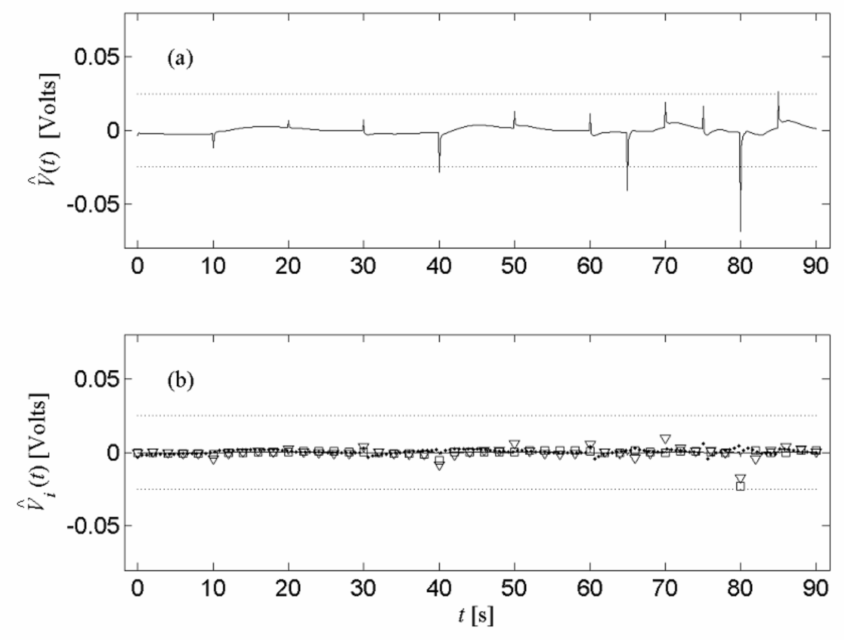

Figure 6.8. Nonlinear OCP/ $c_{s,e}$ SVM error during pulse current profile at 50% SOC (current profile and CFD model voltage response shown in Figs. 4a and 4b): (a) Voltage response error (-) with 25 mV error threshold (···). (b) Individual submodel contributions to voltage error: $\hat{\eta}_-(0,t)$ (-), $\hat{\eta}_+(L,t)$ (--), $\hat{U}_-(0,t)$ (□), $\hat{U}_+(L,t)$ (▽), $\Delta\hat{\phi}_e(L,t)$ (•), with 25 mV error threshold (···).

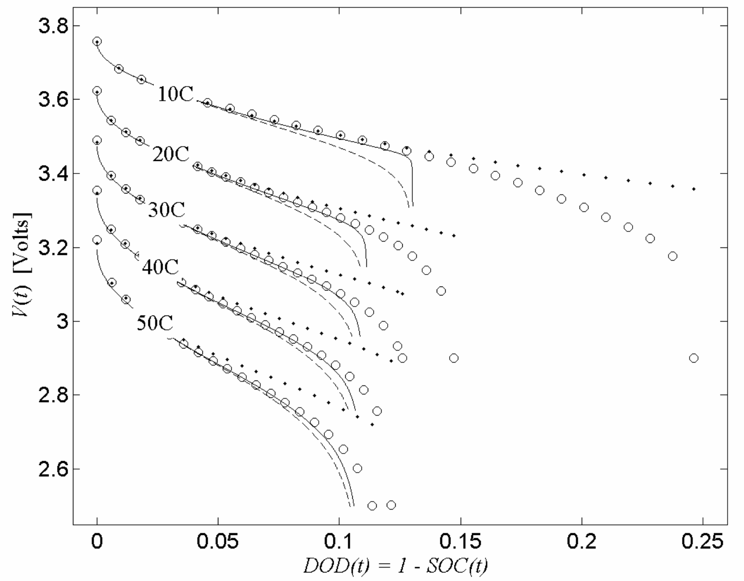

Figure 6.9. Voltage response of various SVMs versus CFD model during constant current discharge from 100% SOC initial condition with sluggish electrolyte diffusion, $D_e = 2.6 \times 10^{-7}$ cm^2/s: CFD model (○), nonlinear OCP/$c_{s,e}$ SVM (•), nonlinear OCP/$c_{s,e}$/$\kappa^{eff}(c_e)$ SVM (-), and nonlinear OCP/$c_{s,e}$/$\kappa^{eff}(c_e)$/$\ln(c_e)$ SVM (--).

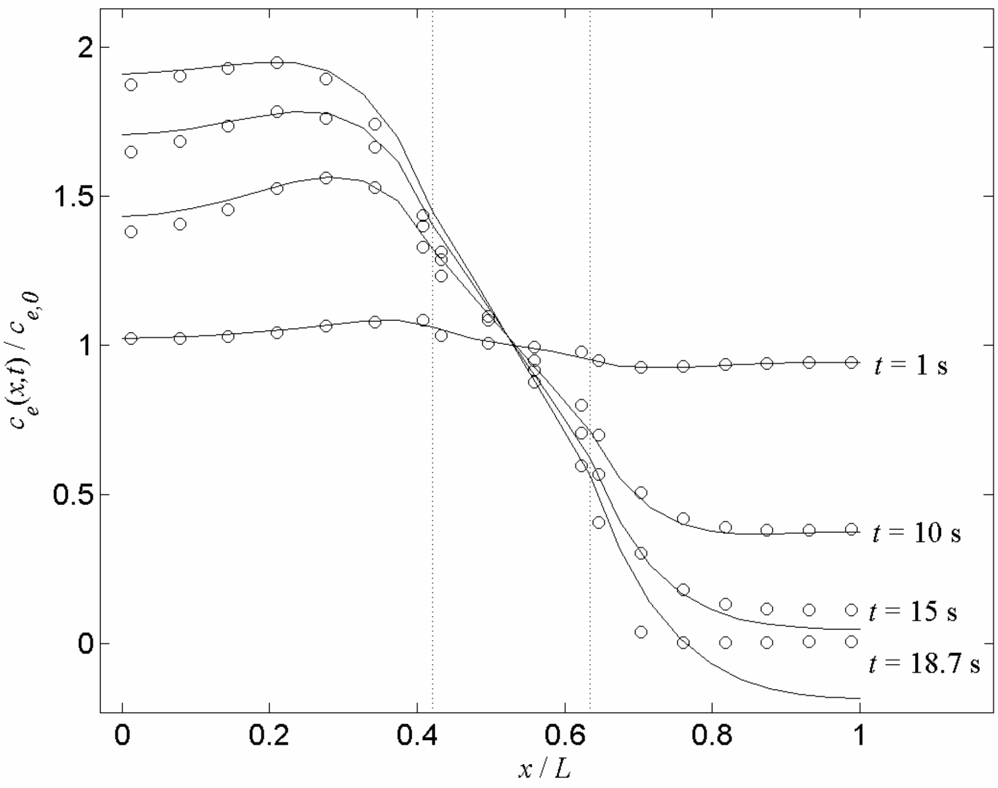

Figure 6.10. Distribution of electrolyte surface concentration at various times during 30C discharge from 100% SOC initial condition with sluggish electrolyte diffusion, D_e = 2.6 x 10^{-7} cm^2/s (voltage response shown in Fig. 10): CFD model (○) and linear SVM (-).

Chapter 7 – ELECTROCHEMICAL ESTIMATION AND CONSTRAINT MANAGEMENT

High power batteries are often rated with multiple current and voltage limits depending on the duration of the pulse event. These variable control limits, however, are difficult to realize in practice. In this chapter, a linear Kalman filter based on the reduced order electrochemical model (Chapter 6) is designed to estimate internal battery potentials, concentration gradients, and state of charge (SOC) from external current and voltage measurements. A reference current governor predicts operating margin with respect to electrode surface depletion/saturation conditions and side reactions responsible for damage and sudden loss of power. The estimates are compared with the nonlinear CFD model of the 6 Ah HEV battery (Chapter 3).

7.1 Linear Kalman Filter

Chapter 6 introduced a linear current/voltage state variable model

$$\begin{aligned} \dot{\mathbf{x}} &= \mathbf{A}\,\mathbf{x} + \mathbf{B}\,u \\ y &= \mathbf{C}\,\mathbf{x} + \mathbf{D}\,u + y_0 \end{aligned} \tag{7.1}$$

with $u = I(t)$ and $y = V(t)$. The standard Kalman filter formulation [23] assumes the plant contains process noise w and measurement noise v in the form

$$\begin{aligned} \dot{\mathbf{x}} &= \mathbf{A}\mathbf{x} + \mathbf{B}u + \mathbf{G}w \\ y &= \mathbf{C}\mathbf{x} + \mathbf{D}u + y_0 + v\,. \end{aligned} \tag{7.2}$$

State estimates $\hat{\mathbf{x}}$ are calculated from sensor measurements $u(t)$ and $y(t)$ as

$$\dot{\hat{\mathbf{x}}} = \mathbf{A}\hat{\mathbf{x}} + \mathbf{B}u + \mathbf{L}(y - y_0 - \mathbf{C}\hat{\mathbf{x}} + \mathbf{D}u)\,. \tag{7.3}$$

The optimal filter gain **L** is precalculated offline as a function of process noise covariance $\mathbf{Q}_w$, measurement noise covariance $\mathbf{Q}_v$, and process noise input matrix **G** to minimize the steady state error covariance

$$\mathbf{P} = \lim_{t\to\infty} E\left([\mathbf{x} - \hat{\mathbf{x}}]\,[\mathbf{x} - \hat{\mathbf{x}}]^T\right). \tag{7.4}$$

7.2 Reference Current Governor

To avoid sudden loss of power, Li concentrations must be maintained within constraints

$$0 < \frac{c_{s,e}(x,t)}{c_{s,\max}} < 1 \quad \text{and} \quad c_e(x,t) > 0\,.$$

To avoid damaging side reactions, the solid/electrolyte phase potential difference, $\phi_{s-e} = \phi_s - \phi_e$, must be maintained within constraints

$$U_{\substack{side\ \ rxn,\\ de-insertion}} < \phi_{s-e}(x,t) < U_{\substack{side\ \ rxn,\\ insertion}}$$

where $U_{side\ rxn}$ is the equilibrium potential of a side reaction occurring when Li ions are either inserted into or de-inserted from active material particles.

Using the state estimate $\hat{\mathbf{x}}(t)$ from Eq. (7.4) we predict a limiting current such that, at future time *t*+*T*, internal battery parameter *y* (i.e. a concentration or potential) will reach limiting value y_{lim} (saturation/depletion, side reaction, etc.). For constant *u*, the linear state equation may be integrated forward in time with an explicit solution. The limiting current available for *T* seconds is thus

$$I_{\min/\max,T} = [\mathbf{C}\,\mathbf{A}^*\ \mathbf{B} + \mathbf{D}]^{-1}\left\{(y_{\lim} - y_0) - \mathbf{C}\,e^{\mathbf{A}T}\ \hat{\mathbf{x}}\right\}. \qquad (7.5)$$

For the present system with $\lambda_1 = 0$,

$$\mathbf{A}^* = diag\left(T \quad \tfrac{1}{\lambda_2}(e^{\lambda_2 T} - 1) \quad \cdots \quad \tfrac{1}{\lambda_n}(e^{\lambda_n T} - 1)\right). \qquad (7.6)$$

Note that for this single-output system the square-bracketed term in Eq. (7.6) is scalar and no matrix inversion is required.

7.3 Results and Discussion

In Chapter 6, a linear current/voltage state variable model (7.1) was constructed by separately fitting transfer functions related to negative electrode solid state diffusion, positive electrode solid state diffusion and electrolyte diffusion dynamics with states $\mathbf{x} = [SOC\ \mathbf{x}_-^{\ T}\ \mathbf{x}_+^{\ T}\ \mathbf{x}_e^{\ T}]^T$. Eigenvalues for the negative and positive electrode states were closely matched, however, and in the present application we find the positive and negative electrode may share the same set of eigenvalues with little loss in accuracy. With states **x** =

$[SOC\ \mathbf{x}_{\pm}{}^{T}\ \mathbf{x}_{e}{}^{T}]^{T}$, the present voltage/current model takes the form

$$\mathbf{A} = diag\left(0\ \boldsymbol{\lambda}_{\pm}\ \boldsymbol{\lambda}_{e}\right),\ \mathbf{B} = \left[-\tfrac{1}{Q}\ 1 \cdots 1\right]^{T},\ \mathbf{C} = \left[\tfrac{\partial(U_{+} - U_{-})}{\partial SOC}\ \mathbf{C}_{\pm}\ \mathbf{C}_{e}\right],\ \mathbf{D} = \left[\mathbf{D}_{\pm} + \mathbf{D}_{e} - \tfrac{R_f}{A}\right] \qquad (7.7)$$

where Q is battery capacity. As a nominal model we use 5 states to describe positive and negative electrode solid state concentration gradient dynamics, 1 state to describe electrolyte concentration gradient dynamics and an additional state for SOC. This $5D_{s\pm}/1D_e$ state variable model, with 0 to 10Hz bandwidth, has eigenvalues

$\lambda_{SOC} = 0$, $\lambda_{\pm} = -[0.00704, 0.0606, 0.613, 6.10, 63.1]$, $\lambda_e = -0.0992$ rad/s.

Sizing filter gain **L** requires choice of $\mathbf{Q}_w$, $\mathbf{Q}_v$, and **G**. To simplify choice, we interpret w as current sensor noise and adjust its influence on individual states with **G**. With this interpretation, $\mathbf{Q}_w$ is current sensor noise covariance and $\mathbf{Q}_v$ is voltage sensor noise covariance, here, $\mathbf{Q}_w = (2\text{A})^2$ and $\mathbf{Q}_v = (0.025\text{V})^2$. In theory, the relative influence of process noise on individual states may be adjusted with individual elements of **G**. In the present application, however, we find that filter eigenvalues (eigenvalues of **A**-**LC**) deviate very little from model eigenvalues (eigenvalues of **A**) irrespective of $\mathbf{Q}_w$, $\mathbf{Q}_v$, and **G** with the exception of λ_{SOC}. The SOC eigenvalue, located at the origin in the open-loop model, takes on negative real values in the closed-loop filter. Attempts to move other filter eigenvalues to slightly faster locations (as little 1.01x $\lambda_{\pm}$) through pole placement causes state estimates to become overly sensitive to sensor noise.

Figure 7.1 compares filter results to data generated by the nonlinear CFD model simulating a Federal Urban Driving Schedule (FUDS cycle) for a hybrid electric mid-sized passenger car (Fig. 3.5) at 50% SOC. The cycle consists of short duration, low to medium rate current pulses for which battery response is largely linear. Filter states are initialized at $\hat{\mathbf{x}}(0) = [0.2\ \ 0 \ldots 0]^T$, i.e. 20% SOC with zero solid and electrolyte phase concentration gradients. The filter gain is sized with $\mathbf{G} = [0.005 \ldots 0.005]$, giving 20-30 second convergence to proper SOC (Fig. 7.1c). Faster converging filters yield noisy estimates when sensor noise is included in the simulation. To simplify discussion, Figs. 7.1d and 7.1e present solid phase surface concentration distributions, $c_{s,e}(x,t)$, as electrode-averaged surface stoichiometries

$$\theta_{s,e}(t) = \frac{1}{\delta c_{s,\max}} \int_0^\delta c_{s,e}(x,t)\, dx . \qquad (7.8)$$

Surface stoichiometries rise and fall much faster than SOC as they are more closely-coupled to recent charge/discharge history. Overshoot in SOC and surface stoichiometry can occur when filter states $\hat{\mathbf{x}}_\pm$, and/or $\hat{\mathbf{x}}_e$ are initialized to non-zero values but convergence is still obtained in 20-30 seconds.

In many situations, and particularly for input currents with negligible DC component such as the FUDS cycle current profile shown in Fig. 7.1a, lower order filters provide good performance. Electrolyte diffusion dynamics, impacting voltage response of the present battery only for sustained medium-to-high rate currents, may be dropped from the filter and electrode transcendental transfer functions may be fit with 3rd and 4th order rational transfer functions rather than 5th order. Figure 7.2 compares SOC and electrode surface stoichiometry errors for filters constructed from $5D_{s\pm}/0D_e$, $4D_{s\pm}/0D_e$, and $3D_{s\pm}/0D_e$ models. The $4D_\pm/0D_e$ model has eigenvalues

$$\lambda_{SOC} = 0,\ \lambda_\pm = -[0.00828, 0.0127, 2.31, 41.5] \text{ rad/s},$$

and the $3D_{s\pm}/0D_e$ model has eigenvalues

$$\lambda_{SOC} = 0,\ \lambda_\pm = -[0.0116, 0.581, 27.3] \text{ rad/s}.$$

Small difference is evident between the three filters' performance on the FUDS cycle.

In Fig. 7.3, the battery is discharged from 100% SOC via 60 A pulses of 10 s duration with 10 s of rest between each pulse. The discharge may be interpreted as a 30A constant current discharge superposed with ±30A perturbations. The DC component of the current profile causes an electrolyte concentration gradient to be established after approximately 20 seconds. Comparison of the $5D_{s\pm}/1D_e$ and the $5D_{s\pm}/0D_e$ filters shows that an additional 1-2% in SOC error and 1% in $\theta_{s,e}$ error is introduced by dropping electrolyte phase dynamics from the filter. Reducing the electrode model from 5 to 3 states introduces an additional 1% error in $\theta_{s,e-}$ but affects $\theta_{s,e+}$ and SOC estimates very little.

The discharge presented in Fig. 7.3 exhibits significant nonlinearities at beginning ($t < 75$ s) and end of discharge ($t > 450$ s) where the linear filter performs poorly. Equilibrium potentials U_+ and U_-, functions of surface stoichiometry, represent the dominant nonlinearity of the battery and the linear filter performs well so long as $\theta_{s,e-}$ and $\theta_{s,e+}$ remain within approximately ±0.15 of their 50% SOC linearization points. Note that surface stoichiometry, and thus equilibrium potential, will be a function of SOC only at rest, in the absence of solid state concentration gradients. At rest, the linear filter is accurate in the interval 27% < SOC < 72%. Under discharge or charge, however, surface dynamics can significantly lead bulk dynamics (i.e. SOC) and for the particular pulse discharge case shown in Fig. 7.3, the filter performs well from 92% SOC (t = 75 s) to 49% SOC (t = 450 s).

We explore two different filter applications of practical value for HEV control: (i) Calculation of an instantaneous "do not exceed" current which, in coordination with motor inverter power electronics, will prevent battery damage, and (ii) Prediction of maximum current available for T seconds which, in coordination with supervisory controllers, will enable efficient and reliable control of the HEV powertrain. State estimates are provided by the $5D_{s\pm}/1D_e$ (7 state) linear filter. Limiting currents are calculated using Eq. (7.5), with T = 0 for the case of the instantaneous current limit and T = 10 s for the case of available current prediction. Due to the closed-loop interaction between model and filter, the plant is simulated using a $5D_{s-}/5D_{s+}/1D_e$ (12 state) nonlinear state variable model rather than the CFD model. This nonlinear state variable model was validated in Chapter 6 to within ±25mV of the CFD model at current rates up to 300 A.

Simulations of the 6 Ah battery show that negative electrode surface depletion limits the discharge performance before the occurrence of either positive electrode saturation or electrolyte depletion. The manufacturer's 2.7 V minimum voltage limit signals the end of discharge when $\theta_{s,e-}$ falls in the range [0.03, 0.3], depending on discharge current rate, SOC, and recent charge/discharge history. As a goal, we wish to limit battery discharge to $\theta_{s,e-} \geq 0.03$ using a maximum reference current.

Figure 6.4 presents simulation results in which a nominal current profile, I_{nom}, consisting of five-second long 300 A current pulses, is limited to $I_{\max}^{\theta_{s,e-}}$, i.e. the battery is discharged at the rate $I(t) = \min(I_{\mathrm{nom}}(t),\ I_{\max}^{\theta_{s,e-}}(t))$. Simulations are presented for two different negative electrode surface stoichiometry limits, 0.03 and 0.25. The linear filter provides an imprecise, albeit conservative reference current at the 0.03 limit due to plant nonlinearity at this low stoichiometry. If we limit current within the stoichiometry range $\theta_{50\%-} \pm 0.15$ where the linear filter provides good performance, the reference current is more precise. Figure 6.4c shows that discharge may be tightly controlled to a $\theta_{s,e-} \geq 0.25$ limit.

Charge performance of the present cell is limited by the manufacturer's 3.9 V maximum voltage limit, though other Li-ion cells are sometimes charged as high as 4.2 V. The 3.9 V limit is far from electrode saturation/depletion, and is more likely intended to prolong battery life by slowing or avoiding side reactions that occur during charging at high voltages. As discussed in Chapter 3, one such side reaction is lithium plating on the electrode surface, predicted to occur in the negative electrode when $\phi_{s-e} = \phi_s - \phi_e < U_{Li,s}$, with equilibrium potential $U_{Li,s} = 0$ [2,59]. Rather than insert into the electrode active material particles, Li^+ ions from the electrolyte solution will form a solid Li film on the particle surface. If the manufacturer's 3.9 V maximum limit is to be respected, the CFD model predicts a worst-case phase potential difference $\phi_{s-e} = 82$ mV occurring at the negative electrode/separator interface ($x = \delta_-$) during slow charging near 100% SOC.

In Figure 7.5, the nominal five-second 180 A pulse charging profile is limited by the afore-mentioned phase potential difference, that is the battery is charged at the rate $I(t) = \max(I_{\text{nom}}(t),\ I_{\min}^{\phi_{s-e}^{x=\delta_-}}(t))$. In the two cases presented, $\phi_{s-e}^{x=\delta_-} \geq 82$ mV and $\phi_{s-e}^{x=\delta_-} \geq 70$ mV, the system charges 10-15 mV beyond the specified limit due to plant nonlinearities, but still stays well above the theoretical limit, $U_{Li,s} = 0$. Despite the error associated with the linear filter, the opportunity clearly exists to pulse charge the battery at voltages beyond 3.9 V and still maintain conservatism with respect to the lithium plating side reaction.

Lastly, we consider prediction of maximum discharge current available for some time into the future, intended as a feed-forward input to powertrain supervisory control. The method is also applicable in the charge direction. Using $\theta_{s,e-} = 0.03$ as end of discharge limit and $T = 10$ s in Eq. (7.5), Fig. 7.6 shows $I_{\max,10s}$ discharge events simulated once every 20 s during a more severe FUDS cycle with four times the input current of the nominal FUDS cycle (Fig. 7.1a). The filter, initialized with a +10% SOC error, converges in 20 to 30 seconds. The first $I_{\max,10s}$ discharge event overshoots the $\theta_{s,e-} = 0.03$ end of discharge condition due to the initial error, however, after 20 s, the maximum discharge current is accurately predicted. Following several strong discharge pulses from 160 to 200 seconds, some SOC estimation error is evident, caused by low $\theta_{s,e-}$ and accompanying nonlinear voltage response. Filter estimates recover as concentration gradients relax. Maximum current, underpredicted during this excursion, also recovers to good accuracy for the remainder of the cycle.

Table 7.1 quantifies the ability of lower order filters to forecast $I_{\max,10s}$ with end of discharge condition $\theta_{s,e-} = 0.03$ on the 4xFUDS cycle following the initial convergence transient. Only slight performance is lost by dropping the electrolyte diffusion state from the filter and/or by reducing the number of electrode states from 5 to 4 but further reduction to 3 electrode states greatly increases the variability in $\theta_{s,e-}$ reached at the end of each discharge event simulation. The $3D_{s\pm}/0D_e$ filter sometimes predicts discharge rates that are not sustainable, with surface stoichiometry depleted in less than 10 s. The 4th order $3D_{s\pm}/0D_e$ filter is still a feasible candidate, though only if used with a more conservative end of discharge stoichiometry limit, perhaps $\theta_{s,e-} = 0.06$.

Available current prediction is attractive due to the explicit manner in which the linear problem may be solved online, however an available power prediction would be more meaningful in the vehicle environment. A precise power estimate would require an iterative nonlinear solver (such as the bisection search) performing constant power forward time simulation as discussed in [66]. Alternatively, a conservative discharge power estimate may be explicitly calculated as

$$P_{\max,T} = (I_{\max,T})\,(V_{\min}) \tag{7.9}$$

where $V_{\min}$ represents the lowest voltage occurring during the maximum current event, i.e. at the end. A conservative charge power estimate may be explicitly calculated as

$$P_{\min,T} = (I_{\min,T})\,(U_{+} - U_{-} + D\,I_{\min,T}) \tag{7.10}$$

where U_+ and U_- are equilibrium potentials (functions of electrode surface stoichiometry at the current collectors, not functions of SOC) and D is the static gain component of the voltage/current state variable model. The voltage $(U_{+} - U_{-} + D\,I_{\min,T})$ will be the lowest voltage over the course of an $I_{\min,T}$ event, occurring at the very beginning. Figure 7.7 presents the 4xFUDS simulation with $P_{\max,10s}$ events simulated every 20 s. With the exception of the first event influenced by filter initial conditions, power capability predicted from Eq. (7.9) is, on average, 12% lower than actual available power. Less conservative power prediction may be obtained using a nonlinear reference governor at the expense of added computational overhead.

7.4 Conclusions

This chapter shows how filters with low order (4 to 7 states) may be designed from a fundamental Li-ion battery model to control battery charge/discharge up to physical saturation/depletion and side reaction limits rather than more conservative fixed voltage limits at the battery terminals. The linear filter, based on a 50% SOC linearized model, performs well so long as electrode surface stoichiometries stay within rest values corresponding to 30% to 70% SOC. During discharge or charge however, electrode surface dynamics can significantly lead bulk (SOC) dynamics and a severe discharge/charge event may cause nonlinear voltage response even with SOC near the 50% linearization point. Following such an event, the linear filter recovers as electrode solid state concentration gradients relax.

Unlike previous control-oriented electrochemical models formulated using spatial discretization techniques [44,45], the present reduced order model enjoys computational efficiency comparable to equivalent circuit models. Expressed as a maximum current available for a finite time horizon, the reference governor predicts margin with respect to saturation/depletion and side reaction conditions in a manner practical for integration with HEV powertrain supervisory control. Instantaneous operating limits generally occur in nonlinear regions of battery operation for which a nonlinear filter would be better suited than the linear filter. Despite the error associated with the linear filter, the present method enables pulse charging beyond the manufacturer’s maximum voltage limit while still maintaining conservatism with respect to the lithium plating side reaction.

Model	# States	$\sigma(\theta_{s,e}(T) - 0.03)$	$\min(\theta_{s,e}(T))$
$3D_{s\pm}/0D_e$	4	0.01953	0.000568
$3D_{s\pm}/1D_e$	5	0.0245	< 0
$4D_{s\pm}/0D_e$	5	0.00908	0.0379
$4D_{s\pm}/1D_e$	6	0.01254	0.0377
$5D_{s\pm}/0D_e$	6	0.00818	0.0392
$5D_{s\pm}/1D_e$	7	0.01276	0.0316

Table 7.1. Standard deviation (relative to $\theta_{s,e-} = 0.03$ limit) and minimum value of $\theta_{s,e-}$ at end of $I_{\max,10s}$ discharge events during 4xFUDS simulations similar to that presented in Fig. 7.6. $I_{\max,10s}$ predicted by filters of varying order.

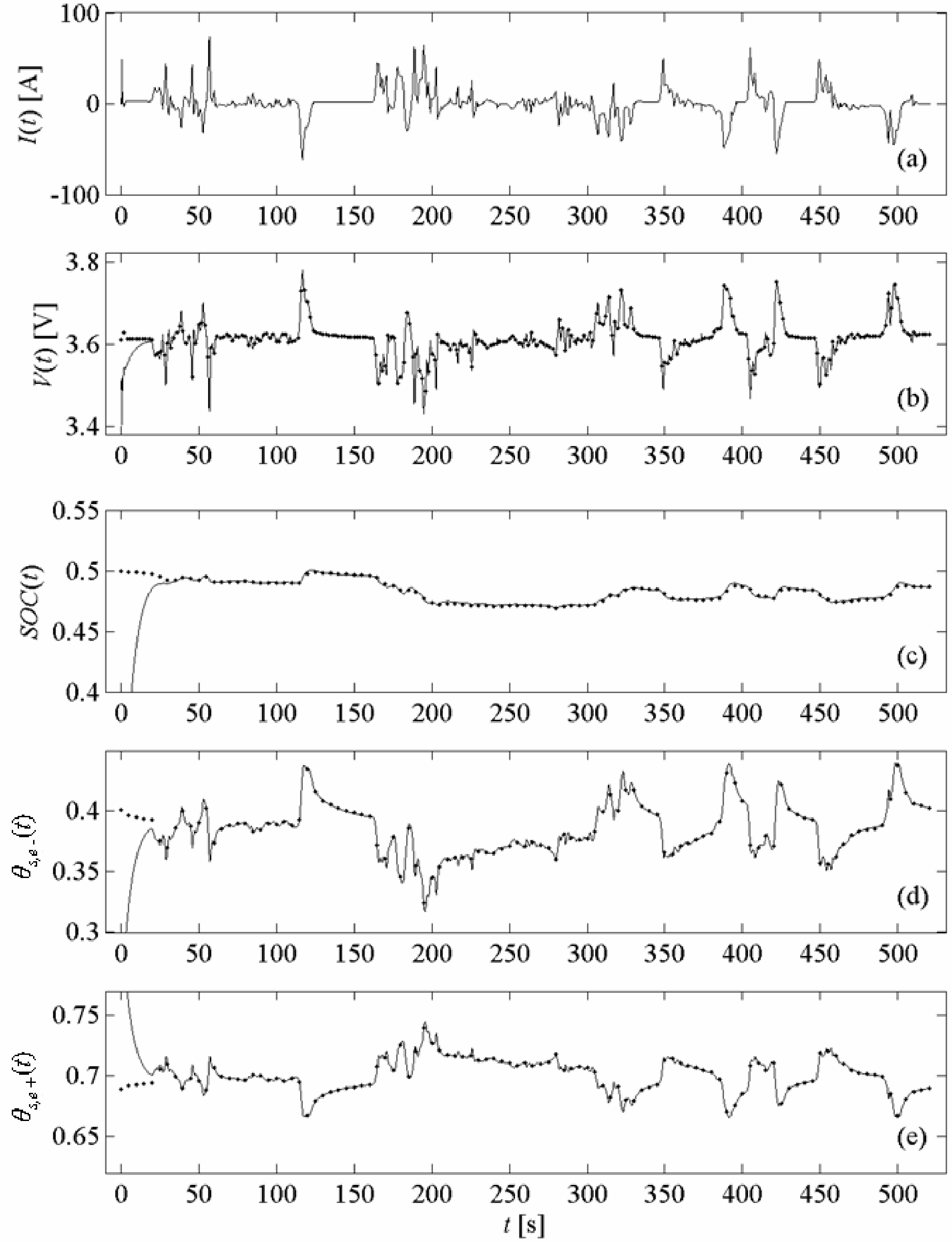

Figure 7.1. FUDS driving cycle simulation: Nonlinear CFD model with 50% SOC initial condition (•) and linear filter with 20% SOC initial condition (-). (a) Current profile, (b) Voltage response, (c) SOC, (d) Negative electrode average surface stoichiometry, (e) Positive electrode average surface stoichiometry.

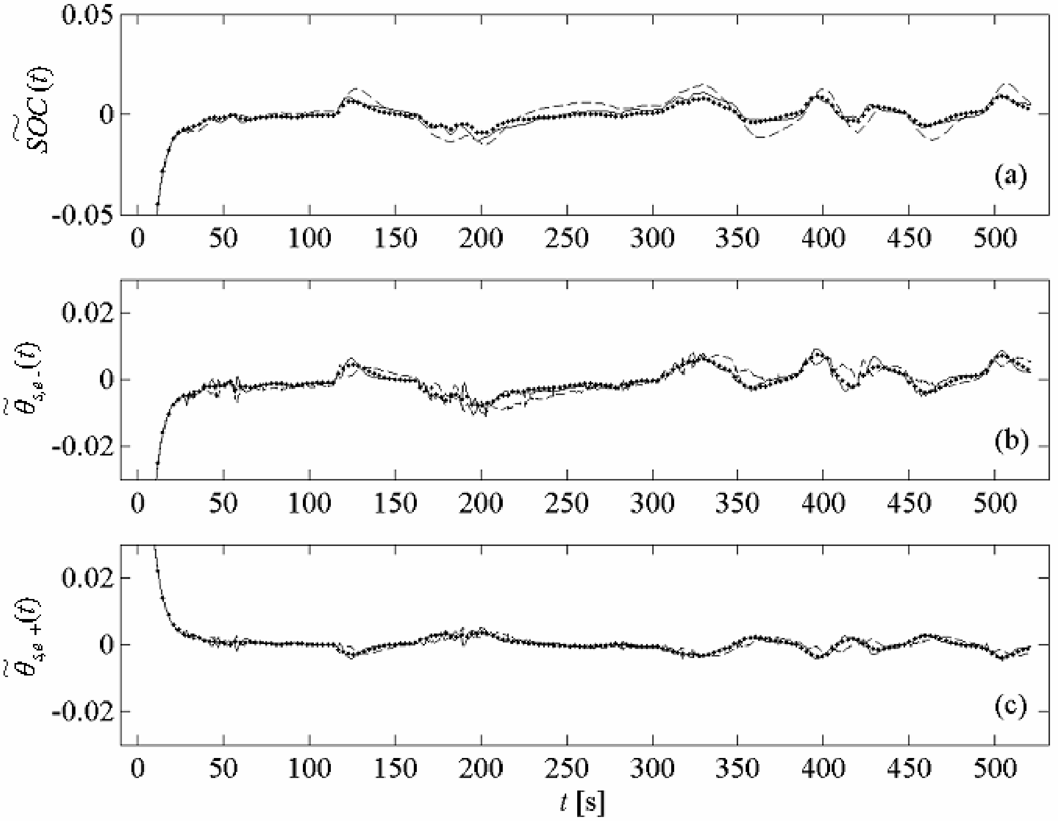

Figure 7.2. Filter error for FUDS driving cycle simulation using filters of various order: $5D_{s\pm}$ /$0D_e$ (6 state) filter (•), $4D_{s\pm}$/$0D_e$ (5 state) filter (-), $3D_{s\pm}$/$0D_e$ (4 state) filter (--). SOC initial conditions: 50% and 20%, respectively, for nonlinear CFD model and linear filters.

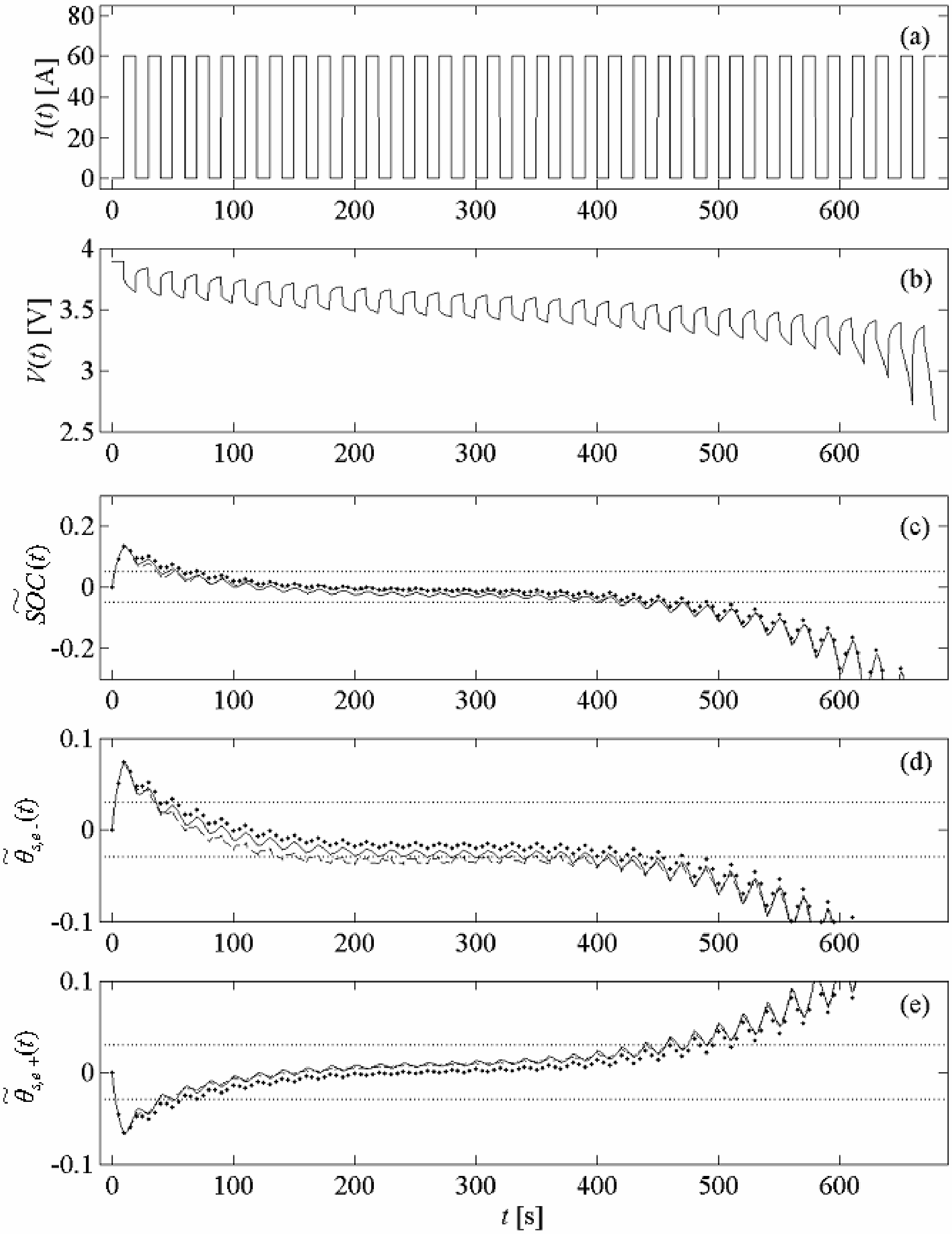

Figure 7.3. Ten-second, 60 A pulse discharge profile initiated from 100% SOC: (a) Current profile; (b) Voltage response of nonlinear CFD model; (c-e) Filter errors: $5D_{s\pm}$ /$1D_e$ (7 state) filter (•), $5D_{s\pm}$ /$0D_e$ (6 state) filter (-), $3D_{s\pm}$ /$0D_e$ (4 state) filter (--). Horizontal dotted lines denote ±5% SOC error threshold in (c) and ±3% surface stoichiometry error thresholds in (d) and (e).

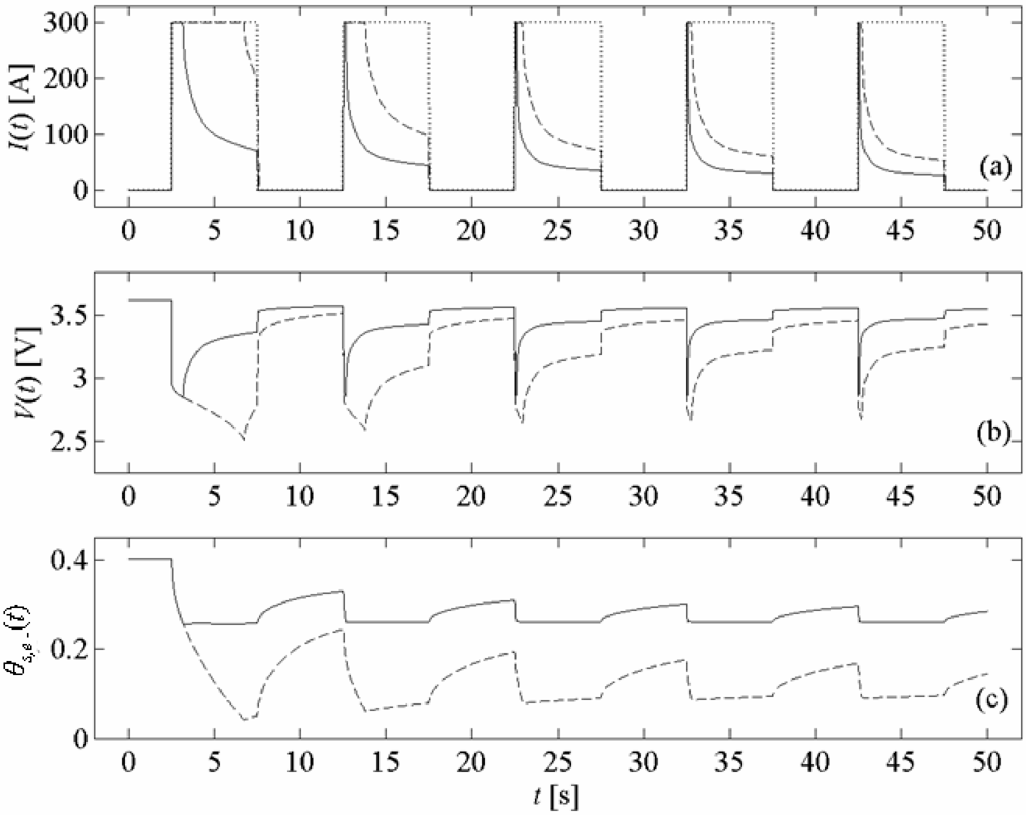

Figure 7.4. Five-second, 300 A nominal pulse discharge profile (…) limited by $\theta_{s,e-} \geq 0.25$ maximum reference current (-) and $\theta_{s,e-} \geq 0.03$ maximum reference current (--). 50% SOC initial condition.

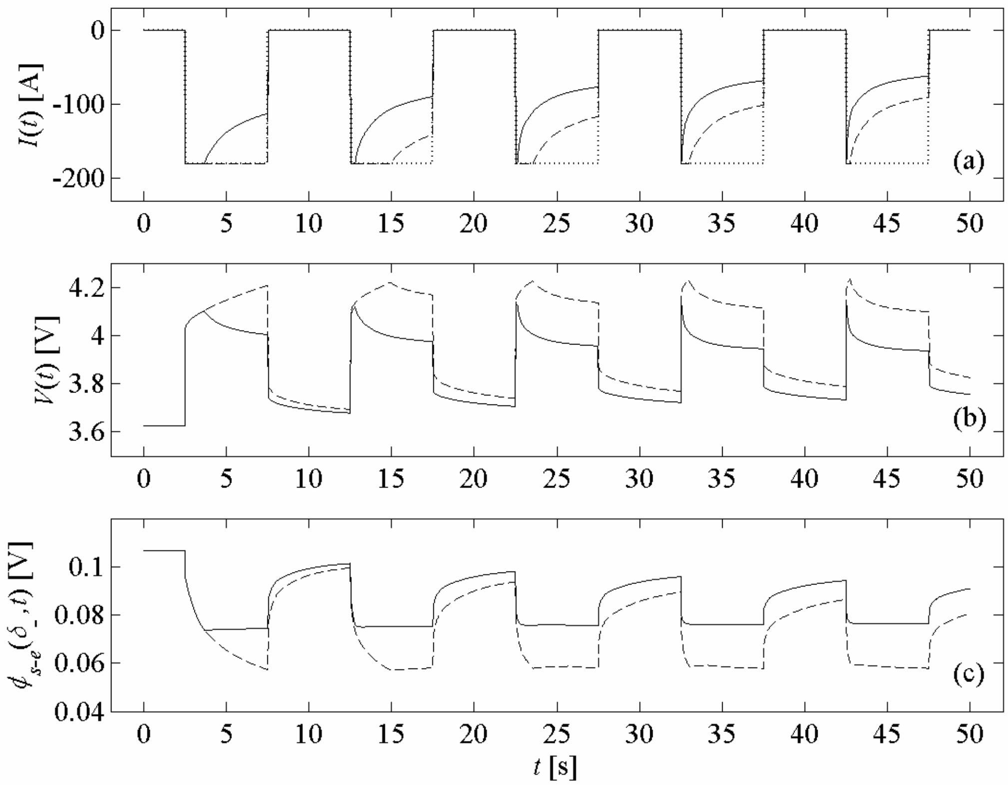

Figure 7.5. Five-second, 180 A nominal pulse charge profile (…) limited by negative electrode $\phi_{s-e} \geq 0.082$ V minimum reference current (-) and $\phi_{s-e} \geq 0.07$ V minimum reference current (--). 50% SOC initial condition.

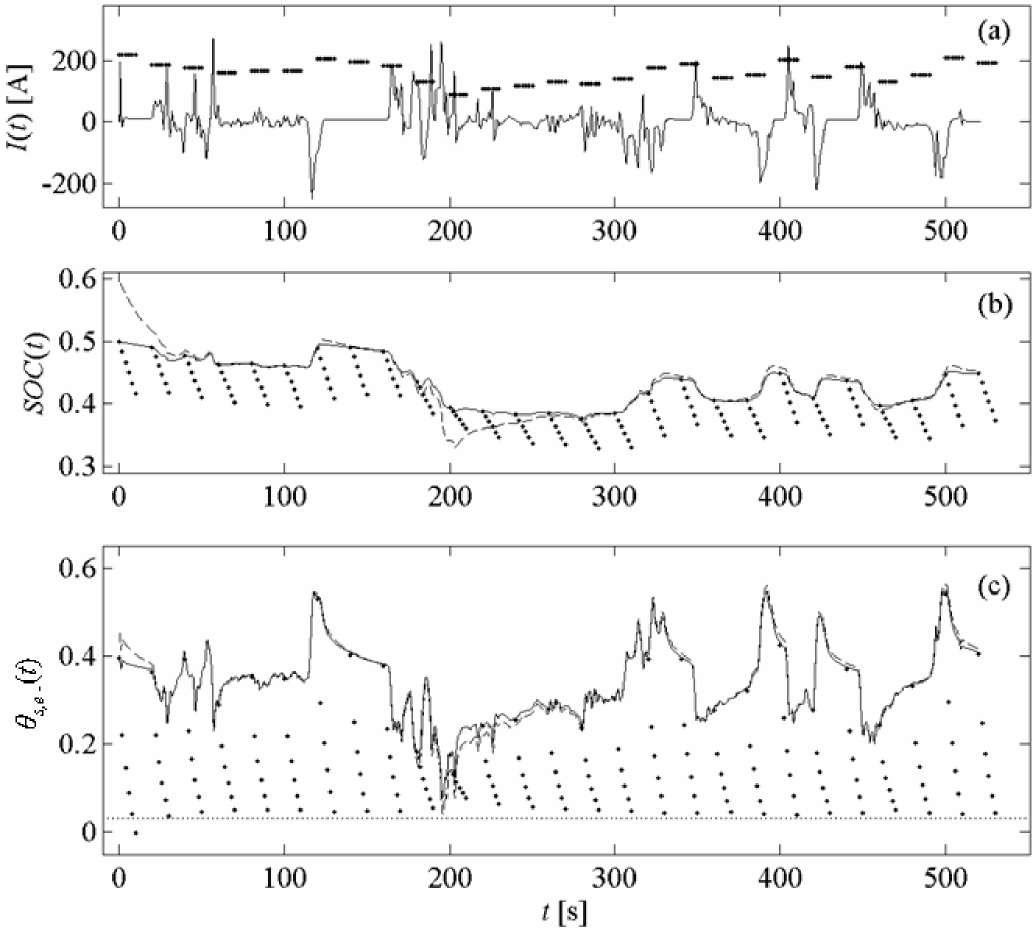

Figure 7.6. 4xFUDS driving cycle with ten-second maximum current discharge events simulated once per 20 seconds: Model with 50% SOC initial condition (-), Filter with 60% SOC initial condition (--), $I_{\max,10s}$ discharge events (•). $I_{\max,10s}$ calculated with $\theta_{s,e-}$ = 0.03 end of discharge condition, shown in (c) with horizontal dotted line.

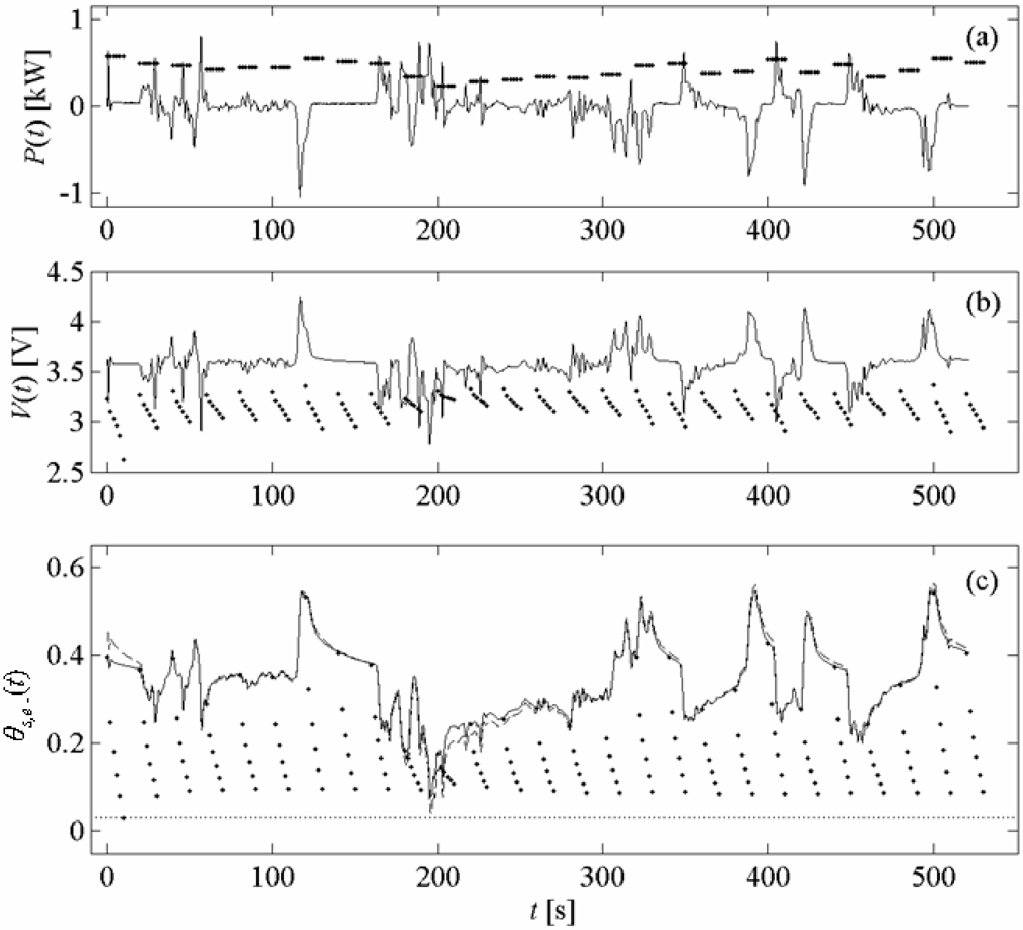

Figure 7.7. 4xFUDS driving cycle with ten-second maximum power discharge events simulated once per 20 seconds: Model with 50% SOC initial condition (-), Filter with 60% SOC initial condition (--), $P_{\max,10s}$ discharge events (•). $P_{\max,10s}$ calculated with 2.65V and $\theta_{s,e-} = 0.03$ end of discharge conditions, the latter shown in (c) with horizontal dotted line.

Chapter 8 – CONCLUSIONS AND FUTURE WORK

8.1 Conclusions

This dissertation introduces a general, electrochemical model-based approach for the efficient and reliable integration of Li-ion batteries into transient, pulse power-type systems. For the 6 Ah hybrid electric vehicle (HEV) battery throughout the present work, we:

1. Experimentally validate a fundamental electrochemical model using constant current data and, more importantly, transient pulse current data representative of the dynamic HEV environment;
2. Reduce the order of the electrochemical model to obtain a nonlinear state variable model with 0 to 10 Hz resolution and fast, explicit execution required for real-time application;
3. Design a linear Kalman filter to estimate potentials and concentration gradients inside the battery from external current and voltage sensor measurements;
4. Employ a reference current governor to control the battery based on internal physical constraints less conservative than the conventional minimum/maximum voltage limits.

The model order reduction technique (Chapter 5) and reduced order battery model (Chapter 6) enable low order filters (Chapter 7) with computational efficiency comparable to equivalent circuit estimation techniques presently used in industry [1,4]. Unlike the empirical methods, the present method controls battery operation to physical saturation/depletion and side reaction limits. Using pulse charge/discharge metrics suggested by DOE test procedures [48], Chapter 4 shows that, at moderate states of charge (SOCs), the 6 Ah battery's charge rate can be increased 50% beyond the 3.9 V-limited rate and still maintain the same level of conservatism with respect to damaging side reactions as provided by the 3.9 V limit at 100% SOC. Shown in Fig. 4.5, useable power and energy density of the battery are increased by 22% and 300%, respectively. This dissertation provides a practical method to realize this increased performance in the uncertain dynamic vehicle environment, effectively increasing the power and energy density of a battery.

A computational fluid dynamics (CFD)-type model validates the low order battery models and estimation algorithms. This is useful, as it is not physically possible to measure concentration/potential distributions inside a battery and thus directly validate the estimates. Figure 8.1 summarizes the procedure followed in Chapter 6 to identify the nonlinear state variable battery model. Though useful, the CFD model (or a similar high order time-domain electrochemical model) is not prerequisite for estimator design as, in the future, it should be possible to directly identify the frequency domain battery model from alternating current impedance data. In this manner, the frequency domain order reduction method employed here is preferable to the Karhuenen-Loève Galerkin method [38] as that procedure would require CFD model simulation results to generate a low order model.

In present industry practice, the system integration process for HEV battery packs is largely empirical. Each new battery pack is experimentally characterized, operating maps are defined, and vehicle supervisory-level control strategies are validated. The approach can be inflexible and time consuming, particularly when seeking to demonstrate long-term reliability throughout battery cycle life. Though the present estimation and management approach has yet to be experimentally verified, it offers potential to significantly streamline the systems integration process. Once the state variable model is parameterized for a candidate battery and its baseline performance is established within a candidate vehicle design, the algorithms may be quickly adapted to a family of battery and vehicle designs with a minimum of additional experimental validation.

8.2 Future Work

8.2.1 Battery Estimation and Control Algorithms

Several practical considerations must be addressed for the present battery management algorithms to be viable in commercial HEVs:

- Temperature dependency must be taken into account. This can either be in an open-loop manner (i.e. by switching between local linear models as a function of temperature measured on the battery casing) or a closed-loop manner (i.e. by using current, voltage, and temperature measurements to predict heat generation rate and provide an estimate of internal battery temperature). Given the concerns associated with Li-ion thermal runaway, an internal battery temperature estimate would be useful.

- The filter and reference governor algorithms must be experimentally validated and shown to be robust throughout the battery life. Modeling studies taking parameter uncertainty into account, a robust filter formulation [67], and/or model adaptation to life-dependent parameters might be useful approaches.

The algorithms might also be extended to cover more difficult estimation problems:

- A nonlinear estimator, such as the extended Kalman filter [68] would allow estimation throughout the 6Ah battery's entire operating range. (The linear filter in Chapter 7 gave good performance only in the 30-70% SOC range.) Nonlinear estimation is likely requisite for battery chemistries having flat equilibrium potential/SOC relationship.
- Equilibrium potential hysteresis must be considered for the nickel metal-hydride battery chemistry [69,70]. A hybrid estimation scheme combining a sliding mode [71] observer with an extended Kalman filter might accomplish this task.

8.2.2 Model Order Reduction of Thermal Fluid Systems

Chapter 5 introduces a residue grouping procedure to reduce the order of linear diffusion systems with closely-spaced negative real eigenvalues. The method rapidly generates low order models, useful in applications such as parameter identification and design space searches. It is unclear whether the grouping method could be extended to linear convection systems whose eigenvalues have imaginary part stacking up in a vertical or near-vertical asymptote in the complex plane [25]. It would be useful to rigorously quantify error associated with the low order grouped residue models, perhaps in an H_∞ sense by finding the maximum singular value of the grouped model error. This approach might lead to robust observers and controllers with much lower order than those obtained through spatial discretization (i.e. finite element, difference or volume) methods [25].

Summarized in Fig. 8.1, Chapter 6 approximates dominant nonlinearities in the battery governing equations by interpolating between local linear reduced order models identified at various electrode surface concentrations, i.e. by lumping the dominant spatially-varying nonlinearity. (By capturing surface concentration dynamics on an average basis (Fig. 6.6), the nonlinear OCP/$c_{s,e}$ state variable model provided good approximation of the battery voltage response during severe high-rate discharge (Fig. 6.4).) Other distributed parameter systems with weak nonlinear spatial-dependence might also be approximated in this manner. It would be useful to formally quantify the error associated with such an approach, perhaps by generating two high order spatially-discretized nonlinear models (both with sufficiently fine mesh), one with lumped nonlinearities and one with spatially-varying nonlinearities. The difference between the two models would be measured in frequency space for a range of admissible nonlinear-dependent field variable distributions. Similar to the present work, the final goal would be to reduce the order of a nonlinear state space to within some error bounds appropriate for the particular control application.

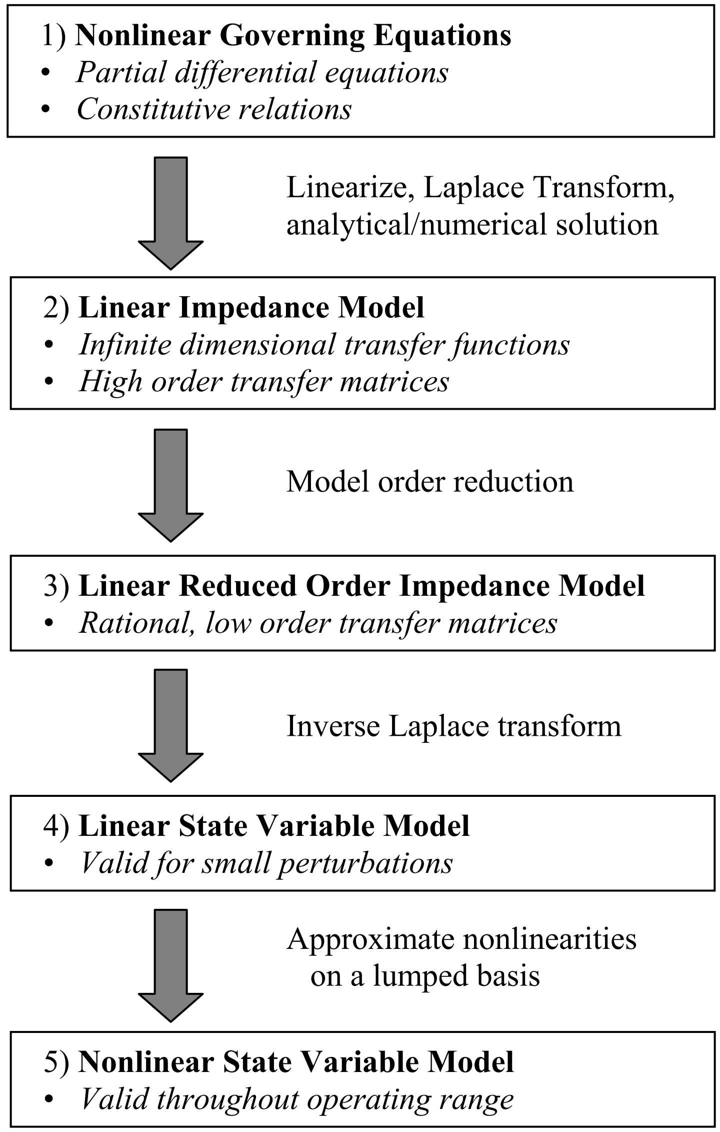

Figure 8.1. Procedure followed in Chapter 6 to obtain a low order nonlinear state variable model of the Li-ion battery.

REFERENCES

---

[1] M. Verbrugge, B. Koch, “Generalized recursive algorithm for adaptive multiparameter regression,” *J. Electrochemical Society*, 153 (2006) A187-201.

[2] M. Doyle, T. Fuller, J. Newman, “Modeling of galvanostatic charge and discharge of the lithium/polymer/insertion cell,” *J. Electrochemical Society*, 140 (1993) 1526-1533.

[3] T. Fuller, M. Doyle, J. Newman, “Simulation and optimization of the dual lithium ion insertion cell,” *J. Electrochemical Society*, 141 (1994) 1-10.

[4] G.L. Plett. “Extended Kalman filtering for battery management systems of LiPB-based HEV battery packs – Part 3. State and parameter estimation.” *J. Power Sources*, 134 (2004) 277-292.

[5] S. Buller, M. Thele, R.W. De Doncker, E. Karden. “Impedance-based simulation models: Supercapacitors and lithium-ion batteries for power electronic application,” *IEEE Ind. Appl. Mag.* (2005) March/April.

[6] S. Piller, M. Perrin, A. Jossen, “Methods for state-of-charge determination and their applications,” *J. Power Sources*, 96 (2001) 113-120.

[7] M. Doyle, J. Newman, A.S. Gozdz, C.N. Schmutz, J.M. Tarascon, “Comparison of modeling predictions with experimental data from plastic lithium ion cells,” *J. Electrochemical Society*, 143 (1996) 1890-1903.

[8] M. Doyle, Y. Fuentes, “Computer simulations of a lithium-ion polymer battery and implications for higher capacity next-generation battery designs,” *J. Electrochemical Society*, 150 (2003) A706-A713.

[9] W.B. Gu and C.Y. Wang, “Thermal-electrochemical coupled modeling of a lithium ion cell,” *ECS Proceedings*, 99-25 (2000) 748-762.

[10] M. Doyle, T. Fuller, J. Newman, “Importance of the lithium ion transference number in lithium/polymer cells,” *Electrochemica. Acta*, 39 (1994) 2073-2081.

[11] T. Fuller, M. Doyle, J. Newman, “Relaxation phenomena in lithium-ion-insertion cells,” *J. Electrochemical Society*, 141 (1994) 982-990.

[12] I. Ong and J. Newman, “Double-Layer Capacitance in a Dual Lithium Ion Insertion Cell,” *J. Electrochemical Society*, 146 (1999) 4360-4365.

[13] M. Doyle, J. Meyers, J. Newman, “Computer simulations of the impedance response of lithium rechargeable batteries,” *J. Electrochemical Society*, 147 (2000) 99-110.

[14] J. Meyers, M. Doyle, R. Darling, J. Newman, “Impedance response of a porous electrode composed of intercalation particles,” *J. Electrochemical Society*, 147 (2000) 2930-2940.

[15] D. Doughty, P. Butler, R. Jungst, E. Roth, “Lithium Battery Thermal Models,” *J. Power Sources*, 110 (2002) 357-363.

[16] S. Al Hallaj, H. Maleki, J. Hong, J. Selman, “Thermal modeling and design considerations of lithium-ion batteries,” *J. Power Sources*, 83 (1999) 1-8.

[17] D. Baker, M. Verbrugge, “Temperature and current distribution in thin-film batteries,” *J. Electrochemical Society*, 146 (1999) 2413-2424.

[18] Y. Chen, J. Evans, “Heat transfer phenomena in lithium/polymer-electrolyte batteries for electric vehicle application,” *J. Electrochemical Society*, 140 (1993) 1833-1838.

[19] G. Botte, B. Johnson, R. White, “Influence of some design variables on the thermal behavior of a lithium-ion cell,” *J. Electrochemical Society*, 146 (1999) 914-923.

[20] P. Nelson, I. Bloom, K. Amine, G. Hendriksen, “Design modeling of lithium-ion battery performance,” *J. Power Sources*, 110 (2002) 437-444.

[21] P. Nelson, D. Dees, K. Amine, G. Henriksen, “Modeling thermal management of lithium-ion PNGV batteries,” *J. Power Sources*, 110 (2002) 349-356.

[22] V. Srinivasan, C.-Y. Wang, “Analysis of electrochemical and thermal behavior of Li-ion cells,” *J. Electrochemical Soc.*, 150 (2003) A98-A106.

[23] C. T. Chen, *Linear System Theory and Design*, Oxford University Press, New York (1999).

[24] G. Franklin, J.D. Powell, M. Workman, *Digital Control of Dynamic Systems*, 3rd ed., Addison Wesley Longman, Menlo Park, CA (1998).

[25] P. D. Christophides, *Nonlinear and Robust Control of PDE Systems – Methods and Applications to Transport-Reaction Processes*, Birkhauser, Boston (2001).

[26] E. Karden, S. Buller, R.W. De Doncker, "A frequency-domain approach to dynamical modeling of electrochemical power sources," *Electrochimica Acta*, 47 (2002) 2347-2356.

[27] K. Smith, C.-Y. Wang, "Solid-state diffusion limitations on pulse operation of a lithium ion cell for hybrid electric vehicles," *J. Power Sources*, 161 (2006) 628-639.

[28] M. Chen, G.A. Rincón-Mora. "Accurate Electrical Battery Model Capable of Predicting Runtime and I-V Performance," *IEEE Trans. on Energy Conversion*, 21 (2006), 504-511.

[29] B. Schweighofer, K.M. Raab, G. Brasseur. "Modeling of High Power Automotive Batteries by Use of an Automated Test System," *IEEE Trans. on Instru. and Meas.*, 52 (2003) 1087-1091.

[30] P. D. Christophides, P. Daoutidis, "Finite Dimensional Control of Parabolic PDE Systems Using Approximate Inertial Manifolds," *J. Math. Anal. Appl.*, 216 (1997) 398-420.

[31] B. Bhikkaji, T. Söderström, "Reduced order models for diffusion systems using singular perturbations," *Energy and Buildings*, 33 (2001) 769-781.

[32] B. Bhikkaji, K. Mahata, T. Söderström, "Reduced order models for a two-dimensional heat diffusion system," *Int. J. Control*, 77 (2004) 1532-1548.

[33] B. Bhikkaji, T. Söderström, "Reduced order models for diffusion systems," *Int. J. Control*, 74 (2001) 1543-1557.

[34] H. M. Park, D. H. Cho, "The Use of the Karhunen-Loève Decomposition for the Modeling of Distributed Parameter Systems," *Chemical Engineering Science*, 51 (1996) 81-98.

[35] M. Loève, *Probability Theory*, Van Nostrand, Princton, NJ (1955).

[36] L. Sirovich, "Turbulence and the Dynamics of Coherent Structures, Parts I-III," *Quart. Appl. Math*, XLV(3) (1987) 561-590.

[37] H. M. Park, W. J. Lee, "Recursive Identification of Thermal Convection," *J. Dynamic Systems, Measurement, and Control*, 125 (2003) 1-10.

[38] H. M. Park, O. Y. Kim, “A Reduction Method for the Boundary Control of the Heat Conduction Equation,” *J. Dynamic Systems, Measurement, and Control*, 122 (2000) 435-444.

[39] V. Pop, H.J. Bergveld, P.H.L. Notten, P.P.L. Regtien, “State-of-the-art of battery state-of-charge determination,” *Measurement Science and Technology*, 16 (2005) R93-R110.

[40] G. M. Ehrlich, “Lithium Ion Batteries,” in *Handbook of Batteries*, 3rd ed., New York: McGraw-Hill (2002), pp. 35.53-35.59.

[41] “Ultra High Power Cells: 7.5Ah UHP-341450.” Lithium Technology Corporation. Plymouth Meeting, PA USA. [Online]. Available: http://www.lithiumtech.com/StandardCells.html

[42] A. Bemporad, “Reference governor for constrained nonlinear systems,” *IEEE Trans. Autom. Control*, 43 (1998) 415-419.

[43] J. Sun, I. V. Kolmanovsky, “Load Governor for Fuel Cell Oxygen Starvation Protection: A Robust Nonlinear Reference Governor Approach,” *IEEE Trans. Control Sys. Technology*, 13 (2005) 911-920.

[44] A. Tenno, R. Tenno, T. Suntio, “Charge-discharge behaviour of VRLA batteries: model calibration and application for state estimation and failure detection,” J. Power Sources, 103 (2001) 42-53.

[45] O. Barbarisi, F. Vasca, L. Glielmo. “State of charge Kalman filter estimator for automotive batteries,” *Control Eng. Practice*, 14 (2006) 267-275.

[46] C.-Y. Wang, V. Srinivasan, “Computational Battery Dynamics (CBD) – Electrochemical/thermal coupled modeling and multi-scale modeling,” *J. Power Sources*, 110 (2002) 364-376.

[47] FreedomCAR Battery Test Manual For Power-Assist Hybrid Electric Vehicles, October 2003, DOE/ID-11069.

[48] PNGV Battery Test Manual, Revision 3, February 2001, DOE/ID-10597.

[49] L.O. Valøen, J.N. Reimers, “Transport properties of LiPF6-based Li-Ion battery electrolytes,” *J. Electrochemical Society*, 152 (2005) A882-A891.

---

[50] D. Dees, E. Gunen, D. Abraham, A. Jansen, J. Prakash, “Alternating current impedance electrochemical modeling of lithium-ion positive electrodes,” *J. Electrochemical Society*, 152 (2005) A1409-A1417.

[51] H.S. Carslaw, J.C. Jaeger, *Conduction of Heat in Solids*, p. 112, Oxford University Press, London (1973).

[52] K. Smith, C.Y. Wang, “Pulse Discharge Power Availability of a Lithium-Ion Hybrid Electric Vehicle Battery Pack,” *Proceedings of the SAE Future Transportation Technology Conference*, Chicago, IL, Sept. 7-9 (2005).

[53] C.Y. Wang, W.B. Gu, B.Y. Liaw, “Micro-macroscopic coupled modeling of batteries and fuel cells. I. Model development,” *J. Electrochemical Society*, 145 (1998) 3407.

[54] T. Jacobsen, K. West, “Diffusion impedance in planar, cylindrical and spherical symmetry,” *Electrochemica Acta*, 40 (1995) 255-262.

[55] G. Sikha, R.E. White, B.N. Popov, “A mathematical model for a lithium-ion battery/electrochemical capacitor hybrid system,” *J. Electrochemical Society*, 152 (2005) A1682-A1693.

[56] V. Subramanian, J. Ritter, R. White, “Approximate solutions for galvanostatic discharge of spherical particles: I. Constant diffusion coefficient,” *J. Electrochemical Society*, 148 (2001) E444-E449.

[57] M.S. Whittingham, “Lithium batteries and cathode materials,” *Chem. Review*, 104 (2004) 4271-4301.

[58] P. Arora, M. Doyle, R. White, “Mathematical modeling of the lithium deposition overcharge reaction in lithium-ion batteries using carbon-based negative electrodes,” *J. Electrochemical Society*, 146 (1999) 3543-3553.

[59] M. Verbrugge, B. Koch, *J. Electroanalytic Chemistry*, 436 (1997) 1-7.

[60] E. Avallone, T. Baumeister, *Marks’ Standard Handbook for Mechanical Engineers*, 10th ed., McGraw-Hill, New York (1996) pp. 4.84-4.85.

[61] S.I. Hayek, *Advanced Mathematical Methods in Science and Engineering*, Marcel Dekker, Inc., New York (2001).

[62] S.C. Chapra, R.P. Canale, *Numerical Methods for Engineers*, 2nd ed., McGraw-Hill, New York (1998).

[63] D.W. Marquardt, "An algorithm for least-squares estimation of nonlinear parameters," *J. Soc. Indust. Appl. Math*, 11 (1963) 431-441.

[64] A.J. Baker, D.W. Pepper, *Finite Elements 123*, McGraw-Hill, New York (1988).

[65] A. Tenno, R. Tenno, T. Suntio, "A method for battery impedance analysis," *J. Electrochemical Society*, 151 (2004) A806-824.

[66] G.L Plett, "High-performance battery-pack power estimation using a dynamic cell model," *IEEE Transactions on Vehicular Technology*, 53 (2004) 1586-1593.

[67] I.R. Petersen, A.V. Savkin, *Robust Kalman Filtering for Signals and Systems with Large Uncertainties*, Birkhauser, Boston (1999).

[68] B.D.O. Anderson, J.B Moore, *Optimal Filtering*, Prentice Hall, Englewood Cliffs, NJ (1979).

[69] K.P. Ta, J. Newman, "Proton intercalation hysteresis in charging and discharging nickel hydroxide electrodes," *J. Electrochemical Society*, 146 (1999) 2769-2779.

[70] V. Srinivasan, J.W. Weidner, J. Newman, "Hysteresis during cycling of hydroxide active material," *Power Source Modeling - Proceedings of the International Symposium, Electrochemical Society* v PV 2002-30, (2005) 74-86.

[71] H.K. Khalil, *Nonlinear Systems*, 3rd ed., Prentice Hall, Upper Saddle River, NJ (2002).

APPENDIX A

Solid State Diffusion Finite Element Model

Described in Chapter 2, transient solid state Li diffusion is incorporated into the previously developed CFD model of Gu and Wang [9]. The macroscopic model requires only the concentration at the surface, $c_{s,e}(t)$, as a function of the time history of local reaction current density, $j^{Li}(t)$. Transform Eqs. (2.1-3) from spherical to planar coordinates using the substitution $v(r) = r\, c_s(r)$ [54] and discretize the new PDE in the r-direction with n linear elements. (The present model uses five elements with node points placed at {0.7,0.91,0.97,0.99,1.0} x R_s.) Transformed back to spherical coordinates, the discretized system is represented as ODEs in state space form,

$$\begin{bmatrix} \dot{c}_{s,1} \\ \dot{c}_{s,2} \\ \vdots \\ \dot{c}_{s,n} \end{bmatrix} = \mathbf{A} \begin{bmatrix} c_{s,1} \\ c_{s,2} \\ \vdots \\ c_{s,n} \end{bmatrix} + \mathbf{B}\, j^{Li}, \qquad c_{s,e} \approx \mathbf{C} \begin{bmatrix} c_{s,1} \\ c_{s,2} \\ \vdots \\ c_{s,n} \end{bmatrix} + \mathbf{D}\, j^{Li}, \tag{A.1}$$

where the n states of the system are the radially-distributed values of concentration $c_{s,1}$, …$c_{s,n}$, at finite element node points 1,…n. For the linear PDE with constant diffusion coefficient, D_s, the matrix **A** is constant and tri-diagonal.

The linear state space system (A.1) can also be expressed as a transfer function,

$$\frac{c_{s,e}(s)}{j^{Li}(s)} \approx G(s) = \frac{b_1 s^n + b_2 s^{n-1} + \ldots + b_{n-1} s + b_n}{a_1 s^n + a_2 s^{n-1} + \ldots + a_{n-1} s + a_n} \tag{A.2}$$

with constant coefficients a_i and b_i [24]. While either (A.1) or (A.2) could be numerically implemented using an iterative solution method, for the linear problem we express the system as a finite difference equation with explicit solution. To discretize (A.2) with respect to time, perform a z-transform using Tustin's method

$$G_T(z) = G(s)\Big|_{s=\frac{2}{T_s}\frac{z-1}{z+1}}, \tag{A.3}$$

resulting in an n^{th} order discrete transfer function

$$\frac{c_{s,e}(z)}{j^{Li}(z)} \approx G_T(z) = \frac{h_1 z^n + h_2 z^{n-1} + \ldots + h_{n-1} z + h_n}{g_1 z^n + g_2 z^{n-1} + \ldots + g_{n-1} z + g_n}\,. \tag{A.4}$$

with constant coefficients h_i and g_i. Computation is thus reduced to an explicit algebraic formula with minimal memory requirements. Solution for $c_{s,e}$ requires that local values of $c_{s,e}$ and j^{Li} be held from only the previous n-1 time steps.

APPENDIX B

Transfer Functions of Short and Long Time Solid State Diffusion Analytical Solutions

Doyle et. al. [2] employ an analytical solution to Eqs. (2.1-3) and embed it inside a Duhamel superposition integral to accommodate the time dependent boundary condition. They provide two integral expressions for the response of reaction current, $j^{Li}(\tau)$, to a step in surface concentration, $\Delta c_{s,e}$, at $\tau = 0$, each in the form

$$a(\tau) = \frac{1}{a_s F}\frac{R_s}{D_s}\frac{1}{\Delta c_{s,e}}\int_0^{\tau} j^{Li}(\zeta)\, d\zeta \,. \tag{B.1}$$

The short time expression (Eq. (B.6) of [2]) is

$$a(\tau) = -\tau + 2\sqrt{\frac{\tau}{\pi}}\left[1 + 2\sum_{n=1}^{\infty}\exp\left(\frac{-n^2}{\tau}\right) - n\sqrt{\frac{\pi}{\tau}}\operatorname{erfc}\left(\frac{n}{\sqrt{\tau}}\right)\right] \tag{B.2}$$

while the long time expression (Eq. (B.5) of [2]) is

$$a(\tau) = \frac{2}{\pi^2}\sum_{n=1}^{\infty}\frac{1}{n^2}\left[1 - \exp\left(-n^2\pi^2\tau\right)\right]. \tag{B.3}$$

Little detail is given in the derivation of these expressions. Differentiating Eqs. (B.1) to (B.3) with respect to τ and solving for $j^{Li}(\tau)$, we recover short time solution

$$j^{Li}(\tau) = a_s F\frac{D_s}{R_s}\left[1 - \frac{1}{\sqrt{\pi\tau}} + \frac{2}{\sqrt{\pi\tau}}\sum_{n=1}^{\infty}\exp\left(\frac{-n^2}{\tau}\right)\right]\Delta c_{s,e} \tag{B.4}$$

and long time solution

$$j^{Li}(\tau) = a_s F\frac{D_s}{R_s}\left[-2\sum_{n=1}^{\infty}\exp\left(-n^2\pi^2\tau\right)\right]\Delta c_{s,e}\,, \tag{B.5}$$

no longer in integral form. Taking the Laplace transform of Eqs. (B.4) and (B.5) and recognizing that the transform of the step input is $C_{s,e}(s) = \Delta c_{s,e} / s$, we find the short time transfer function

$$\frac{J^{Li}(s)}{C_{s,e}(s)} = a_s F\frac{D_s}{R_s}\left[1 - R_s\sqrt{\frac{s}{D_s}} + 2R_s\sqrt{\frac{s}{D_s}}\sum_{n=1}^{\infty}\exp\left(-2nR_s\sqrt{\frac{s}{D_s}}\right)\right] \tag{B.6}$$

and the long time transfer function

$$\frac{J^{Li}(s)}{C_{s,e}(s)} = a_s F \frac{D_s}{R_s}\left[-2\sum_{n=1}^{\infty}\frac{s}{s+n^2\pi^2}\right]. \qquad \text{(B.7)}$$

Taking the reciprocal of Eqs. (B.6) and (B.7) and substituting dimensionless variables $\bar{J}^{Li}$, $\overline{C}_{s,e}$, and ψ yields expressions used in Chapter 3.

APPENDIX C

Transfer Function of Parabolic Profile Solid State Diffusion Approximate Model

Wang et. al. [46] assume concentration distribution within a spherical active material particle to be described by a parabolic profile. Integrating the two parameter polynomial with respect to Eq. (2.1), they reduce the problem of determining surface concentration, $c_{s,e}(t)$, as a function of reaction current, $j^{Li}(t)$, down to the solution of one ODE

$$\frac{\partial c_{s,avg}}{\partial t} = \frac{3}{a_s F R_s} j^{Li} \tag{C.1}$$

and one interfacial balance

$$c_{s,e} - c_{s,avg} = \frac{R_s}{5 a_s F D_s} j^{Li} . \tag{C.2}$$

Taking the Laplace Transform of Eqs. (C.1) and (C.2) yields

$$s\, C_{s,avg}(s) = \frac{3}{a_s F R_s} J^{Li}(s) \tag{C.3}$$

and

$$C_{s,e}(s) - C_{s,avg}(s) = \frac{R_s}{5 a_s F D_s} J^{Li}(s) \tag{C.4}$$

which, when combined to eliminate $C_{s,avg}$, provides the transfer function

$$\frac{C_{s,e}(s)}{J^{Li}(s)} = \frac{1}{a_s F} \frac{R_s}{D_s} \left[\frac{3 D_s}{s {R_s}^2} + \frac{1}{5} \right] . \tag{C.5}$$

Substituting dimensionless variables $\overline{J}^{Li}$, $\overline{C}_{s,e}$, and ψ into Eq. (C.5) yields the expression used in Chapter 3.

APPENDIX D

Nonlinear Least Squares Algorithm

Chapter 5 introduces optimal reduced order diffusion models with eigenvalue and residue parameters found by minimizing cost functions Eq. (5.18) and (5.39). Taking the latter as an example and dropping the double overbar notation, the unknown parameters of the model in Eq. (5.38) are $\mathbf{p} = (\lambda_k , \mathbf{r}_k^T)^T$. For observation j at frequency ω_j, define the error between the model and the data as

$$\mathbf{f}_j = \left[\mathrm{Re}(\mathbf{Y}_j^* - \mathbf{Y}_j)^T \quad \mathrm{Im}(\mathbf{Y}_j^* - \mathbf{Y}_j)^T \right]^T \tag{D.1}$$

with Jacobian

$$\mathbf{J}_j = \left[\frac{\partial \mathbf{f}_j}{\partial \lambda_k}, \ \frac{\partial \mathbf{f}_j}{\partial \mathbf{r}_k} \right] = \begin{bmatrix} \dfrac{-2\lambda_k \omega_j^2 \mathbf{r}_k}{(\lambda_k^2 + \omega_j^2)^2}, & \dfrac{\omega_j^2 \mathbf{1}_k}{\lambda_k^2 + \omega_j^2} \\ \dfrac{\omega_j (\lambda_k^2 - \omega_j^2)\mathbf{r}_k}{(\lambda_k^2 + \omega_j^2)^2}, & \dfrac{-\lambda_k \omega_j \mathbf{1}_k}{\lambda_k^2 + \omega_j^2} \end{bmatrix} \tag{D.2}$$

where the $\mathbf{1}_k$ is a column vector of ones with the same dimensions as $\mathbf{r}_k$. Combining all observations across the frequency range of interest yields $\mathbf{f} = [\ \mathbf{f}_1^T \ \mathbf{f}_2^T \ldots \ \mathbf{f}_j^T \ldots]^T$ and $\mathbf{J} = [\ \mathbf{J}_1^T \ \mathbf{J}_2^T \ldots \ \mathbf{J}_j^T \ \ldots]^T$. Given initial parameter guess $\mathbf{p}^{[0]}$, the set of parameters which minimize the cost function in Eq. (5.39) is found by iteratively solving

$$(\mathbf{J}^T \mathbf{J}) \Delta \mathbf{p} = -\mathbf{J}^T \mathbf{f} \tag{D.3}$$

and updating the parameters at each iteration

$$\mathbf{p}^{[i+1]} = \mathbf{p}^{[i]} + \Delta \mathbf{p} \tag{D.4}$$

as discussed in Chapra and Canale [62]. The Levenberg-Marquardt algorithm [63] is used to substantially improve numerical stability and convergence.

APPENDIX E

State Space Realization of Series Transfer Matrix

From Chapter 5, Eq. (5.30), a series representation of the transfer matrix (5.21) is

$$\mathbf{Y}(s) = \left[\mathbf{Z} + \sum_{k=1}^{n} \frac{\mathbf{r}_k \; s}{s - \lambda_k}\right] U(s) \cdot \tag{E.1}$$

Using the principle of superposition, we express the linear system time domain solution as

$$\mathbf{y}(t) = \mathbf{y}_{\mathbf{Z}}(t) + \sum_{k=1}^{n} \; \mathbf{y}_k(t) \cdot \tag{E.2}$$

The inverse Laplace transform of the static part of Eq. (E.1) is $\mathbf{y}_{\mathbf{Z}}(t) = [\mathbf{Z}]u(t)$. To solve an individual term of the dynamic part, we define the state

$$X_k(s) = \frac{1}{s - \lambda_k} U(s) \tag{E.3}$$

which, by performing the inverse Laplace transform provides the state equation

$$\dot{x}_k(t) = \lambda_k x_k(t) + u(t) . \tag{E.4}$$

The output is related to the state by $\mathbf{Y}_k(s) = \mathbf{r}_k \; s \; X_k(s)$ yielding output equation

$$\mathbf{y}_k(t) = \mathbf{r}_k \dot{x}_k(t) = \mathbf{r}_k \lambda_k x_k(t) + \mathbf{r}_k u(t) . \tag{E.5}$$

Combining individual solutions yields the state space model

$$\begin{aligned} \dot{\mathbf{x}}(t) &= \begin{bmatrix} \lambda_1 & & \\ & \ddots & \\ & & \lambda_n \end{bmatrix} \mathbf{x}(t) + \begin{bmatrix} 1 \\ \vdots \\ 1 \end{bmatrix} u(t), \\ \mathbf{y}(t) &= \begin{bmatrix} \mathbf{r}_1 \lambda_1 & \cdots & \mathbf{r}_n \lambda_n \end{bmatrix} \mathbf{x}(t) + \left[\mathbf{Z} + \sum_{k=1}^{n} \mathbf{r}_k \right] u(t) \end{aligned} \tag{E.6}$$

used in Chapter 5.

VITA

Kandler A. Smith

Education:

Pennsylvania State University, **Ph.D. Mechanical Engineering**, 2006.

Pennsylvania State University, **M.S. Mechanical Engineering**, 2004.

University of Florida, **M.S. Engineering Management**, 2000.

Virginia Tech, **B.S. Mechanical Engineering**, 1997. Minors: German & mathematics.

Work Experience:

Research Assistant, **Penn State**, May 2005-Dec. 2006. Li-ion electrode surface degradation modeling and experiment. Developed new graduate-level engineering curricula.

Graduate Teaching Fellow, **Penn State**, Fall 2004 & Spring 2005. Instructor for sophomore-level thermal-fluid sciences engineering course.

Research Assistant, **Penn State**, Fall 2003-Summer 2004. Developed fundamental Ni-MH & Li-ion battery models for DOE/Argonne National Labs.

NSF K-12 Fellow, **Penn State**, Sept. 2001-Aug. 2003. Engaged 8th grade science students in topics related to advanced hybrid electric and fuel cell vehicles.

Flight Test Field Representative, **UTC Pratt & Whitney**, Sept. 2000-May 2001. Monitored jet engine performance during flight testing of prototype STOVL aircraft.

Engine Control Software Engineer, **UTC Pratt & Whitney**, Sept. 1997-Aug. 2000. Designed jet engine sensor/actuator self-test and failure accommodation software.

Intern, **Alois Scheuch GmbH**, Ried, Austria, Summer 1997.

Intern, **Virginia Tech Ctr. for Transportation Research**, Blacksburg, VA, Summer 1996.

Co-op, **Naval Surface Warfare Center**, Dahlgren, VA, Jan. 1994-Aug. 1995.

Professional Affiliations:

Member: American Society of Mechanical Engineers, Society of Automotive Engineers, The Electrochemical Society